The Evaluation of Silicon Microstrip Detectors for the ATLAS Semiconductor Tracker and Supersymmetry Studies at the Large Hadron Collider

By

Lee Martin Drage

of

Trinity College

A dissertation submitted to the University of Cambridge

for the degree of Doctor of Philosophy

September 1999

Abstract

The ATLAS detector will surround one of the interaction points of the Large Hadron Collider at the European Centre for Particle Physics. The ATLAS Semiconductor Tracker (SCT) will provide precision tracking of charged particles using silicon microstrip detectors. The SCT silicon detectors must operate for at least 10 years in a high radiation environment, in a 2 T magnetic field and with non-normally incident particles.

The first half of this thesis investigates the performance of prototype detectors for the SCT using a 180 GeV/c pion beam. Two beam tests are documented. The first is used to compare the performance of two different silicon microstrip detector designs after detector irradiation to a fluence equivalent to 10 years of ATLAS operation. Detector efficiency, noise occupancy, precision and the charge division between detector strips are studied. The charge produced in a detector by incident pions is compared with the predictions of Landau theory. The second beam test compares the performance of an irradiated detector and an unirradiated detector of the selected SCT design in a magnetic field and with non-normally incident pions. The performance of detectors in both beam tests are found to mostly satisfy design specifications.

The accurate measurement of the momentum and position of charged particles will be essential when searching for new physics. Supersymmetry (SUSY) is the most theoretically favoured extension of the Standard Model, the current theory of fundamental particles and interactions. The majority of studies of the ATLAS potential to discover and investigate SUSY particles have assumed that a discrete symmetry, R-parity, is conserved. In this thesis, an R-parity and baryon number violating supergravity model is considered. A new version of the HERWIG Monte Carlo event generator which correctly incorporates R-parity violating vertices was used with ATLFAST, a particle level simulation of the ATLAS detector. An algorithm to measure three sparticle masses is presented. It is shown that the errors on these measurements are dominated by uncertainties in jet energy scale corrections.

Preface

This thesis is the culmination of work carried out at the Cavendish Laboratory, Cambridge between October 1996 and August 1999. I am indebted to many people who have made these three years stimulating and enjoyable.

Firstly, I wish to thank my supervisor, Andy Parker, for expertly guiding me through my PhD and for giving constructive criticism on drafts of this thesis. I am also very grateful to Janet Carter for allowing me to work with the Cambridge HEP Group and for advice on silicon detectors. I also wish to thank David Munday for help with topics ranging from physics to CERN bureaucracy and John Hill and Steve Wotton for dealing with my computing related problems. Thanks also to Jan White for keeping things running smoothly.

During the course of my PhD, I have spent several months taking data at test beams. I am indebted to Gareth Moorhead, Peter Phillips, Steinar Stapnes, Debbie Morgan, Petra Riedler, Dave Robinson, Javier Sanchez, Maria Jose Costa and many more for making the test beams possible and for making them an enjoyable and gastronomic experience. I also wish to thank Bryan Webber, Ben Allanach, Kosuke Odagiri, Peter Richardson, Stephen Haywood and RD Schaffer for their help and guidance on simulation and theory related topics.

I am grateful to PPARC, Trinity College and the Cambridge HEP Group for funding my PhD and travel to numerous courses, meetings and conferences.

A large number of people have made my stay in Cambridge an enjoyable one. The list is long and includes Ken Wyllie, Bruce Hay, Andrea Biguzzi, Chris Lester and many other members of the HEP group and Trinity College. Thanks also to those who were mad enough to row with me and to both “BA boats” for making coaching such a rewarding experience. Special thanks go to Harriet for her support and encouragement and for keeping me smiling.

Finally, I would like to thank my parents, Jan and Malc, for many years of support and my brother, Trevor, for many cheery emails. I dedicate this thesis to my parents.

Declaration

This dissertation is the result of my own work except where explicit reference is made to the work of others and has not been submitted for another qualification to this or any other university.

L. M. Drage

Contents

List of Figures

List of Tables

Chapter 1

Introduction

ATLAS (**A** **L**arge **T**oroidal **LHC** **A**pparatu**S**) [1] is a particle detector which will surround one of the interaction points of the Large Hadron Collider (LHC) [2] at the European Centre for Particle Physics (CERN). This thesis can be divided into two parts: a study of prototypes of a small component detector of ATLAS and a study of the discovery potential of the detector as a whole.

This introduction has two main aims: to explain the motivations for building the LHC and to describe the design of the ATLAS detector. To explain why the LHC is needed, the Standard Model, the current theory of fundamental particles and interactions, is outlined in section 1.1. The problems and theoretically motivated extensions of the theory are then discussed. Sections 1.4-1.6 describe the LHC and the ATLAS detector. Finally, a brief outline of each chapter of this thesis is given.

1.1 The Standard Model

There are four known fundamental forces in nature: electromagnetic, weak, strong and gravitational. The interactions of particles via the first three of these forces are described by the Standard Model (SM) [3–5]. To date, no experimental evidence has been found to contradict the SM[a] [6, 7]. There are, however, reasons to believe that the SM is not the ultimate description of fundamental particles and interactions. Nor has the SM been totally verified; the sector of the theory responsible for particle masses remains untested.

The SM classifies particles as being either matter particles or force mediating particles. Fundamental matter particles have a spin of one-half and are called fermions. The exchange of spin-one gauge bosons mediates forces between fermions.

Force	Gauge bosons	Mass (GeV)
Electromagnetic	Photon (γ)	0
Weak	$W^{\pm}$, Z	$m_W = 80.22$, $m_Z = 91.19$
Strong	Gluons (g)	0

Table 1.1: The three fundamental forces described by the SM and the associated gauge bosons.

The three forces of the SM and the associated gauge bosons are summarised in table 1.1. The electromagnetic force is mediated by the exchange of massless photons. Only charged fermions interact electromagnetically. All particles interact via the weak force which is mediated by three massive gauge bosons, $W^{\pm}$ and Z, which carry charges of $\pm e$ and 0 respectively, where e is the electronic charge. The strong force is felt by any particle carrying a colour charge. There are three types of colour charge denoted red, green and blue. The gluon, the mediating gauge boson of the strong force, is massless and carries two colour charges.

The fermions of the SM are either quarks, which carry a single colour charge, or

[a] Recent experiments have provided evidence for neutrino oscillations and hence neutrino mass. In the SM, neutrinos are massless but massive neutrinos could be incorporated into the theory without making fundamental changes.

Fermion	Charge	Family 1	Family 2	Family 3
Quarks	2/3	up (u)	charm (c)	top (t)
	$-1/3$	down (d)	strange (s)	bottom (b)
Leptons	-1	electron (e^-)	muon (μ^-)	tau (τ^-)
	0	electron-neutrino (ν_e)	muon-neutrino (ν_μ)	tau-neutrino (ν_τ)

Table 1.2: The fermions of the SM.

leptons, which do not interact strongly. There are six quarks and six leptons, each of which has an associated antiparticle. The fermions are summarised in table 1.2.

The leptons comprise three charged and massive particles, the electron, muon and tau, and three massless and uncharged neutrinos. Weak interactions can be used to classify leptons into three families, each containing a massive lepton and a neutrino. Only leptons in the same family interact weakly with one another.

The six quarks are named up, down, charm, strange, top and bottom. Like leptons, the quarks can be classified into three families. A quark couples via the weak force most strongly, but not uniquely, to the other quark of the same family. Hence, unlike leptons, quarks are not eigenstates of the weak force. The Cabbibo-Kobayashi-Maskawa (CKM) matrix describes the family mixing of the weak force in the quark sector.

Mathematically, the SM is a collection of quantum field theories (QFT). Quantum electrodynamics (QED) describes the electromagnetic force and quantum chromodynamics (QCD) the strong force. The electromagnetic and weak forces are described by a unified electroweak theory.

The Lagrangians of SM QFTs are invariant under local unitary transformations. If $\psi(x)$ is a field describing a fermion, such a transformation is given by:

$$\psi(x) \rightarrow \psi'(x) = U(x)\psi(x) \tag{1.1}$$

The transformation, $U(x)$, is local because it depends on x. The Lagrangian of a free fermion is not invariant under a local transformation. The Lagrangian can, however, be made invariant by introducing one or more vector fields. The vector fields represent the gauge bosons of the theory. Thus, requiring the local invariance of a free particle Lagrangian produces a Lagrangian of interacting particles. The electroweak force is invariant under $SU(2)_L \times U(1)$ and QCD has an $SU(3)$ symmetry. The SM is therefore invariant under $SU(3) \times SU(2)_L \times U(1)$.

The above described SM has been tested extensively. No experimental evidence has been found to disprove it. One part of the theory, the Higgs sector, has however not been directly verified. The Higgs sector [8, 9] comprises a two-component complex scalar field which was postulated to give mass to the weak gauge bosons but is also responsible for fermion masses. The Higgs mechanism also predicts the existence of a scalar particle, the Higgs boson, which has not yet been observed. Fits to precision electroweak measurements yield a Higgs mass of $m_H = 76^{+85}_{-47}$ GeV, where the limits are 68% confidence limits (CL) [10]. The 95% upper CL obtained from the same data is 220 GeV [11]. Direct Higgs searches at the Large Electron Positron (LEP) collider provide a lower mass limit of $m_H > 89.7$ GeV (95% CL) [12].

Another area of the SM which remains to be tested with precision measurements is CP-violation. If a particle and its antiparticle decay in identical ways then the decay is said to be invariant under charge conjugation (C). A fermion can be expressed in terms of left and right components. An interaction which is different for otherwise identical left and right-hand components is said to violate parity (P). If an interaction is equally probable in both time directions, that is with time running forwards and reversed, then time (T) is conserved. Strong and electromagnetic interactions conserve C, P and T. The weak force, however, violates C and P. A combined parity and charge symmetry (CP) is almost conserved. CP violation is incorporated in, but not explained by, the SM.

The small asymmetry between matter and antimatter is postulated to be responsible for the dominance of matter over anti-matter in the universe. CP-violation in the kaon system is currently being studied at purpose built experiments (NA48 [13], KTeV [14]). CPT is believed to be conserved for all three forces.

In total, the SM has 19 free parameters which must be determined experimentally.

1.1.1 Shortcomings of the SM

The SM cannot be the ultimate theory of fundamental interactions for several reasons:

- The SM has 19 free parameters. Other quantities, such as the number of families of fermions, must also be determined empirically. An ultimate theory would predict the values of such parameters.

- The SM does not include gravity. At energies of ~100 GeV, gravitational interactions are insignificant compared to other forces. However, at the Planck scale[b], M_P, gravity does become important. The SM cannot therefore be the description of fundamental interactions at arbitrary energy.

- All particles in the SM have masses of approximately 100 GeV or less. It would be very surprising if no particles existed with a mass between 100 GeV and M_P.

- The hierarchy problem. One-loop corrections to the Higgs mass-squared, Δm_H^2, are quadratically proportional to Γ_{UV}, the ultra-violet cut off of the theory. Γ_{UV} is interpreted as the mass scale at which new physics becomes important. If $\Gamma_{UV} \sim M_P$, the one-loop correction to the Higgs mass for the process $H \to t\bar{t} \to H$ is 10^{30} [7] times greater than the expected Higgs mass. The hierarchy problem is

[b] $M_P = (8\pi G)^{-\frac{1}{2}} = 2.4 \times 10^{18}$ GeV

not automatically solved by introducing new physics at a scale below M_P because Δm_H^2 has contributions proportional to the mass-squared of the heaviest particle in the theory. The coupling between the Higgs field and SM particles is proportional to the Higgs mass. If $m_H \sim M_P$, one would expect SM masses to be of a similar magnitude. The hierarchy problem is succinctly stated by the question; why are M_W and M_P so different?

Many of the problems of the SM can be solved by introducing a new symmetry: supersymmetry (SUSY).

1.2 Supersymmetry: An extension of the SM

In supersymmetric extensions of the Standard Model, a symmetry between fermions and bosons is added to $SU(3) \times SU(2)_L \times U(1)$. Each SM particle acquires a supersymmetric partner, or superpartner, with the same electric charge, weak isospin and number of colour degrees of freedom but with spin differing by one half. The superpartner of a fermion is therefore a boson and vice versa. Leptons have spin-zero superpartners called sleptons (scalar leptons) and quarks are associated with squarks (scalar quarks). Gauge and Higgs bosons have spin-half superpartners called gauginos and higgsinos respectively.

The quadratically diverging one-loop corrections to m_H^2 which lead to the hierarchy problem have opposite signs for fermions and bosons. If one postulates a fermionic partner for each boson and a bosonic partner for each fermion, i.e. introduce supersymmetry, these quadratic divergences can be made to naturally cancel. Other theories which overcome the hierarchy problem can be constructed. SUSY, however, is the most favoured because physics at SM energies is left unchanged. Supersymmetric models also allow the inclusion of gravity [7].

Supersymmetry must be broken since otherwise a SUSY particle would have exactly the same mass as its SM partner, and this is not observed experimentally. To break SUSY a soft SUSY-breaking term is added to the Lagrangian. The split in energy between a particle and the associated sparticle is of order $m_{\rm soft}$. One loop corrections to m_H^2 due to SUSY breaking are of order $m_{\rm soft}^2$. To avoid reintroducing the hierarchy problem, $m_{\rm soft}$ cannot be too large and the lightest SUSY particles should have a mass of order 1 TeV or less. If SUSY is the solution to the hierarchy problem, at least some SUSY particle masses should be low enough for the theory to be discovered at the LHC.

No evidence for SUSY has yet been found. Lower mass limits (95% CL) on the lightest supersymmetric particle (LSP) of between 23.4 GeV and 32.3 GeV have been determined by the four LEP detectors [15]. Lower mass limits (95% CL) on squark and gluino masses of approximately 250 GeV have been obtained by the D0 and CDF experiment at the Tevatron [16–18].

1.3 Signatures of new physics

A detector designed to search for new physics must be able to detect a wide range of signatures. If the SM Higgs boson exists, the decay mode in which it is most easily observed depends on its mass. Details of Higgs production cross sections and branching fractions can be found in [19]. Table 1.3 lists some Higgs decay channels and the Higgs mass ranges in which they are dominant. From the range of possible signatures it can be seen that ATLAS must offer good electromagnetic calorimetry, lepton identification and tracking, jet reconstruction and b-tagging[c]. A detailed analysis of the detection of the SM Higgs boson in ATLAS is presented in [20].

[c] b-tagging is the identification of jets initiated by b-quarks

Decay channel	Mass range (GeV)
$H \to b\bar{b}$	$80 < m_H < 100$
$H \to \gamma\gamma$	$90 < m_H < 150$
$H \to ZZ^* \to 4l^\pm$	$130 < m_H < 2m_Z$
$H \to ZZ \to 4l^\pm,\, 2l^\pm 2\nu$	$m_H > 2m_Z$
$H \to WW \to l^\pm \nu$ 2 jets	$m_H > 2m_W$
$H \to ZZ \to 2l^\pm$ 2 jets	$m_H > 2m_Z$

Table 1.3: Decay modes of the SM Higgs boson [1]. m_Z is the mass of the Z boson.

The signatures of SUSY depend heavily on the specific model [21–25] . In scenarios where the LSP is weakly interacting and stable, the accurate measurement of missing transverse energy is essential. Good jet reconstruction, accurate measurement of high momentum leptons and good b-jet tagging are also important. Numerous studies of the ability of the ATLAS detector to measure SUSY parameters can be found in [20].

1.4 The LHC

The LHC is a proton-proton collider which will begin operation in 2005. The accelerator will be constructed in the tunnels housing the existing LEP collider at CERN (figure 1.1). Protons are collided instead of significantly lighter leptons because the energy losses due to synchrotron radiation are proportional to M^{-4}, where M is the mass of the accelerated particle. The disadvantage of using protons is their composite nature which leads to more complicated events than seen in LEP detectors. The energy of a proton is shared by its constituent quarks and gluons. To ensure that collision energies within the range of expected new physics are achieved, 7 TeV proton beams will be collided. The LHC will initially operate at a luminosity of 10^{33} cm^{-2} s^{-1} and will increase over three years to a higher luminosity of 10^{34} cm^{-2} s^{-1}. The unprecedented

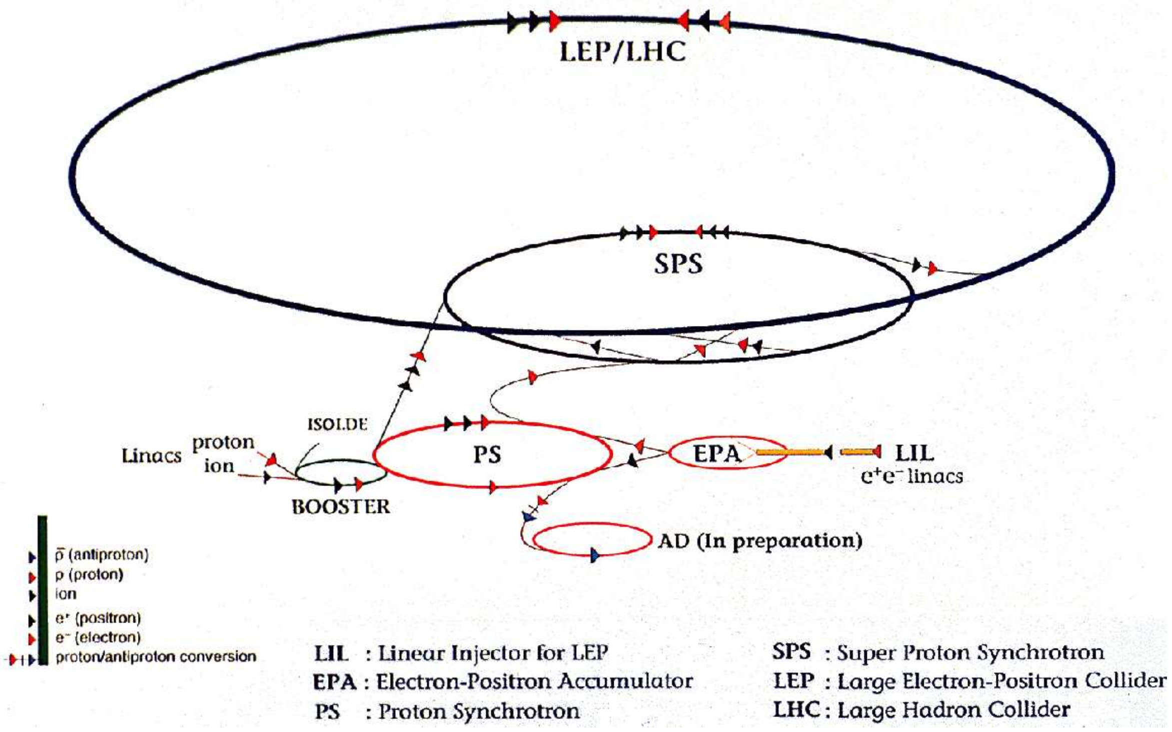

Figure 1.1: The CERN accelerators.

high luminosity of the LHC is required because of the low cross sections of predicted new physics such as Higgs production.

There will be four interaction points on the LHC ring, each surrounded by a detector. The general purpose detectors, ATLAS and CMS (Compact Muon Solenoid) [26], will be built at two interaction points. Both detectors are designed to study a wide range of signatures and will be used in further tests of the SM and in new physics searches. b-quark production rates at the LHC will be high and a third detector, LHC-B [27], will concentrate on CP-violation in B-mesons. The fourth interaction point will be surrounded by ALICE (A Large Ion Collider Experiment) [28] which will investigate heavy ion collisions.

1.5 Variable definitions

Before describing the ATLAS detector it is useful to define some variables. In the following definitions the Cartesian coordinate axes are oriented with the z-axis anti-parallel to one of the incoming beams and with the origin at the interaction point.

A point described by a Cartesian position vector, $\vec{a} = a_x\hat{x} + a_y\hat{y} + a_z\hat{z}$ can be described by coordinates (z, ϕ, η) which are defined:

$$\phi = \arctan\left(\frac{a_y}{a_x}\right) \tag{1.2}$$

$$z = a_z \tag{1.3}$$

$$\theta = \arccos\left(\frac{a_z}{\sqrt{a_x^2 + a_y^2 + a_z^2}}\right) \tag{1.4}$$

$$\eta = -\ln\left(\tan\left(\frac{\theta}{2}\right)\right) \tag{1.5}$$

If a particle has a momentum given in Cartesian coordinates by $\vec{p} = p_x\hat{x} + p_y\hat{y} + p_z\hat{z}$ then ϕ and η are similarly defined. In addition,

$$p_T = \sqrt{p_x^2 + p_y^2} \tag{1.6}$$

1.6 The ATLAS detector

The ATLAS detector, shown in figure 1.2, will be 22 m high, 44 m long and will weigh around 7000 tons. The detector has three distinct sub-systems which, in order of increasing distance from the beam pipe, are: an inner tracker, a calorimeter and a muon spectrometer. The Inner Tracker, also known as the Inner Detector, will provide

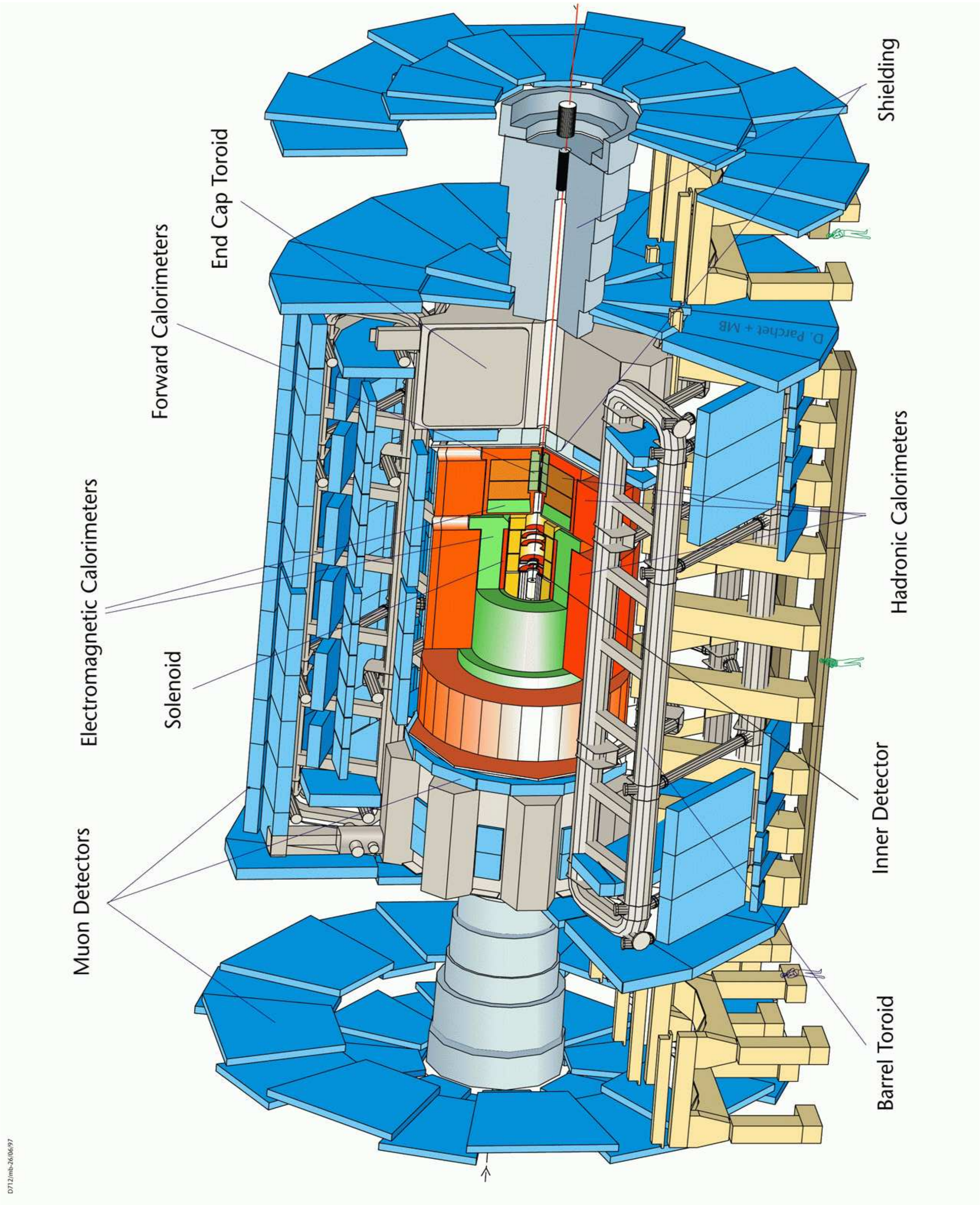

Figure 1.2: The ATLAS detector.

precision tracking of charged particles. The calorimeters will measure the energy and position of most particles which interact electromagnetically or via the strong force. The muon spectrometer will provide tracking for muons. Each sub-system is generally composed of a cylindrical "barrel" region, centred on the interaction point, and "end-cap" regions at either end of the barrel.

The Inner Detector and Muon Spectrometer determine the momentum of a particle by measuring its deflection in a magnetic field. The magnetic field of the Inner Tracker is solenoidal with a field strength of 2 T. The field of the Muon Spectrometer is provided by a barrel and two end-cap toroids. The maximum fields in these toroid magnets are ~3.9 T and ~4.1 T respectively.

1.6.1 The Inner Detector

The energy measurement of particles in ATLAS is degraded by material before the calorimeters. The Inner Detector [29, 30] must therefore satisfy the conflicting requirements of minimal material content and precision tracking in a high multiplicity environment.

Three technologies are used in the Inner Detector. Pixelated silicon detectors are used in the Pixel Detector which surrounds the interaction point. The SemiConducting Tracker (SCT) surrounds the Pixel Detector and employs silicon microstrip detectors. Gas filled straw detectors are used in the Transition Radiation Tracker (TRT), the outer most part of the Inner Detector. The three sub-detectors of the Inner Detector are shown in figure 1.3 and described in more detail below.

Figure 1.4 shows a simulation of the decay $H \rightarrow ZZ^* \rightarrow \mu^+\mu^-e^+e^-$ in the Inner Detector barrel. The plot emphasises the high multiplicity nature of the environment in which the Inner Detector must operate.

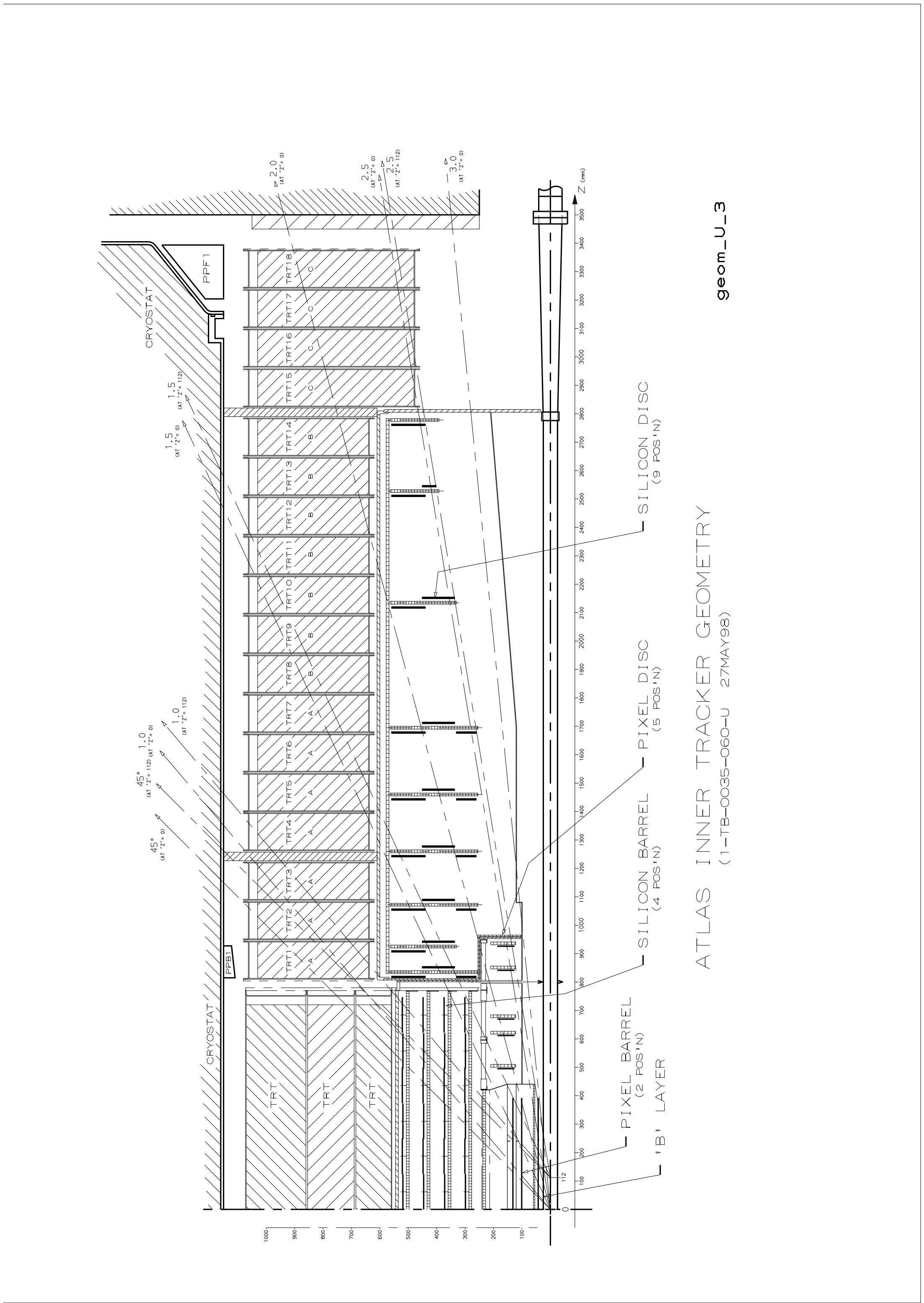

Figure 1.3: A section through a quarter of the Inner Detector. The Inner Detector geometry has been modified since the drawing of this figure in May 1998. In the current geometry, all five pixel disks have a z-coordinate less than 80 cm and therefore extend no further in z than the SCT barrel.

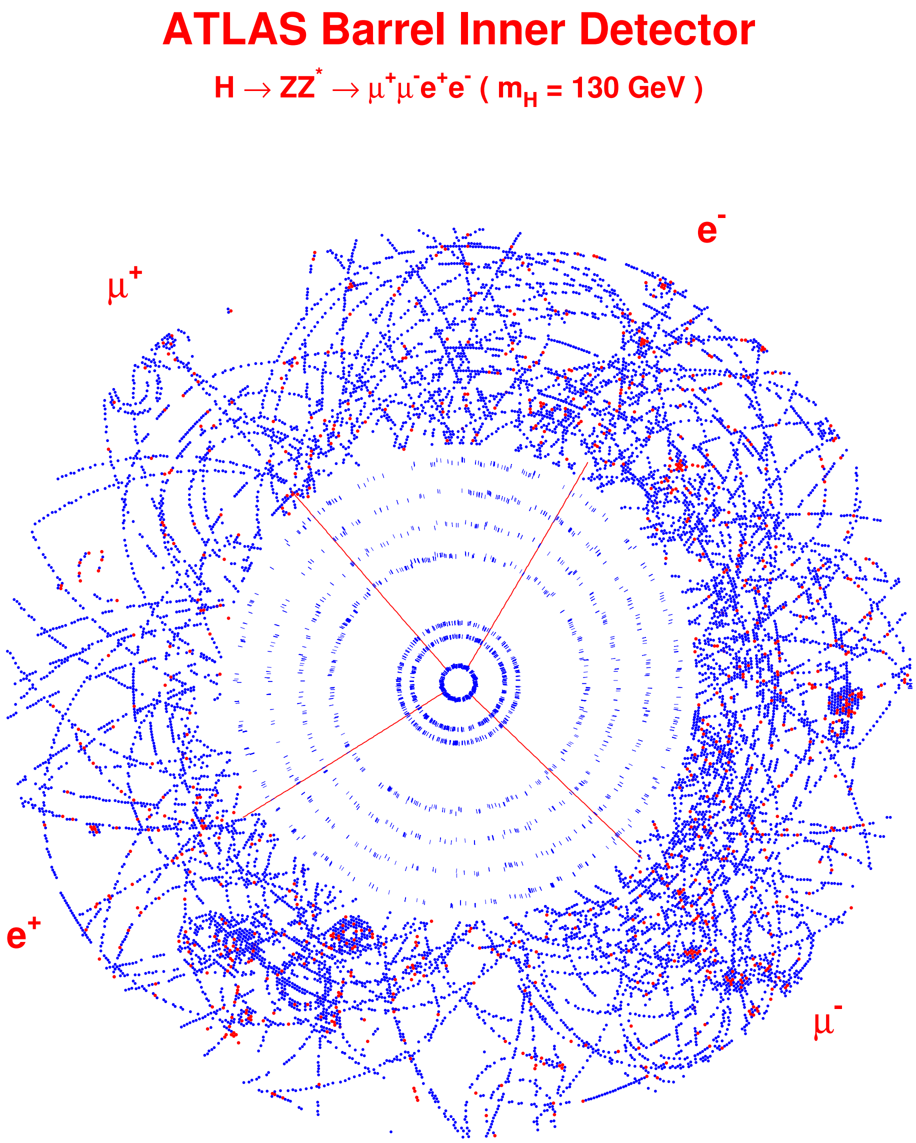

Figure 1.4: A simulation of the decay $H \rightarrow ZZ^* \rightarrow \mu^+\mu^-e^+e^-$ in the Inner Detector barrel [29].

For reasons explained in Chapter 2, the pixel and silicon microstrip detectors will be operated at a temperature of -7^oC. Heat will be removed from detectors directly by a contact cooling system. In addition, a flow of cold, dry nitrogen will be maintained through the thermally insulated SCT and Pixel Detector sub-systems. The TRT will be operated at room temperature. The thermal insulation between the TRT and the inner systems of the Inner Detector can be seen in figure 1.3.

The Pixel Detector

The Pixel Detector is required to give high precision tracking and vertexing in a high occupancy environment. The reconstruction of secondary vertices will be especially important in the tagging of jets from b-quarks. The Pixel Detector and its read-out electronics will operate in a high radiation environment and must be radiation hard. The solution chosen by ATLAS comprises three thin concentric cylinders of sensitive material in the barrel region and ten discs, five either side of the barrel, forming the end-cap regions. The barrel layers are at radii of $\sim$ 4 cm, 10.1 cm and 13.2 cm. The end-cap wheels have z-positions of between 49.5 cm and 77.0 cm. A particle track with $|\eta| < 2.5$ crosses at least three active layers.

The fundamental unit of the pixel barrel is called a module. The active area of a module is a 62.4 mm$\times$24.4 mm silicon wafer which will be between 150 μm and 250 μm thick. The surface of the wafer is implanted with 611440 50 μm$\times$350 μm pixels. The theory of silicon detectors is described in chapter 2. 16 read-out chips are bump-bonded to the wafer surface. The end-cap wafers are of similar dimensions but tapered to allow a concentric arrangement.

Approximately 1500 barrel and 1000 end-cap modules will be used to construct the Pixel Detector. The long side of the pixels is aligned axially and radially in the barrel and end-cap detectors respectively.

The SCT

The barrel SCT is composed of four cylinders of modules at radii between 30 cm and 50 cm. The forward SCT comprises nine wheels either side of the barrel at distances between 83.5 cm and 278.8 cm from the interaction point. The SCT provides tracking in the range $|\eta| < 2.5$.

Modules of a single design are used to populate the whole SCT barrel (figures 1.5 and 1.6). Four 6.36 cm$\times$6.40 cm$\times$300 μm silicon wafers are used to construct each module. Each wafer is implanted with 768 read-out strips which are approximately 6 cm long and have a pitch of 80 μm. Pairs of wafers are placed end-to-end and bonded together to give 12.6 cm long strips. In a module, two pairs of wafers are placed one above the other. The upper wafers are rotated by a 40 mrad stereo angle with respect to the lower wafers. When placed in the SCT, the strips of the lower wafers are parallel to the beam. The two planes of detectors allow the r-ϕ and z coordinates of a track to be measured.

Beryllia (BeO) is used in the support frame of a module because of its mechanical rigidity and high thermal conductivity. Heat is conducted from the detectors to cooling pipes initially by the BeO support frame and then by highly thermally conductive pyrolytic graphite (TPG). The read-out electronics are placed on two BeO hybrids which bridge the silicon wafers on either side of the module.

Three different modules are used in the forward SCT. These are referred to as inner, middle and outer ring modules. Each module is trapezoidal in shape. The middle and outer ring modules are composed of four wafers in a similar arrangement to the barrel module. Figure 1.7 shows a middle ring module. The inner ring module is composed of two back-to-back silicon wafers.

Chapters 2-4 of this thesis describe the operation, design and evaluation in a test beam of SCT barrel modules.

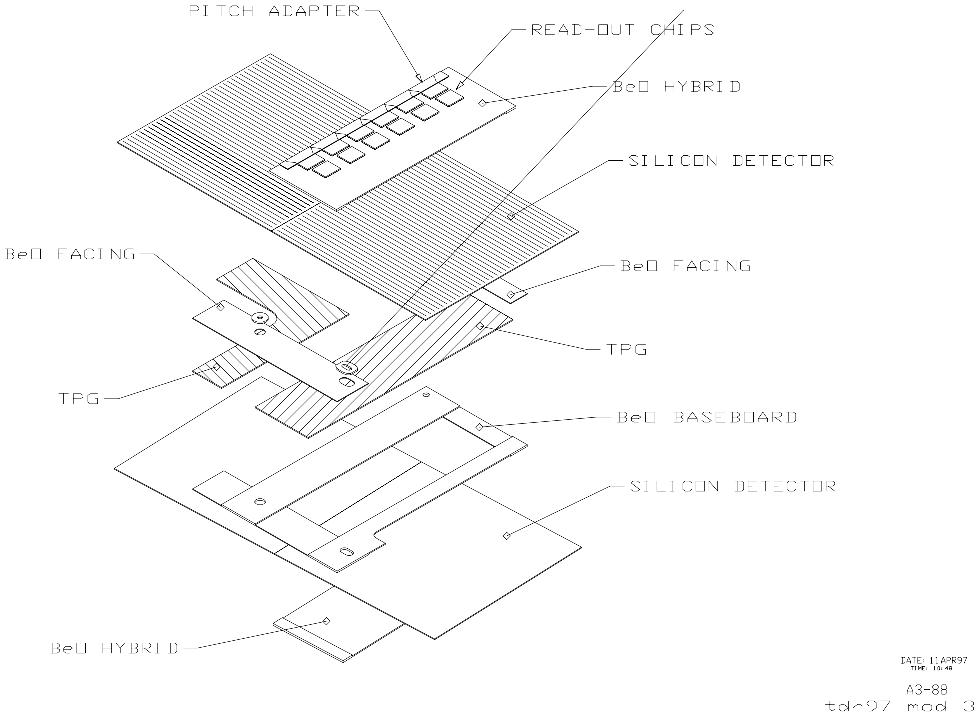

Figure 1.5: An expanded view of an SCT barrel module (from [30]).

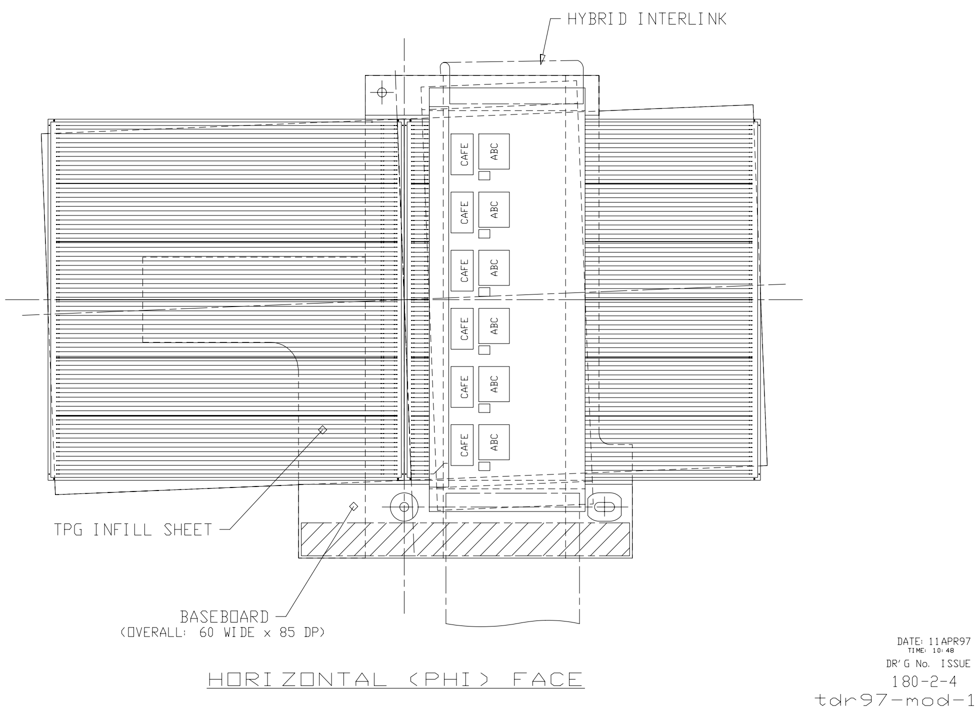

Figure 1.6: An SCT barrel module. The stereo rotation of the lower wafer can be seen (from [30]).

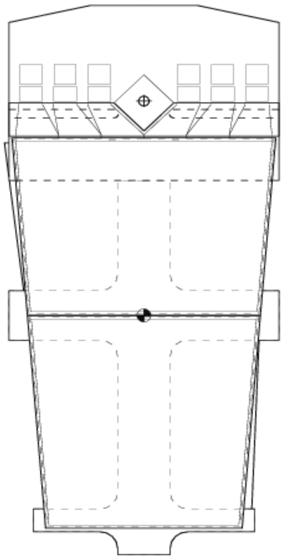

Figure 1.7: An SCT ‘middle ring’ end-cap module (from [30]).

The TRT

The detecting component of the TRT is a gas filled straw detector. The straws have a diameter of 4 mm and a length between 39 cm and 150 cm depending upon their position in the detector. A thin wire extends through the centre of the straw and forms the detector anode. The conductive wall of the straw acts as the cathode. The straw is filled with a 70% Xe + 20% CF_4 + 10% CO_2 gas mixture. Ionising radiation traversing the straw produces free charge in the gas which drifts under the action of an applied electric bias and is collected at the anode.

The barrel TRT is constructed from around 53000 axially oriented straws. The 320000 straws of the end-cap are oriented radially. Around 36 straws are crossed by a particle with $|\eta| < 2.5$ and $p_T > 0.5$ GeV.

The space between straws is filled with polypropylene/polyethylene fibres. Electrons traversing these fibres emit transition radiation (X-rays) which are detected in the straw tubes. Two charge collection thresholds are used in the TRT: a lower threshold, which will be achieved by sufficiently ionising particles, and a higher threshold, which will be reached by electrons and their associated transition radiation. The TRT will thus contribute to electron identification.

1.6.2 Calorimetry

A calorimeter should, ideally, be thick enough to stop all charged and strongly interacting incident particles except muons. Particles lose energy via a variety of processes and create a shower of lower energy particles which in turn interact with the calorimeter. The energy of the shower is equal to the energy of the incident particle. Sampling calorimeters will be used in ATLAS. Active layers, in which the deposited energy is measured, are interleaved with dense absorber layers. The fraction of energy deposited in the active layers can be calculated and used to find the energy of a particle. Segmentation of the active layers allows measurement of a particle's position.

The ATLAS calorimeters will be used to measure the energy and position of electrons, photons and jets. A hermetic calorimeter is essential for measuring the missing transverse momentum of an event. The calorimeter will also be used for triggering.

The ATLAS calorimetry system is composed of an electromagnetic (EM) calorimeter [32], a hadronic tile calorimeter [33] and a forward calorimeter (figure 1.8). The EM calorimeter surrounds the Inner Detector and is surrounded by the tile calorimeter.

Liquid argon (LAr) and lead are used as the active and absorber materials, respectively, of the EM calorimeter. The barrel ($|\eta| < 1.475$) comprises three sampling layers. The absorber and active layers in each sampling are folded into an accordion structure which allows a fine granularity whilst maintaining hermeticity. The first sampling is

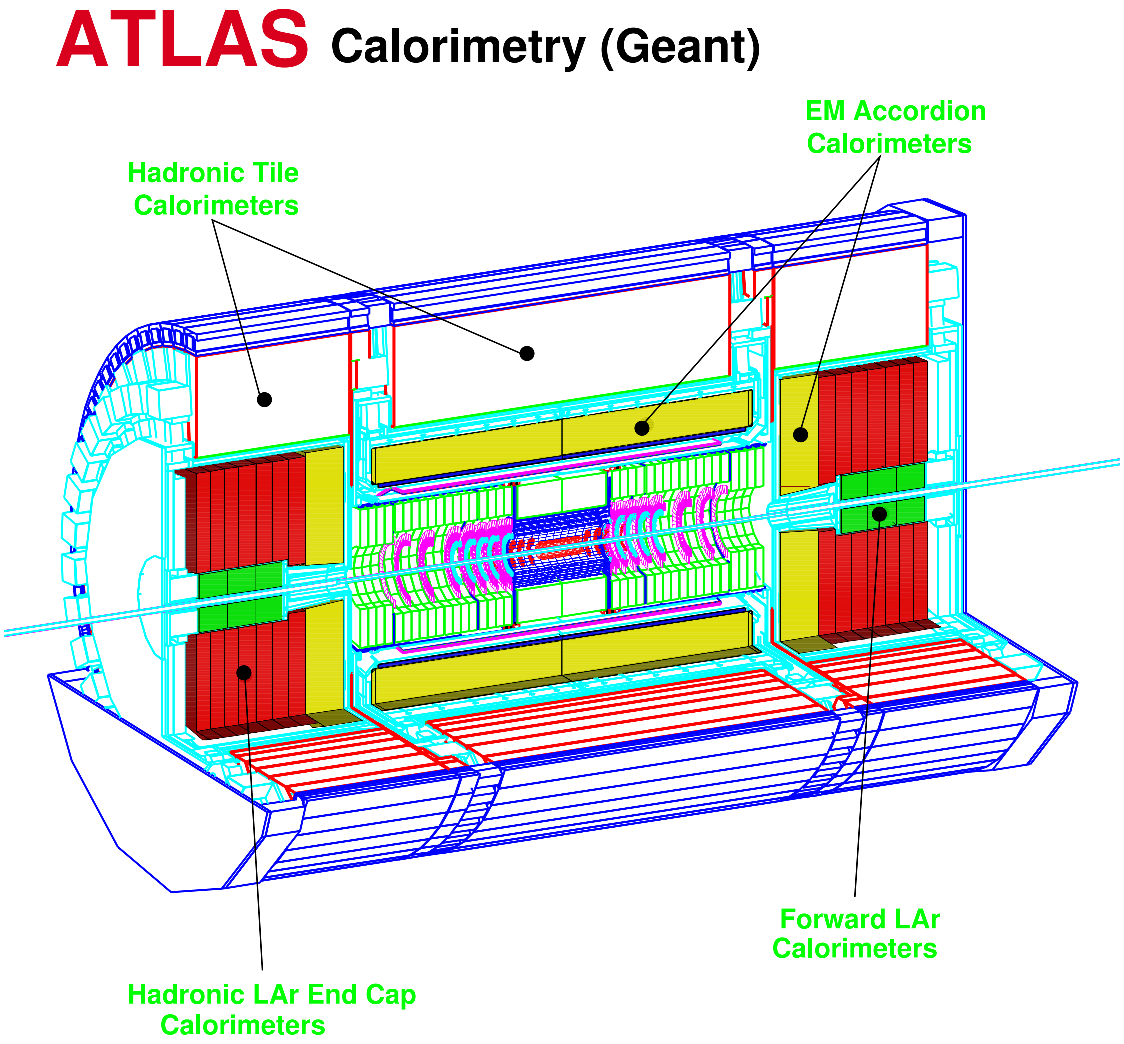

Figure 1.8: The ATLAS system of calorimeters (from [31]).

highly segmented in η to improve the resolution of electron and photon position measurements. The EM end-cap covers the range $1.375 < |\eta| < 3.2$. An additional thin sampling layer, the presampler ($|\eta| < 1.8$), is placed in front of the EM barrel and corrects for energy lost in material upstream of the calorimeter. The EM calorimeter is enclosed by a barrel and two end-cap cryostats.

Scintillating tiles are used as the active material in the hadronic calorimeter barrel ($|\eta| < 1.0$) and extended barrel ($0.8 < |\eta| < 1.7$). Iron is used as the absorber material. There are three sampling layers of granularity $\Delta\eta \times \Delta\phi = 0.1 \times 0.1$, 0.1×0.1 and 0.2×0.1. Liquid argon and lead are used in the hadronic end-cap calorimeter ($1.5 < |\eta| < 3.2$). The active material of the forward calorimeter ($3.1 < |\eta| < 4.9$) is liquid argon. Copper and tungsten are used as absorber materials.

1.6.3 The Muon Spectrometer

The precision detection of muons is essential to the detection of Higgs, SUSY and other new physics. The trajectory of muons in the air core toroids will be measured by monitored drift tubes over most of the range of the spectrometer ($|\eta| < 2.7$). Cathode strip chambers will provide a finer granularity for $|\eta| > 2$. The Muon Spectrometer [34] will have a trigger system independent of the rest of the ATLAS detector. Resistive plate chambers and thin gap chambers will provide the trigger.

1.7 This thesis

Chapters 2-4 of this thesis are concerned with SCT silicon microstrip detectors.

Chapter 2 introduces some basic semiconductor physics and describes the operation of a generic silicon microstrip detector. SCT detectors must detect non-normally incident particles in a magnetic field and in a high radiation environment. The impact of these constraints on detector design is described. In 1997, the ATLAS Collaboration had not decided on the design of SCT microstrip detectors. The final section of chapter 2 outlines the two detector technologies being considered.

During the minimum lifetime of the ATLAS SCT (10 years), the performance of silicon microstrip detectors will be degraded by a high radiation fluence. Chapter 3 investigates the performance in a test beam of irradiated prototypes of both possible SCT detector technologies. It is shown that both types of detector will perform adequately after 10 years of operation. Based on the results of this test beam and other work, the ATLAS Collaboration decided upon the technology to be used in the SCT.

Two prototypes of the chosen SCT technology were evaluated in a second beam test, described in chapter 4. The performance of irradiated and unirradiated prototypes in a magnetic field and with non-normally incident particles is investigated. Once again, the prototypes are shown to perform to specification.

Chapter 5 considers the performance of ATLAS as a whole. As was discussed earlier in this introduction, SUSY is a favoured extension of the SM. In most studies of the SUSY discovery potential of ATLAS, it is assumed that a discrete symmetry, R-parity, is conserved. There are, however, no theoretical or empirical reasons for R-parity conservation. Chapter 5 investigates the ability to measure sparticle masses in an R-parity violating scenario. The SUSY model, event generator and ATLAS simulation are described in the first section of the chapter. The measurement of three sparticle masses is then demonstrated. The error on these measurements is shown to be dominated by jet-energy calibration errors.

Chapter 6 summarises the work presented in this thesis.

Chapter 2

Silicon Microstrip Detectors

Silicon has been chosen as the active material of the ATLAS SCT. The first part of this chapter describes the physics of silicon. The second section focuses on the silicon p-n junction which is the fundamental element of any silicon detector. The behaviour of radiation damaged silicon has strongly influenced the design of ATLAS silicon detectors and is considered in the third section. The final part of this chapter describes two generic types of silicon detector which, in 1997, were being considered for use in the ATLAS Inner Detector.

2.1 The physics of silicon

Silicon is an element found in Group IV of the periodic table. It crystallises into a diamond structure with each silicon atom bonding covalently to its four nearest neighbours. In the crystalline form, silicon is a semiconductor.

The electron energy levels of a pure, or intrinsic, silicon crystal are grouped into bands separated by gaps devoid of energy levels. The valence band is the highest energy band that is occupied at absolute zero. In silicon, it is completely full when all electrons are in their lowest possible energy state. The conduction band, the next group of electron energy levels above the valence band, is unoccupied at absolute zero.

The band gap energy, E_g, is the energy difference between the top of the valence band and the bottom of the conduction band. In semiconductors, the band gap energy is smaller than in insulators[a] and valence band electrons can be excited into the conduction band with comparatively little energy. The promotion of electrons into the conduction band creates positively charged states in the valence band. These states can be treated as particles of positive charge $|e|$ called holes.

Conduction band electrons and valence band holes are mobile and when either are present silicon behaves as a conductor. The electron and hole mobilities, μ_e and μ_h, are defined by:

$$|\mathbf{v_e}| = \mu_e |\mathbf{E}| \tag{2.1}$$

$$|\mathbf{v_h}| = \mu_h |\mathbf{E}| \tag{2.2}$$

where $\mathbf{v_e}$ and $\mathbf{v_h}$ are the electron and hole drift velocities when there is an electric field $\mathbf{E}$ in the silicon. If the densities of conduction band electrons and valence band holes are n and p respectively, the net current density is

$$\mathbf{j} = n(-e)\mathbf{v_e} + pe\mathbf{v_h} = (n\mu_e + p\mu_h)e\mathbf{E} \tag{2.3}$$

which is Ohm's law with conductivity,

$$\sigma = (n\mu_e + p\mu_h)e \tag{2.4}$$

Equation 2.4 shows that the conductivity of silicon can be improved by increasing hole or electron concentrations. This is achieved by introducing a small amount of an impurity

[a] E_g = 1.11 eV in silicon at 300K [35]. Silicon dioxide (SiO_2), an insulator, has a band gap energy of 8.8 eV

into the crystal which is known as doping. The resulting impure silicon is said to be extrinsic.

When silicon is doped with a group V element such as phosphorus or arsenic, the impurity atoms replace silicon atoms at a small number of crystal lattice sites. Each impurity atom has five valence electrons, four of which participate in lattice bonds. The remaining electron is only loosely bound to the impurity atom and an energy much less than E_g is required to excite it into the conduction band. The doping, therefore, introduces filled donor energy states just below the conduction band. The dopant is known as a donor impurity.

Replacing some lattice silicon atoms with a group III element, which has only three valence electrons, introduces holes into the lattice. These holes are weakly bound to the impurity atom and can easily be excited into the valence band. Equivalently, one can say that the impurity creates electron acceptor levels just above the valence band which, when occupied by valence electrons, create holes in the valence band. The dopant is therefore referred to as an acceptor impurity.

In practice, both donor and acceptor levels are present in extrinsic silicon. When there are more donor than acceptor levels, the majority charge carriers are electrons and the silicon is said to be n-type. When there are more acceptor than donor levels, holes are the majority charge carriers and the silicon is said to be p-type.

The probability of an electron state of energy ϵ being occupied is given by the Fermi-Dirac function:

$$f(\epsilon) = \frac{1}{e^{(\epsilon-\mu)/kT} + 1} \tag{2.5}$$

where T is the temperature in Kelvin, k is Boltzmann's constant and μ is the Fermi

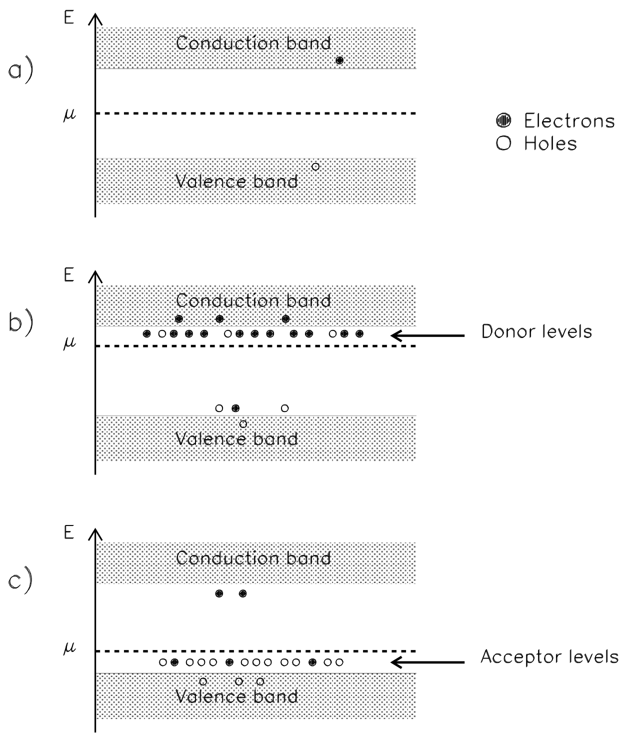

Figure 2.1: Electron energy levels in **(a)** intrinsic, **(b)** n-type and **(c)** p-type silicon.

energy, defined by $f(\mu) \equiv 0.5$. In intrinsic silicon, the Fermi energy is in the centre of the band gap (figure 2.1a). The Fermi energy in n-type silicon is nearer to the conduction band (figure 2.1b) and in p-type silicon it is closer to the valence band (figure 2.1c).

2.2 The p-n junction

When silicon is doped such that a region of n-type silicon is adjacent to a region of p-type silicon, a p-n junction is created. For the p-n junction to be in thermal equilibrium, the Fermi energy must be at the same level on both sides. If this were not the case there would be a net diffusion of holes and electrons across the junction. The equilibrium is achieved by a small transfer of electrons from the n-type to the p-type silicon, where

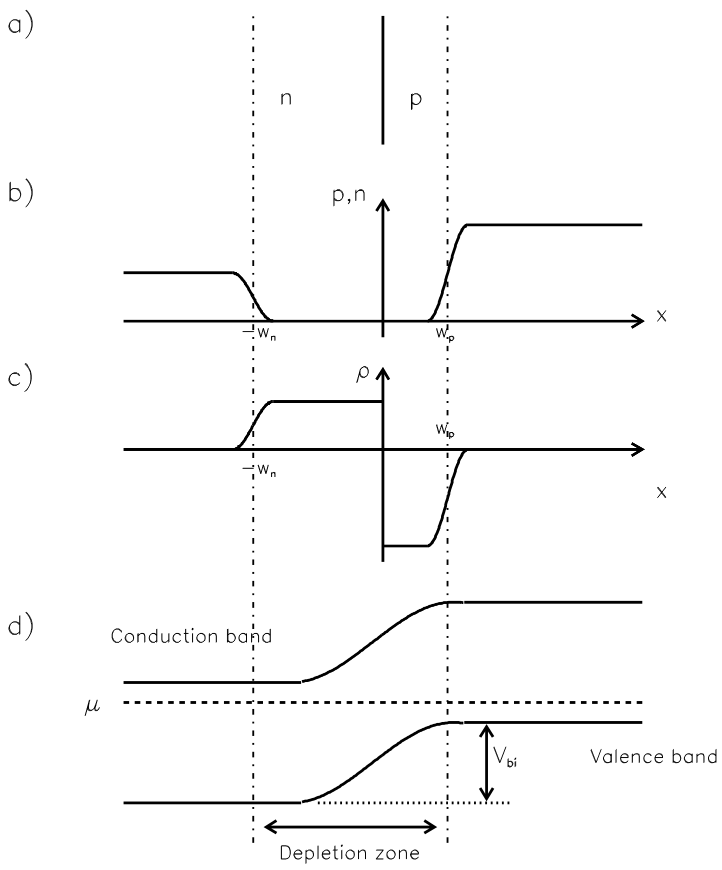

Figure 2.2: **(a)** The p-n junction **(b)** The variation with x, the distance from the junction, of the charge carrier concentration. The p-n junction is at $x = 0$. **(c)** The charge density, $\rho(x)$. **(d)** The bending of the valence and conduction bands. Note that the Fermi energy, μ, is independent of position.

they annihilate with holes. This transfer creates a region either side of the junction devoid of free charge carriers which is called the depletion region (figure 2.2b). The donor and acceptor impurity ions in the depletion region are locked into the lattice and a region of space charge is created (figure 2.2c). The space charge creates a potential difference across the junction which bends the conduction and valence bands as shown in figure 2.2d. To pass from the n to the p side of the junction an electron or hole must overcome a potential step of height V_{bi}, the built-in voltage of the junction.

If a p-n junction is abrupt, the extent of the depletion region in the p-type and n-type silicon, w_p and w_n, can be shown [36] to be:

$$w_n = \sqrt{\frac{2\epsilon_0 \epsilon_{Si} N_A V_{bi}}{e N_D (N_A + N_D)}} \tag{2.6}$$

$$w_p = \sqrt{\frac{2\epsilon_0 \epsilon_{Si} N_D V_{bi}}{e N_A (N_A + N_D)}} \tag{2.7}$$

where N_A and N_D are the concentrations of acceptor and donor impurities respectively and ϵ_{Si} is the permittivity of silicon. In these equations it is assumed that the charge carrier concentration rises sharply at the edge of the depletion region.

p-n junctions of silicon detectors have one side of the junction more heavily doped that the other. In this case, the depletion region extends predominantly into the more lightly doped silicon and has a width:

$$w \approx \sqrt{\frac{2\epsilon_0 \epsilon_{Si} V_{bi}}{e N_{bulk}}} \tag{2.8}$$

where N_{bulk} is the doping concentration of the more lightly doped silicon.

The height of the potential step at the p-n junction can be changed by applying a voltage across the junction. Applying the positive side of the voltage to the p-type silicon decreases the step height and is known as forward biasing. Negative biasing, where the voltage polarity is reversed, increases the potential step height. For a p-n junction with an applied forward bias, V, equation 2.8 becomes:

$$w \approx \sqrt{\frac{2\epsilon_0 \epsilon_{Si} (V_{bi} - V)}{e N_{bulk}}} \tag{2.9}$$

Thus, negative biasing increases the width of the depletion region.

The current flowing across a negatively biased p-n junction is smaller than for a positively biased junction but not zero. This leakage current has several contributing processes. One source is the drift of minority charge carriers. The applied bias acts as a barrier to majority carriers but also increases the flux of minority carriers. Another source of the leakage current is the creation by thermal excitation of majority charge carriers in the depleted region. Electron energy levels near the centre of the band gap also contribute. These are called deep levels and result from crystal imperfections, impurities and damage to the silicon surface. The leakage current increases with increasing reverse bias.

2.3 Silicon detectors

Silicon detectors are p-n junctions operated under reverse bias. One side of the junction is usually much thicker and more lightly doped than the other. The bias voltage is, ideally, large enough to extend the depletion region across the width of the lightly doped silicon. Few mobile charge carriers then remain in the bulk of the detector which is said to be fully depleted. The bias at which full depletion occurs is called the depletion voltage.

A particle traversing a detector creates electron-hole pairs in the depleted bulk. These are separated by the electric field of the applied bias and drift towards the faces of the detector where a charge can be detected. Single sided microstrip detectors have the more heavily doped silicon segmented into long, thin, parallel strips as shown in figure 2.3. Charge is collected on the strips nearest to the particle path. The collected charge is shared across more strips when a particle is incident at an angle. Double sided detectors have strips on both faces and measure two coordinates of a particle track.

The dominant source of energy loss of most relativistic particles is ionisation. The

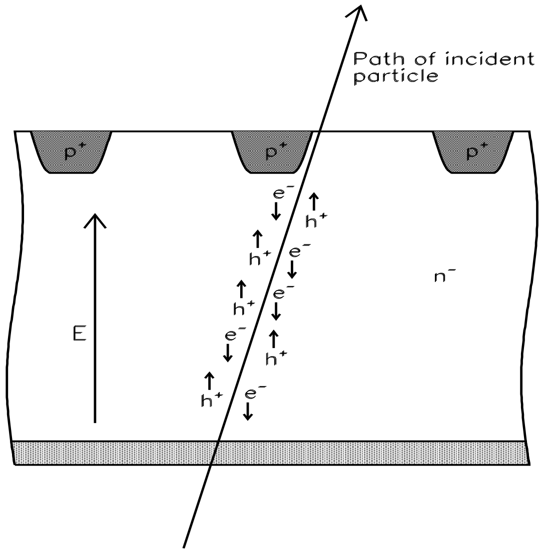

Figure 2.3: A schematic diagram of part of a silicon detector with highly doped p-type strips in an n-type bulk. The three strips extend into the page. The direction of the electric field, E, resulting from reverse biasing is shown. Holes generated by an incident particle drift towards the strips.

mean rate of energy loss by ionisation is described by the Bethe-Bloch equation [37] which, for a given material, depends only on the mass, charge and momentum of the incident particle. In figure 2.4, the rate of energy loss, $-\frac{dE}{dx}$, of particles in silicon is plotted against the ratio of the particle momentum and mass. A particle with momentum near the minimum in the curve is said to be a minimum ionising particle (MIP).

The energy lost by a charged particle traversing a thin piece of material has a Landau distribution [38], the mean value of which is given by the Bethe-Bloch equation. The Landau distribution has a high energy tail and the mean energy and most probably energy deposited in a material are not the same. In 300 μm thick silicon, normally incident MIPs lose a mean energy of 116 keV. The most probable energy lost by a MIP is 90 keV [39]. In silicon, an average energy of 3.6 eV[b] is required to create an electron-hole pair and so the most probable number of electron-hole pairs created is 25000.

[b]1.11 eV is required to promote an electron from the valence to the conduction band. Phonons are created in the silicon lattice by the remaining energy.

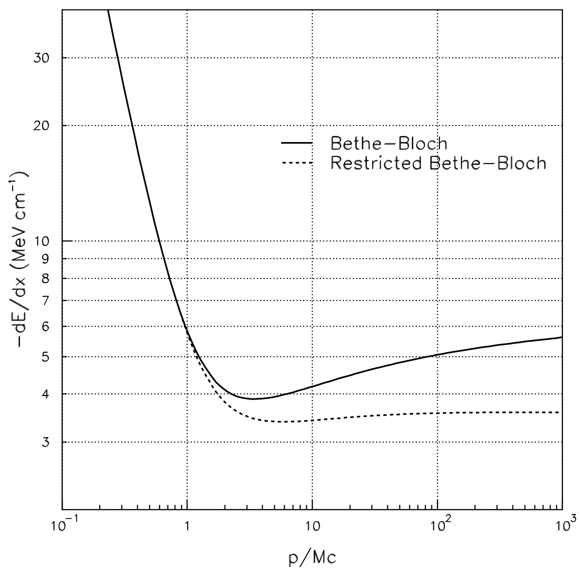

Figure 2.4: The mean rate of energy loss by ionisation with distance, -dE/dx, plotted against the ratio between the momentum, p, and mass, M, of a particle travelling through silicon. The solid line shows the variation predicted by the Bethe-Bloch equation. For a MIP, $-dE/dx = 3.88$ MeV cm^{-1}. At $p/Mc = 1000$, $-dE/dx = 5.62$ MeV cm^{-1}. The dashed line shows the energy loss predicted by the restricted Bethe-Bloch equation which is described in the text. At $p/Mc = 1000$, the mean energy deposited in the silicon, $-dE/dx = 3.58$ MeV cm^{-1}.

The mean energy deposited in a thin section of material has been observed to be lower than the energy lost by the ionising particle [39, 40]. This difference in energy is due to the escape from the material of some ionisation electrons. The effect is most pronounced when the incident particle is highly relativistic. A parameter of the Bethe-Bloch equation is T_{max}, the maximum energy that can be imparted to an electron by the incident particle in a single collision. In the standard Bethe-Bloch equation, T_{max} is determined kinematically. It has been shown [40] that the energy deposited in a material is more closely predicted if T_{max} is reduced to the maximum energy of an electron that will remain in the material. The resulting formula is referred to as the restricted Bethe-Bloch equation and is plotted in figure 2.4 for $T_{max} = 500$ keV.

The charge collection time of a silicon detector decreases with increasing bias voltage. For this reason detectors are, if possible, operated over-depleted, that is with a bias voltage greater than the depletion voltage. In a 300 μm thick silicon detector biased at 300 V, the electron and hole collection times are 8 ns and 25 ns respectively [39].

The depletion voltage of a detector can be reduced by using high resistivity silicon for the detector bulk. In ATLAS, the bulk doping concentration will be $10^{11-12}\mathrm{cm}^{-3}$. The maximum bias voltage of a detector is limited by leakage currents and the risk of avalanche breakdown. The maximum tolerable leakage current is limited by the power supply, heat dissipation of the detector and noise levels in the read-out electronics. Leakage currents increase at higher temperatures. An increase in leakage current may result in more heat dissipation and a further increase in leakage current. The possibility of detector thermal runaway can be minimised by efficiently removing heat from the detector. Avalanche breakdown occurs when the electric field in the detector is so high that electrons in the detector bulk gain enough momentum to cause further ionisations. The voltage at which avalanche breakdown first occurs can be increased by designing the detector geometry to minimise areas of high electric field.

The spatial resolution of a microstrip detector is largely determined by the strip separation or pitch. The resolution of a detector can be defined as the root mean square (RMS) of the distribution of the distance between the particle track and measured position. If a signal is produced only on the strip nearest to a traversing particle, and the measured position is therefore the centre of that strip, the resolution is the strip pitch over $\sqrt{12}$. This resolution can be improved by collecting charge on more than one strip. The techniques available for improving resolution depend on the read-out method employed which may be analogue, digital or binary. In analogue read-out systems a value proportional to the charge collected is recorded. In digital systems the analogue signal is converted into one of several discrete values. A binary system simply returns a 1 or a 0 depending upon whether the charge collected is above or below a certain threshold.

The coupling between the detector strips and the amplifiers of the front end electronics (FEE) can be direct (DC) or analogue (AC). In DC coupled detectors, an amplifier is connected to an aluminium strip laid directly on top of the each strip of heavily doped silicon. A disadvantage of DC coupling is that the leakage current flows through the front end electronics. This current may differ from strip to strip and the calibration of detector read-out is complicated.

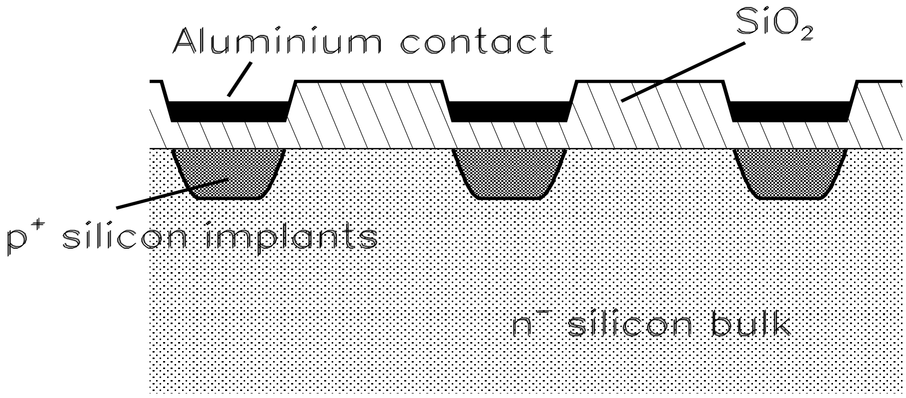

Figure 2.5: The surface of part of an AC coupled detector with p^+ implants in an n^- bulk silicon.

AC coupled detectors have a coupling capacitor between the detector and read-out electronics (figure 2.5). This capacitor is often a metal-oxide-semiconductor (MOS) capacitor fabricated on the detector surface by separating the aluminium contact strip from the silicon by a layer of silicon dioxide. Silicon dioxide is an insulator and forms the dielectric of the capacitor. AC coupled detectors overcome calibration problems due to leakage currents by measuring only a change in current. Shot noise is also reduced because the current flowing through the FEE is smaller. AC coupled detectors do, however, require a more complicated biasing scheme than DC detectors in which the strip bias is provided through the FEE. In AC coupled detectors, the bias must be applied separately via bias resistors which minimise charge loss from the read-out circuit.

The bias voltage and read-out electronics are connected to the non-junction side of a detector by an ohmic connection. Highly doped silicon is first laid down onto the bulk silicon followed by a contact layer of aluminium. The highly doped silicon has the same majority charge carrier as the detector bulk.

2.4 Silicon detectors in a magnetic field

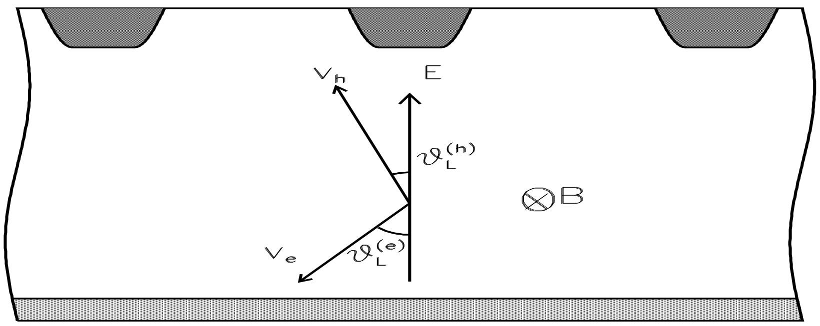

Figure 2.6: The orientation of silicon microstrip detectors in the SCT barrel with respect to the magnetic field, **B**. The direction of hole and electron drift velocities are also shown.

The silicon microstrip detectors of the ATLAS Inner Detector will operate in a 2 Tesla solenoidal magnetic field [29]. Figure 2.6 shows the orientation in the SCT barrel of a microstrip detector with respect to the magnetic induction, **B**. A free hole or electron in the detector bulk is subject to a force $\mathbf{F} = q(\mathbf{E} + \mathbf{v} \times \mathbf{B})$ where q and $\mathbf{v}$ are the charge and drift velocity of the particle and $\mathbf{E}$ is the electric field of the applied bias voltage.

This force has a component parallel to the detector face and $\mathbf{v}$ and $\mathbf{E}$ are not parallel. The Lorentz angle, θ_L, is the angle between the drift velocity and electric field. It is related to the magnetic induction, $\mathbf{B}$, by [41]

$$\tan\theta_L = \mu_H|\mathbf{B}| \tag{2.10}$$

where μ_H is the Hall mobility. At 300K, electrons and holes in high resistivity silicon have Hall mobilities of 0.1560 $\mathrm{m^2V^{-1}s^{-1}}$ and 0.0358 $\mathrm{m^2V^{-1}s^{-1}}$ respectively [35].

Electrons and holes produced by an incident particle drift to the detector faces where a charge can be collected. With no magnetic field, the distribution of collected charge is symmetric and centred around the track of a normally incident particle. In a magnetic field, the distribution centre and particle track no longer coincide because of the lateral drift of charge carriers. The distribution is also wider and skewed because the amount of lateral drift of a hole or electron increases with the depth in the detector at which it was produced [42].

2.5 Radiation damage to silicon

The Inner Detector will operate in a high radiation environment and it is therefore important to understand the behaviour of silicon detectors in such conditions. The expected fluences in ATLAS are discussed in section 2.5.1. Silicon detector studies have shown that damage occurs to both the bulk and the surface of a detector. Sections 2.5.2 and 2.5.3 respectively discuss bulk and surface effects.

2.5.1 ATLAS radiation fluences

The rate at which silicon is damaged by a given fluence of radiation is dependent on the type and energy of the incident particles. Known normalisation functions can be used to express the damage due to a fluence of one type and energy of particle in terms of another [43]. In the ATLAS Collaboration, the contributions from all types of particle are presented in terms of the equivalent fluence of 1 MeV neutrons (abbreviated 1 MeV n cm^{-2}). The highest fluence that will be received by the SCT is estimated to be $(1.4 \pm 0.7) \times 10^{14}$ 1 MeV n cm^{-2} [30].

2.5.2 Bulk damage to silicon

Two measurable effects of bulk damage in silicon detectors are an increase in leakage current and a change in depletion voltage. The increase in leakage current, ΔI, has been found to be directly proportional to the total fluence, ϕ, and is given by

$$\Delta I = \alpha \phi V \tag{2.11}$$

where V is the depleted volume of the detector and the constant of proportionality, α, is known as the damage constant. When leakage currents are measured at 20^{o}C the damage constant for proton irradiation is approximately 3.0×10^{-17} A cm^{-1} [44,45]. The rise in leakage current is due to the creation of energy levels in the middle of the band gap which act as carrier generator centres. After irradiation, a fall in leakage current has been observed [45].

The change in the depletion voltage of a detector during irradiation reflects a change in the donor and acceptor impurity concentrations in the bulk silicon. The effective doping concentration, $N_{eff} = N_A - N_D$, becomes more positive as the donor concentration, N_D, falls and the acceptor concentration, N_A, increases. In n-type silicon, $|N_{eff}|$ first falls to zero and then the silicon undergoes type inversion to p-type. The doping concentration of the p-type silicon then increases. When irradiated at room temperature, type inversion of high resistivity n-type silicon occurs at an approximate fluence of 10^{12} 1 MeV n cm^{-2} [46,47].

The mechanism responsible for the change in effective doping concentration is Non-Ionising Energy Loss (NIEL). In NIEL, incident particles scatter elastically off of lattice silicon atoms. If the energy transferred to the lattice atom is sufficient, the silicon atom can be displaced to an interstitial, a position between lattice sites, leaving a vacancy on the lattice. Interstitials and vacancies are referred to as point defects and at room temperature both are mobile.

At least two complexes involving point defects are thought to be responsible for the change in doping concentration. An IP complex is formed when a phosphorus atom and an interstitial combine. The phosphorus atom in such a complex is unable to act as a donor. The formation of IP complexes is, therefore, postulated to explain the observed fall in donor concentration. A divacancy, a complex of two vacancies, has acceptor like properties. The production of divacancies is thought to explain the rise in acceptor concentration.

The change in N_{eff} with fluence, ϕ, has been parameterised for n-type silicon as [46]:

$$N_{eff}(\phi) = N_o e^{-c\phi} + \beta\phi \tag{2.12}$$

where N_o is the initial doping concentration and c and β are positive and fluence independent coefficients. N_{eff} and N_o have the same sign as the majority charge carrier.

The effective doping concentration continues to change after irradiation has ceased. Immediately afterwards, N_{eff} falls during a period of beneficial annealing before rising once more in an anti-annealing phase. Eventually, N_{eff} reaches a plateau value.

A parametrisation of the variation of N_{eff} with time during beneficial annealing is consistent with the decay of some acceptor states created during irradiation. The time constant of this exponential decay, τ_s, is strongly dependent on temperature, varying as $exp(-A/T)$ where T is the annealing temperature and A is a constant. At 21^{o}C, $\tau_s \approx 2$ days and at 0^{o}C, $\tau_s \approx 67$ days [47].

To explain the anti-annealing of silicon, the creation during irradiation of a third point defect complex is postulated. This complex is initially electrically neutral but becomes electrically active either by decaying [47] or combining with a second, possibly identical, complex [48]. The time constant of anti-annealing is proportional to e^{-aT} where T is the annealing temperature and a is a constant [47]. At 50^{o}C, anti-annealing has a time constant of the order of several days. At 0^{o}C, the time constant is measured in tens of years and anti-annealing is essentially frozen at -7^oC.

2.5.3 Surface damage

The effects of damage by irradiation to a detector surface are strongly influenced by the detector design. As shown in figure 2.5, a passivating layer of SiO_2 covers the surface of many silicon detectors. This oxide layer has a net positive charge which can be reduced, but not entirely eliminated, during the manufacture of the device. Incident particles can create electron-hole pairs in the SiO_2 by promoting electrons from the conduction band to the valence band (E_g = 8.8 eV). Impurities in the SiO_2 can also be ionised to give electron-ion pairs. In the absence of an electric field, the radiation induced electron-hole and electron-ion pairs would normally recombine. In AC-coupled detectors, however, the SiO_2 layer is involved in the MOS read-out capacitors. The electric field across the capacitor separates oppositely charged particles in the oxide. Mobile electrons are removed from the oxide layer but the less mobile ions and holes remain, thus increasing the net positive charge of the oxide. The charge in the oxide layer induces an accumulation layer of electrons in the bulk silicon near the Si/SiO_2 interface. The accumulation layer causes areas of high electric field which increase the risk of avalanche breakdown at a given bias voltage [49].

2.6 ATLAS silicon microstrip detectors

In 1997, two generic types of microstrip detector were being considered for use in the ATLAS Inner Detector: p-in-n and n-in-n detectors.

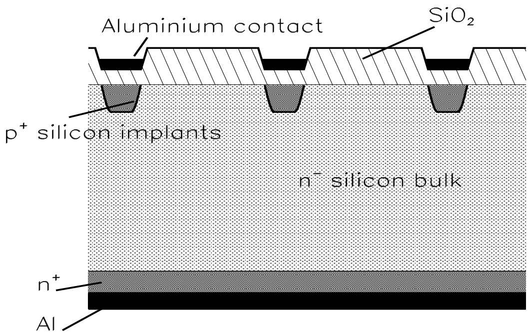

Figure 2.7: A schematic of a p-in-n detector before irradiation

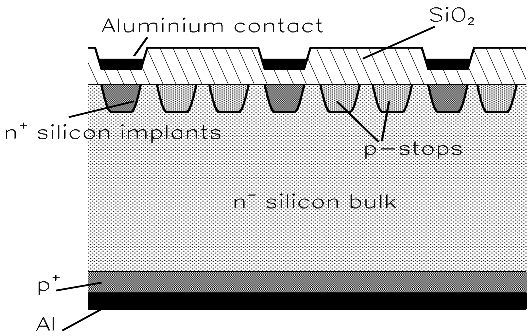

Figure 2.8: A schematic of an n-in-n detector before irradiation

p-in-n detectors (figure 2.7) have highly doped p-type strips on a high resistivity n-type bulk silicon. A layer of n^+-type bulk silicon forms the ohmic connection on the backplane. Before the irradiation induced type inversion of the bulk silicon, the p-n junction is on the strip side of the detector. The depletion region grows from the strips towards the backplane with increasing bias voltage. During irradiation, the lightly doped bulk silicon undergoes type inversion but the n^+ backplane remains relatively unchanged. The depletion region then grows from the p-n junction on the backplane towards the strips. The bulk near the detector strips is depleted only at or above full depletion and so p-in-n detectors should ideally be operated above full depletion. This is not always possible because of the rise in depletion voltage, increase in leakage current and an increased risk of avalanche breakdown. It has been shown that when operated underdepleted, a reduced signal is still produced in the strips by induction across the high resistivity, undepleted bulk [50]. The operation of underdepleted p-in-n detectors is observed in section 3.5.1.

n-in-n detectors (figure 2.8) have n^+ silicon strips in a high resistivity n-type bulk with a p^+ backplane. p-type strips called p-stops are fabricated between the n^+ strips which would otherwise be shorted together by the electron accumulation layer. p-stops are not biased. Before irradiation, the depletion region grows from the backplane and afterwards from the strip side. The detector can therefore be efficiently operated underdepleted after type inversion. A disadvantage of n-in-n detectors is that the fabrication of p-stops requires extra processing steps. There is also a larger voltage drop between strips which can reduce the bias voltage at which avalanche breakdown first occurs [50].

Baseline silicon microstrip detectors for the SCT barrel have 768 read-out strips approximately 22 μm wide and with a pitch of 80 μm. The total area of the 300 μm thick silicon wafers is 64×63.6 mm and the active area covers 62×61.6 mm. In both n-in-n and p-in-n detectors, floating guard rings are fabricated concentrically around the edge of the detector. Without guard rings, the electron accumulation layer prevents the depletion layer extending beyond the edge strips resulting in a large voltage drop and high electric field. When guard rings are used, the depletion region punches through to each in turn and the voltage drop is spread across the extent of the guard rings resulting in a smaller electric field [49]. In ATLAS, detector read-out strips will be capacitively coupled to binary read-out electronics.

The combination of SCT detectors and FEE is referred to as a module. The specifications of SCT modules are defined in [30]. It should be noted that these requirements are based on the operation of n-in-n detectors, the base-line technology when [30] was published. Listed below are the specifications relevant to the analyses presented in the following two chapters. The post-irradiation values are for a fluence of 2×10^{14} protons cm^{-2} (1.4×10^{14} 1 MeV n cm^{-2}). A binary threshold of 1 fC is assumed.

- Maximum operation voltages before and after irradiation should be 150 V and 300 V respectively. The modules should therefore be maximally efficient above these voltages.
- Pre-irradiation total leakage current should be less than 50 nA when measured at -10 °C and at a bias voltage of 150 V.
- Post-irradiation total leakage current should be less than 1 mA when measured at -10 °C and at a bias voltage of 300 V.
- Detection efficiency should be greater than 99%.
- Occupancy due to noise should be less than 5×10^{-4}.

Chapter 3

A test beam comparison of p-in-n and n-in-n detectors

3.1 Introduction

In 1997, the ATLAS Collaboration had not decided whether to use p-in-n detectors or n-in-n detectors in the SCT. A test beam in November 1997 was used to compare the performance of these two detector technologies. The silicon strip detectors of the SCT must operate in a high radiation environment. Thus, in this test beam, the performance of three irradiated n-in-n detectors and three irradiated p-in-n detectors was compared. The first section of this chapter describes the design, irradiation and annealing of the detectors. The test beam apparatus and data analysis are then described. Finally, results for all six detectors are presented.

3.2 The detectors

The three p-in-n and three n-in-n detectors studied were prototypes of silicon strip detectors for the SCT barrel. Each had an active area of 62×61.6 mm^2 and 768 read-out strips of 80 μm pitch. The active area was surrounded by guard rings.

Detector	Supplier	Type	Thickness (μm)	Bias resistors	Passiv.	p-stops	V_d (V)
P1	Eurisys [51]	p-in-n	340	Implant	None	-	43
P2	Sintef [52]	p-in-n	300	Poly.	None	-	55
P3	MPI [53]	p-in-n	280	Implant	None	-	97
N1	Hamamatsu [54]	n-in-n	300	Poly.	Silox	Common	70
N2	Hamamatsu	n-in-n	300	Poly.	Silox	Indiv.	60
N3	Sintef	n-in-n	300	Poly.	None	Indiv.	42

Table 3.1: Details of the six detectors studied in the November 97 test beam. Detector N1 has a novel p-stop design, more details of which can be found in [55]. The right-most column lists the full depletion voltage before irradiation [56]. The column labelled passivation (abbreviated to passiv.) indicates whether the detector surface was passivated.

The detectors were manufactured by four different suppliers and differed in details of passivation, biasing resistors[a], thickness and, in the case of n-in-n detectors, the design of p-stops. The details of each detector are given in table 3.1. All detectors except P3 had strips implanted into an n-type bulk with resistivity, $\rho \sim 5$ kΩ. The bulk material of P3 had a lower resistivity, $\rho \sim 2$ kΩ.

Each detector was glued or clamped in a ceramic frame to facilitate handling during the irradiation and test beam.

[a] Polysilicon bias resistors consist of a polysilicon film fabricated on top of the silicon dioxide. Implant resistors are fabricated by doping a strip of silicon between the detector bias rail and each read-out strip. p-stops can be either individual or common. Individual p-stops consist of isolated rings of p-type implants around each read-out strip. The p-type implants are connected together when common p-stops are used.

3.2.1 Detector irradiation

The radiation damage of silicon detectors was discussed in section 2.5.2. It is estimated that detectors in the SCT will receive a radiation fluence of 1.4×10^{14} 1 MeV n cm^{-2} during the first 10 years of operation [30]. The six detectors of this study were irradiated for 300 hours using 24 GeV protons from the CERN PS accelerator. The total fluence received by each detector was measured using aluminium foil activation to be 3×10^{14} protons cm^{-2}. This fluence is approximately equivalent to 2×10^{14} 1 MeV n cm^{-2}, the estimated total SCT fluence plus a 50% safety margin. To minimise detector noise and the risk of detector thermal runaway, the SCT will be operated at a temperature of -7^oC [30]. To replicate the SCT environment as closely as possible, the detectors in this study were uniformly irradiated in a dry nitrogen atmosphere at a temperature of -8 ± 1^oC [57]. A reverse bias of 150 V was applied to all detectors and the read-out strips were connected to ground.

3.2.2 Detector annealing

The LHC will operate for approximately a third of each of the 10 years of running and the Inner Detector will therefore be subject to an annual cycle of irradiation. The temperature of the SCT will be maintained at -7^oC at all times expect during maintenance when the temperature will rise to around room temperature. In [30], it is estimated that the SCT will be at 20^oC for 2 days and 17^oC for a further 14 days annually.

In this study, the effect of the annual warm-up was simulated by keeping the detectors at 21^oC for 25 days. This period of time and temperature were estimated, using the Ziock parameterisation [47], to yield the same effective dopant concentration annealing as the 10 years of annual warm-up periods. More details of the annealing can be found in [57].

Detector	Depletion voltage after 9.3 days (V)
P1	370
P2	145
P3	257
N1	305
N3	245

Table 3.2: The full depletion voltages after 9.3 days of annealing at 25°C for five of the studied detectors [57]. The depletion voltages were determined from CV measurements at 100 Hz and -10°C.

The depletion voltages of the detectors were measured after 9.3 days of annealing using a capacitance-voltage (CV) measurement at 100 Hz and -10°C (table 3.2). Data at later times are not available for the detectors studied. It should be noted that the depletion voltage found using CV measurements has been found to be frequency dependent [57,58]. The CV measured depletion voltage has also been shown to be as much as 100 V lower than the lowest voltage at which full charge collection is observed [56].

The leakage currents of the six detectors were measured during the test beam to be less than 0.5 mA at a bias voltage of 450 V and a temperature of approximately -8 °C. All detectors therefore fulfil the post-irradiation leakage current specifications (section 2.6).

3.3 The test beam set-up

3.3.1 Detector read-out

Each detector was mounted on a ceramic frame and wire bonded to a pitch adapter also on the frame. The purpose of the pitch adapter, referred to as type D, was to increase the physical separation of read-out channels to facilitate the repeated bonding

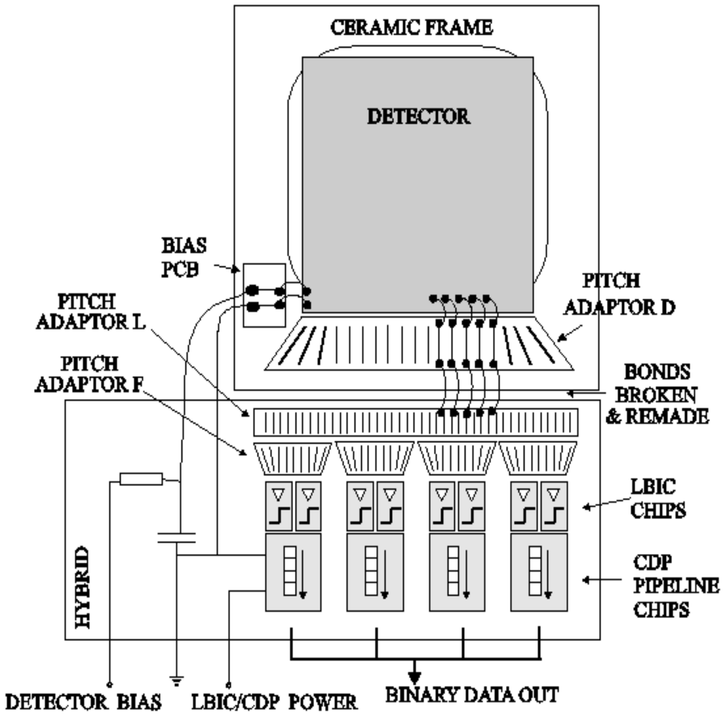

Figure 3.1: A schematic of a detector connected to a binary electronics hybrid (courtesy of K. Wyllie and D. Robinson).

and unbonding of the detector from front-end electronics mounted on a hybrid. For this test beam, binary hybrids populated with LBIC, CDP and HAC chips were used. The detector and hybrid are shown schematically in figure 3.1.

The LBIC chip [59] is an analogue chip performing preamplification, pulse shaping and discrimination. Each chip takes 64 detector read-out strips as its input and, after preamplification and pulse shaping, compares the charge on each with a single definable threshold. The 64 output channels are set high or low to indicate a charge on the corresponding input channel as being above or below the threshold. The threshold of each LBIC can be calibrated using capacitors connected to the input channels of the chip. The capacitance of these calibration capacitors is known to a high precision and, by charging them at a known voltage, a known charge can be injected into the LBIC.

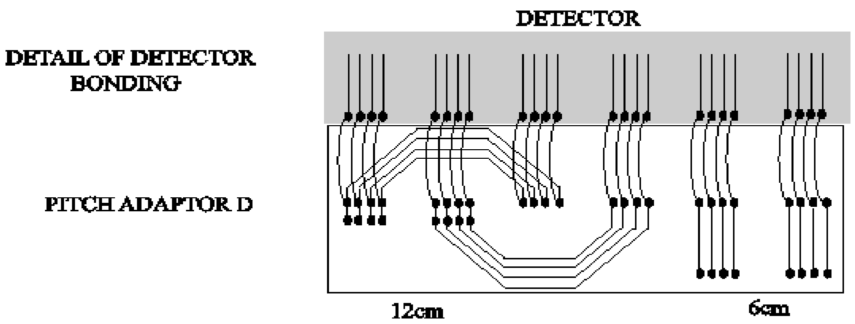

Figure 3.2: A schematic of half of pitch adapter D showing the adjacent 12 cm and 6 cm regions.

The Clock Driven Pipeline (CDP) chip [60] reads the output of two LBIC chips, that is 128 channels. The CDP is clocked at 40 MHz and on each clock edge the 128 bit hitmap on the input channels is placed onto the front of a 128 deep hitmap pipeline. Every 25 ns a new hitmap is added to the pipeline. When the CDP receives a read-out trigger, the hitmap at a predetermined depth in the pipeline is copied into a secondary buffer from where it can be read out.

The Header Adder Chip (HAC) [61] handles communication between the hybrid and off-detector electronics. It controls and organises the read-out of the buffers of up to 6 CDP chips.

The CDP/LBIC combination is not the chosen final solution for the SCT front-end electronics. These were, however, the most satisfactorily working chips available at the time of the test beam.

In the ATLAS SCT, two 64 mm $\times$ 63.6 mm detectors will be placed end-to-end and bonded together to give 768 approximately 12 cm long strips. To test the read-out of 12 cm long strips using just one detector, a pitch adaptor D was used to combine strips (figure 3.2). Each group of 256 output channels of the pitch adaptor is divided into two regions of 128 strips: a "6 cm region" and a "12 cm region". In the 6 cm region, each output channel is connected to just one detector strip. In the 12 cm region, two detector strips are connected to each output channel of the pitch adaptor. The minimum separation of two strips connected to the same output channel is 32 strips, or 2.56 mm. There are 512 output channels on the pitch adaptor used to read out the 768 strips of a detector.

Each detector and hybrid was mounted in an aluminium frame. The combination of a detector and hybrid will be referred to as a binary module.

3.3.2 Experimental set-up

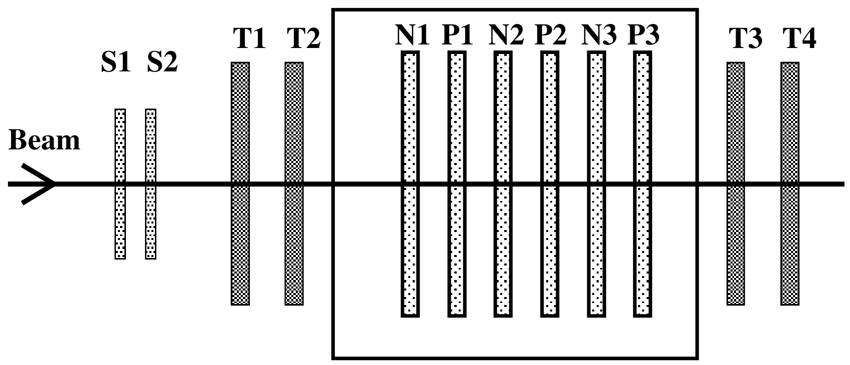

Figure 3.3: A schematic view from above of the test beam set-up. The telescope modules (T1-4) were used in track finding and projection. The scintillators (S1-2) were used to provide a trigger for the binary modules (P1-3, N1-3).

The November 1997 apparatus is shown schematically in figure 3.3. Figure 3.4 shows a photograph of the set-up. The apparatus was installed in the CERN SPS H8 beam line. The beam was composed of 180 GeV/c pions and had an approximate beam spot size of 15×15 mm^2. Particles were delivered in bursts every 14.4 seconds.

The six binary modules were placed with strips perpendicular to the beam and oriented vertically. The beam pions were normally incident on the detectors. The modules were operated in a light tight, thermally insulated box in a dry nitrogen atmosphere at a temperature of -8^oC. To allow the testing of both 6 cm and 12 cm strip read-out, the beam was centred on the junction of a 6 cm and 12 cm region.

Four telescope modules (T1-4) were placed in the beam with two either side of the box housing the binary modules. Each module comprised two silicon detectors of 50 μm pitch oriented with strips at right angles to one another. Each module thus gave two orthogonal space points. They were read out with slow analogue electronics (VIKING chips [62]). The telescope modules were used in the data analysis to reconstruct beam particle trajectories. The precision with which trajectories can be projected to the binary modules has been measured in previous test beams to be around 2 μm [63].

Two scintillators (S1, S2) were placed before the whole assembly. A coincidence signal from S1 and S2 provided a trigger to initiate read-out of the binary and telescope modules. Typically, 100 triggers were received in each burst.

3.3.3 Off-detector electronics and data acquisition

Signals from the scintillators, binary modules and telescopes were relayed to a counting room using 30 m long cables. One digital signal processor (DSP) was used to control and read out each binary module. The DSP performed a limited amount of processing on the data received from the on-detector HAC chip. A pulse generator supplied the 40 MHz clock to the binary modules. Analogue to digital converting modules known as IRAMs were used to process the data from the telescope modules. The IRAMs performed some

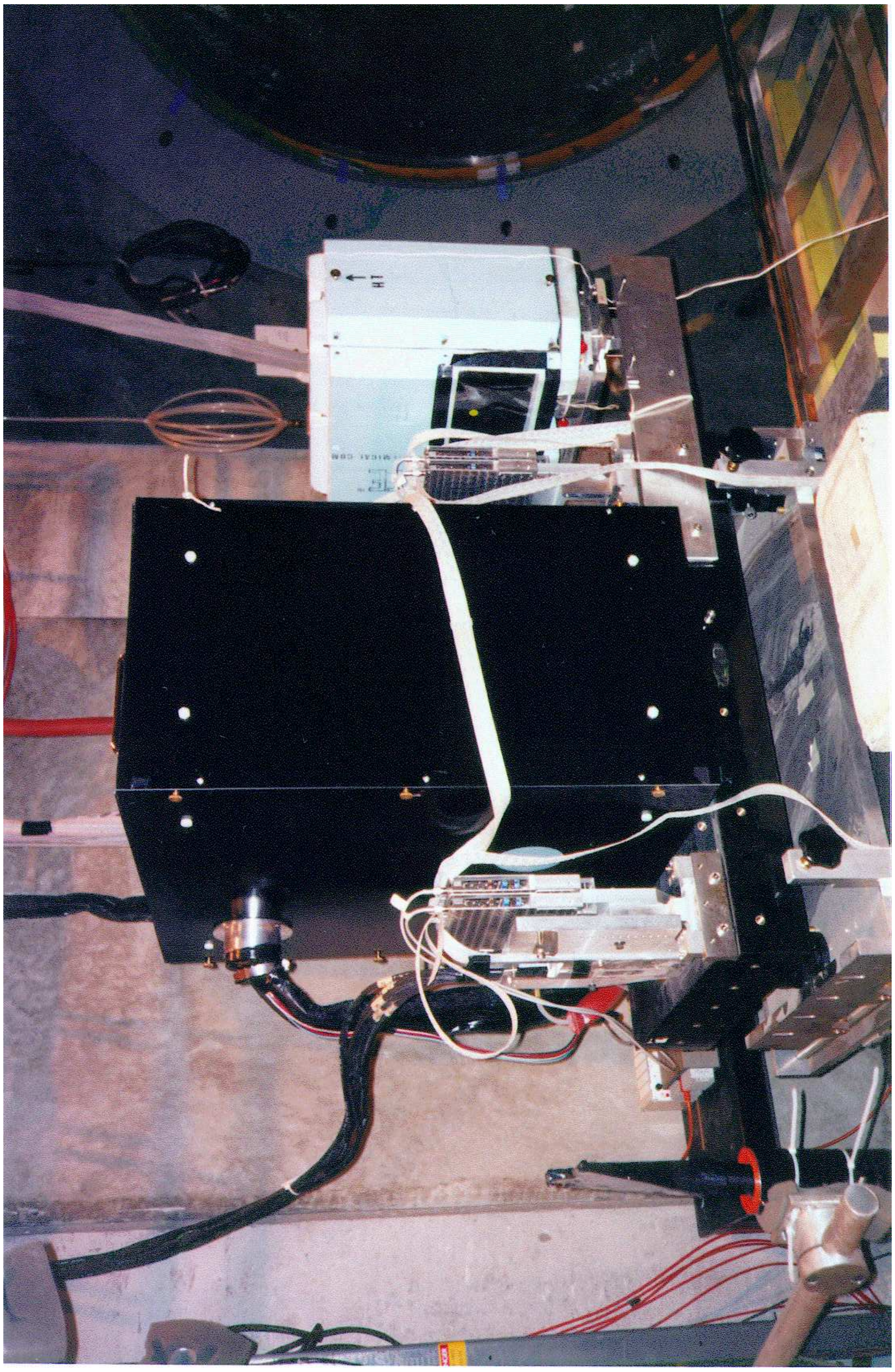

Figure 3.4: A photograph of the November 1997 test beam apparatus. The large black box in the centre of the picture housed the 6 modules investigated in this chapter. The telescope modules can be seen immediately before and after the module box. Beam pions traversed the photograph from left to right. Part of the supporting structure for the trigger scintillators can be seen in the very bottom left of the photograph. The two pairs of telescope modules are separated by approximately 70 cm.

data compression, converting a list of the charge on each strip to a list of clusters of hit strips.

In the LHC, both the beam crossing frequency and the detector read-out clock frequency will be 40 MHz. The phase between these two clocks will be chosen to maximise charge collection in the silicon detectors and will be fixed. In the H8 test beam, the scintillator coincidence trigger can occur at any time within the 25 ns gap between read-out clock edges. The efficiency of charge collection can depend on the time between the trigger and subsequent read-out clock. A time to digital converter (TDC) with 200 ps precision was used to measure this time.

The processed DSP, IRAM and TDC data were combined using a RAID processor installed in the same VME crate as the data processing modules. The raw data were encapsulated into a modular and hierarchical "RD13" data structure [64] and saved to disk. Typically, data files of 25000 events were produced which were then written to magnetic tape.

3.3.4 Raw data processing

Before the final analysis of the data, a Data Summary Tape (DST) was produced. The DST contains a list of clusters of hit strips in the telescope and binary modules and TDC information. A list of straight line tracks, fitted through hits in at least two of the four telescope modules, was also included in the DST. Ideally, hits from at least three modules would be used to find tracks. In this test beam, however, a chip used to read out a region of one of the telescope modules was not working. Requiring three or more pairs of space points would have reduced the number of usable events in each run.

Before tracks could be reconstructed, an alignment file, which records the position and orientation of each detector, had to be produced. Each time the apparatus was moved, an alignment file was produced from a DST filled with just detector cluster coordinates. The orientation and position of a detector as recorded in an alignment file is referred to as the software alignment of the detector.

3.3.5 Software alignment of detectors

The software alignment of each detector was calculated from tracks found using the outer two telescope modules (T1,T4), the distance between which had been measured by hand. These two anchor planes were assumed to be perpendicular to the beam. The other detectors were aligned in software by minimising the RMS width of the track residual distribution. The track residual is the distance between the track intersect with the detector and the centre of the detector strip registering a hit. This distance is measured along a line in the detector plane perpendicular to the strips. The distribution width was minimised by varying the detector's software orientation in five ways: rotating the detector around its vertical and horizontal axes; rotating the detector in its plane around an axis parallel to the beam; translating the detector in a direction perpendicular to the beam and to the strip orientation; and translating the detector parallel to the beam.

3.4 Offline data analysis

The binary modules were aligned such that the beam was centred on a junction between a 6 cm and a 12 cm region. The two regions were analysed separately. In the 12 cm region, two detector strips are connected to each LBIC input channel. If an output channel in a 12 cm region records a hit, it is not possible to determine which of the two strips fired using the binary module information alone. In this analysis, it is assumed that the strip nearest to the particle trajectory, determined using the telescope modules, was hit.

3.4.1 Bad channel identification

A single list of bad channels in each binary module was used in the analysis of all runs. The bad channels were identified using data from 20 runs representative, in terms of voltage and threshold, of the whole data sample. The finding of bad channels in an individual run is described below. Channels identified as bad in more than five runs were listed as bad channels for the purposes of the final analysis of the module.

In the bad-channel analysis of individual runs, each binary module is analysed separately. For each run, all hits in the module are histogrammed by channel number. This histogram indicates the number of times in the run that each read-out channel recorded a hit. A bad channel is either dead or noisy. A noisy channel is defined as having four times as many hits as the average number of hits on its two neighbouring channels. Similarly, a dead channel has four times fewer hits than its neighbours. This simple algorithm fails to identify clusters of noisy channels which occasionally occur and must therefore be removed by hand. Typically, two or three strips out of 128 were identified as being bad.

3.4.2 Definitions of efficiency and noise occupancy

For a given binary module, an event is said to be efficient if there is a hit strip, not identified as bad, within ± 160 μm of the particle trajectory intersect as calculated using the telescope modules. Although most track residuals will be shown to have an absolute value of less than 60 μm (section 3.5.6), a window of ± 160 μm was used to allow for small errors in detector alignment. The efficiency of a detector is the fraction of good events in which the detector is efficient. A good event is defined in section 3.4.3.

A noise hit is defined as any above threshold read-out channel which has not been identified as bad and which is outside of ± 200 μm of the track intersect. The noise occupancy of an event is the number of noise hits as a fraction of the number of good read-out channels. The noise occupancy of a run is the mean noise occupancy in all good events.

3.4.3 Event selection

In the analysis of a binary module, the tracks reconstructed from the telescopes are essential for determining whether a particle passed through the region of the detector being studied and for finding noise occupancy and efficiency. To eliminate any ambiguity over which track to associate with which hits, only events with exactly one reconstructed track were used. An event was not used if the track traversed the module under test within ± 160 μm of a bad channel or the edge of the detector region being studied.

TDC cuts

In previous beam tests [49, 65] the efficiency of a module has been observed to vary with the time between the scintillator trigger and the clock edge on which the binary modules are read out (the TDC time). The effect is largest when LBIC chips are used to read out n-in-n detectors. LBICs were designed to be used with p-in-n detectors, in which the charge collection differs from n-in-n detectors because of different mobilities of holes and electrons. The overall effect is that the output pulse of an LBIC reading an n-in-n detector is shorter than when reading a p-in-n detector. If a particle passes through an n-in-n detector just after a binary clock pulse, the LBIC output is not read by the CDP until nearly 25 ns later. The LBIC-shaped pulse peaks in less than 25 ns and the charge at the LBIC discriminator input may have fallen below the binary threshold. If a particle traverses the detector just before the binary clock, the output of the LBIC

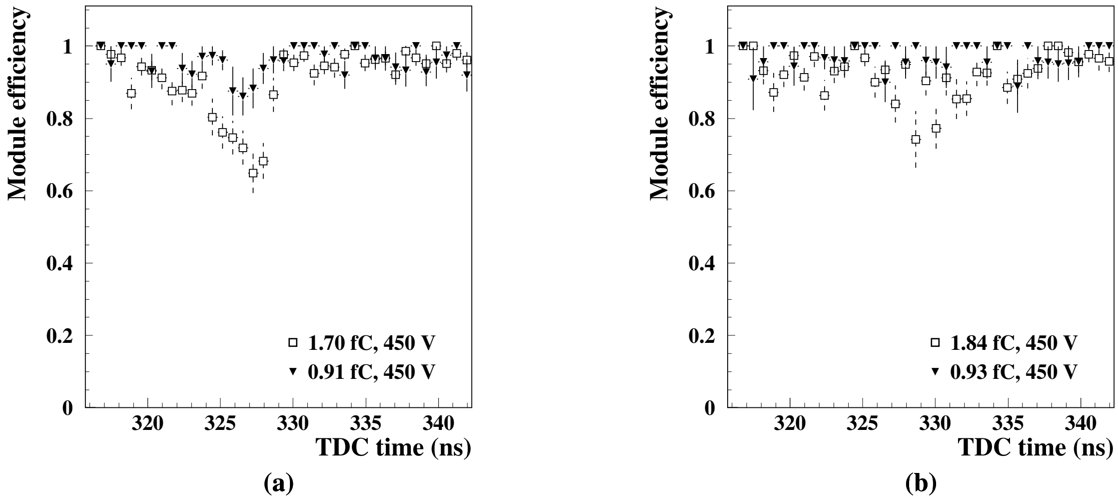

Figure 3.5: Module efficiency plotted against TDC time for (a) module N3 and (b) module P3

pulse shaper may not have risen above the binary threshold. Inefficiencies can therefore occur at extrema in the TDC time. Such inefficiencies are also seen in p-in-n detectors when using a high binary threshold.

Figure 3.5a shows the efficiency of module N3 plotted against the time between the scintillator coincidence trigger and the binary read-out clock pulse. The efficiency is seen to be lower for certain values of the TDC time and to be discontinuous at 328 ns. This observed pattern is due to the polarity on a TTL/NIM converter being incorrectly set. The converter takes the scintillator signal as input and its output triggers the binary module read-out. With the polarity incorrect, the binary modules are triggered on the back edge of the pulse from the TTL/NIM converter instead of on the front edge. The TTL/NIM converter output pulse is about 10 ns long. If the coincidence trigger is received just after a binary read-out clock pulse, the binary modules are read out on the following clock pulse. In this case, the TDC time is nearer 340 ns, where the modules are efficient. If, however, the coincidence trigger is received less than 10 ns before the next binary clock pulse, the binary modules are not read out until over 25 ns later and some inefficiency is introduced. In this case, the TDC time is within the first 10 ns of the range of the TDC times.

The read-out of module P3 is less affected by the trigger problem. The dip in efficiency seen in figure 3.5b for a binary threshold of 1.84 fC is symmetric around 328 ns. A similar variation of efficiency with TDC time would be observed in the n-in-n and p-in-n detectors at high thresholds even if the binary modules were correctly triggered. If the TTL/NIM converter polarity had been correctly set, the modules would have been less efficient for low and high TDC times.

In this analysis, events with the TDC time in the following ranges were not used:

- n-in-n detectors: 319 ns $< t_{TDC} <$ 331 ns
- p-in-n detectors: 325 ns $< t_{TDC} <$ 335 ns

3.4.4 The data sample

Runs were taken with the binary modules biased at voltages between 100 V and 500 V and with a binary threshold between approximately 0.6 fC and 5.0 fC. In ATLAS, it is intended that the binary threshold will be set to 1.0 fC. Data for the detectors N1 and N3 are only available for the first and last halves of the data taking period respectively. In all runs, the beam pions are approximately normally incident on the detectors.

3.5 Results

3.5.1 Module efficiency and detector bias voltage

Figures 3.6a-3.6c show the variation of module efficiency with detector bias voltage for the 6 cm region of the three n-in-n detectors. Efficiencies are shown for binary thresholds of around 1.0 fC. For a given bias voltage, the efficiency of each module at 1.0 fC has been found from the plotted points using a linear interpolation. The 1 fC-efficiencies are shown in figures 3.6a-3.6c as a line and are summarised for all three detectors in figure 3.6d.

The behaviour of the three n-in-n modules is seen to be similar. The efficiency is constant above approximately 150 V in all three modules. The detector bias voltage above which the module efficiency is constant will be referred to as the plateau voltage. Plateau 1.0 fC-efficiencies of 95% are observed, except for module N2 which has a lower plateau value of 90%. At a bias of 100 V, the module efficiency is about 90% of the plateau efficiency.

The full depletion voltages of the three n-in-n detectors were found, using CV measurements, to be of the order of 280 V after the first 9 days of the annealing period (table 3.2). The depletion voltages were not re-measured before the detectors were placed in the test beam. CV measurements were, however, performed on similar detectors for the full 21 days. The depletion voltages of these detectors rose by between 50 V and 80 V in the last 16 days of annealing [57]. Using this information, the depletion voltages of the n-in-n detectors are estimated to be in the range 330-360 V. The n-in-n detectors, therefore, demonstrated maximally efficient operation at approximately half the full depletion voltage. This is expected because after type inversion of the bulk silicon the depletion region of an n-in-n detector grows from the strip side. For a fully

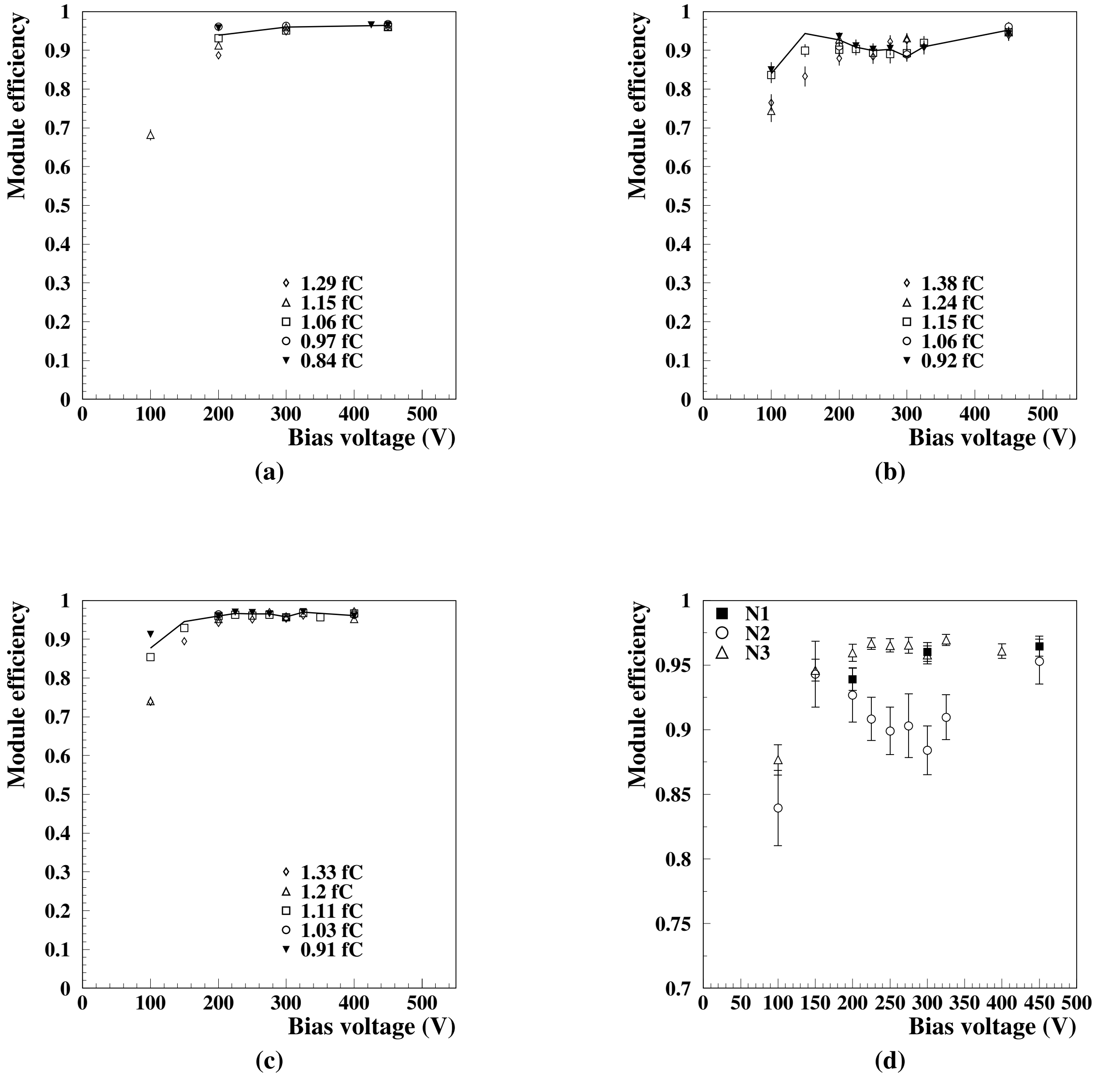

Figure 3.6: The variation with detector bias voltage of module efficiency for several thresholds. Results are shown for the 6 cm region of the modules **(a)** N1 **(b)** N2 and **(c)** N3. In each plot, the 1 fC-efficiency, interpolated from the points shown, is indicated by a line. The 1 fC-efficiencies of the three detectors are shown together in **(d)**.

depleted detector operated with a low binary threshold, an efficiency close to 100% is expected. The lower than expected plateau efficiencies are discussed in section 3.5.2.

Figures 3.7a-3.7c show the variation of module efficiency with detector bias voltage for the 6 cm region of the p-in-n modules. As in figure 3.6, the 1.0 fC-efficiency at a given bias voltage has been interpolated from points at several different thresholds. The variation with bias voltage of the 1.0 fC-efficiency is summarised for all three detectors in figure 3.7d.

The plateau voltages of the three modules are significantly different. When measured during annealing, module P2 was found to have a lower CV determined depletion voltage than modules P1 and P3. Evidence of a lower depletion voltage is also seen in these test beam measurements: P2 is fully efficient above 160 V whereas P1 and P3 reach full efficiency at 410 V and 260 V respectively. The low depletion voltage of P2 is not understood. A large spread in depletion voltages has previously been observed in different irradiated diodes [66].

The difference in behaviour of modules P1 and P3 can be explained in terms of differing detector thicknesses. The depletion voltage scales as the square of detector thickness. Scaling the bias voltages to 300 μm, modules P1 and P3 are found to be fully efficient above 319 V and 298 V respectively.

In contrast to the n-in-n modules, the efficiency of the p-in-n modules falls sharply at bias voltages below the plateau voltage. At 50 V below the plateau voltage, the p-in-n module efficiency has fallen by approximately 50% compared to 10% in the n-in-n modules. In irradiated p-in-n detectors, the depletion region grows from the back plane of a detector. When a p-in-n detector is under-depleted the strips are not in the depletion region. A reduced signal is, however, produced in the strips by induction across the high resistivity, undepleted bulk.

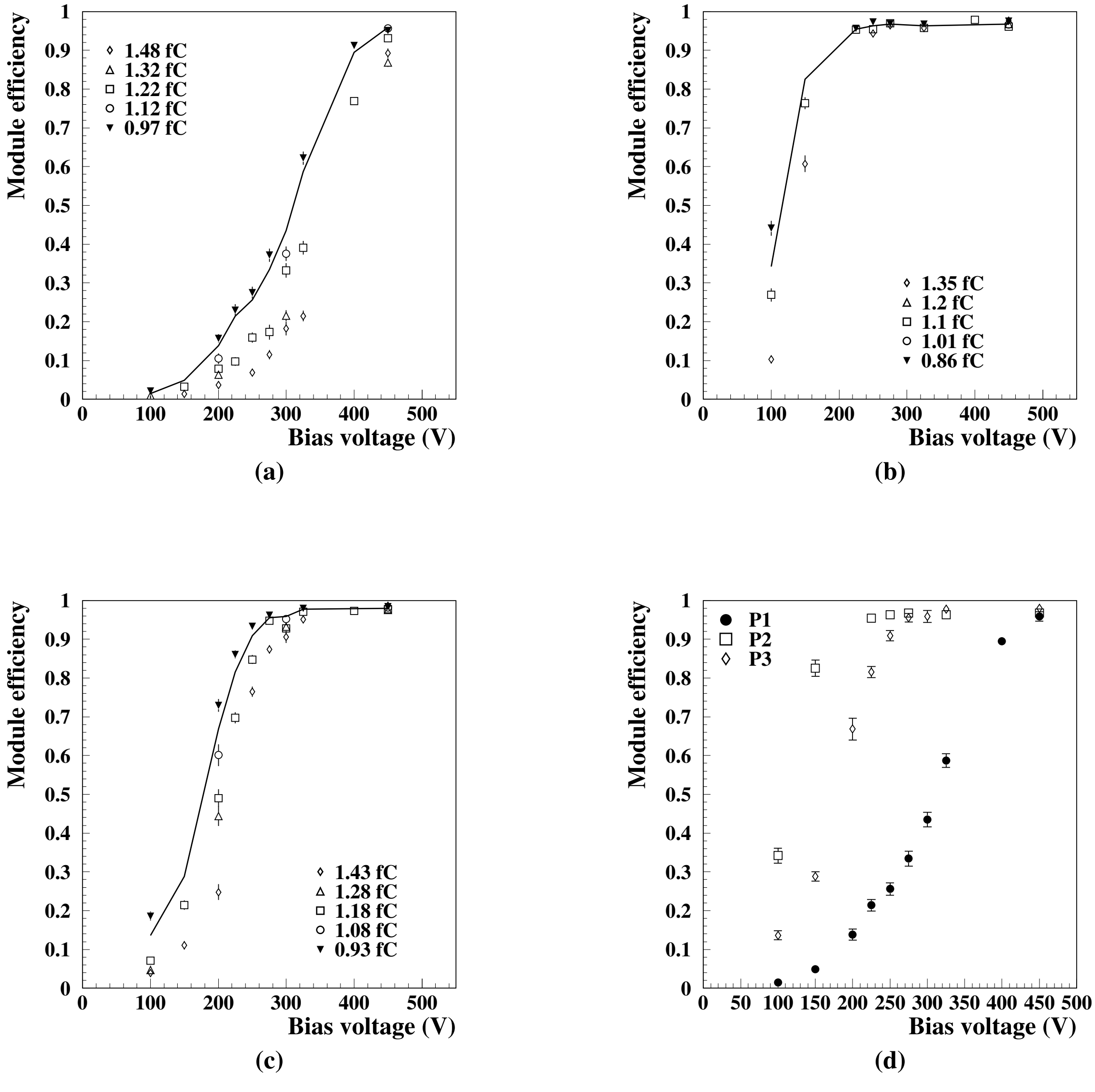

Figure 3.7: The variation with detector bias voltage of module efficiency for several thresholds. Results are shown for the 6 cm region of the modules **(a)** P1 **(b)** P2 and **(c)** P3. In each plot, the 1 fC-efficiency, interpolated from the points shown, is indicated by a line. The 1 fC-efficiencies of the three detectors are shown together in **(d)**.

The depletion voltage of the detector P2 was measured after the test beam to be 150 V. Using fast analogue electronics [67] and a radioactive source, the charge collection efficiency was found to saturate at a bias voltage of 300 V [56]. In this test beam, therefore, module P2 is found to be fully efficient at a detector bias just above the CV determined depletion voltage.

The 1 fC-efficiencies of the 12 cm regions of the n-in-n and p-in-n modules are shown in figures 3.8a and 3.8b. The variation with bias voltage is seen to be similar in the 6 cm and 12 cm regions. The data from both regions of the detectors are summarised in table 3.3.

3.5.2 Plateau efficiencies

In the plots of section 3.5.1, the modules displayed maximum efficiencies with respect to bias voltage and binary threshold of between 90% and 96%. The plateau efficiency of a module is expected to be closer to 100%. It was found that the maximum efficiency of modules could be raised by approximately 2% by requiring that at least two modules, not including the module under test, were efficient in a good event. This suggests that some of the module inefficiency is introduced during detector read-out and data acquisition (DAQ). Since neither the DAQ system or FEE used in this test beam are the chosen solution for ATLAS, such inefficiency is of less interest than inefficiencies at the detector level. No requirement on the efficiency of other detectors has been imposed to obtain the results presented in this chapter. The p-in-n detectors are not fully efficient in lower bias voltage runs and only one n-in-n detector was functioning correctly for the entirety of the test beam. Requiring at least two other detectors to be efficient would have significantly reduced the available statistics.

Using binary modules as anchor planes removes some but not all inefficiency. No

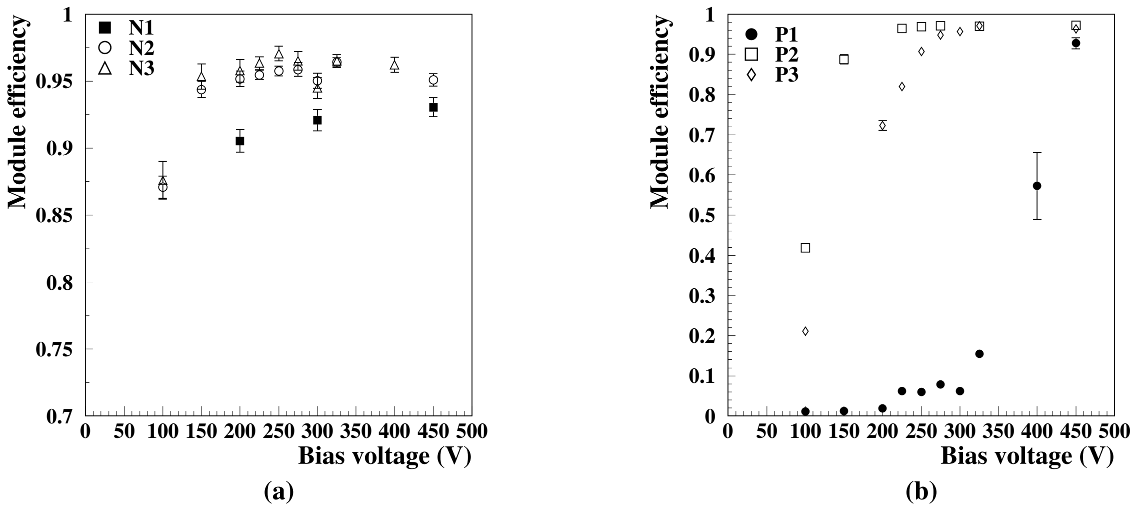

Figure 3.8: The variation of module 1.0 fC-efficiency with bias voltage for the 12 cm region of (**a**) the n-in-n detectors and (**b**) the p-in-n detectors.

Module	Thickness (μm)	Plateau voltage (V)			
		Measured		Scaled to 300μm	
		6 cm	12 cm	6 cm	12 cm
N1	300	-	-	-	-
N2	300	140	140	140	140
N3	300	120	140	120	140
P1	340	410	450	319	329
P2	300	160	160	160	160
P3	280	260	260	298	298

Table 3.3: Summary of the lowest detector bias voltage at which fully efficient operation is observed for all six modules. The two right-most columns show the bias voltages scaled to those of a 300 μm thick detector. It is difficult to determine the plateau voltage of N1 because little data is available for bias voltages below 200 V.

correlation was found between module efficiency and the following:

- Position of the beam in both the vertical and horizontal planes
- Position of the event in the burst
- Detector strips though which the particle passed. The inefficiency is therefore not due to unidentified dead strips.

In the 1998 beam test, the hitmaps in some events were found to be shifted by eight bits in a small fraction of events. No evidence of such a shift was seen in the November 97 data.

It has not been fully explained why the module efficiencies are not closer to 100%. Evidence that this inefficiency is not due to the detectors themselves but due to the detector read-out is presented in section 3.5.3. Module P2 was also demonstrated to operate at nearly 100% efficiency in the 1998 test beam (chapter 4). In this analysis it is, therefore, useful to compare module efficiencies with those observed for the same module at high bias voltage and low threshold.

3.5.3 Module efficiency and track η

The telescope modules were used to reconstruct pion tracks and to find the point of intersection of the track with the binary detectors. For each module and event, the distance between this intersection point and the centre of the strip to the left of it was measured along a line in the plane of the detector and perpendicular to the strip direction. This distance, expressed as the fraction of the strip pitch (80 μm), is referred to as the track η. A track passing exactly in-between two strips has $\eta = 0.5$. A track passing through the centre of a strip has either $\eta = 0.0$ or $\eta = 1.0$.

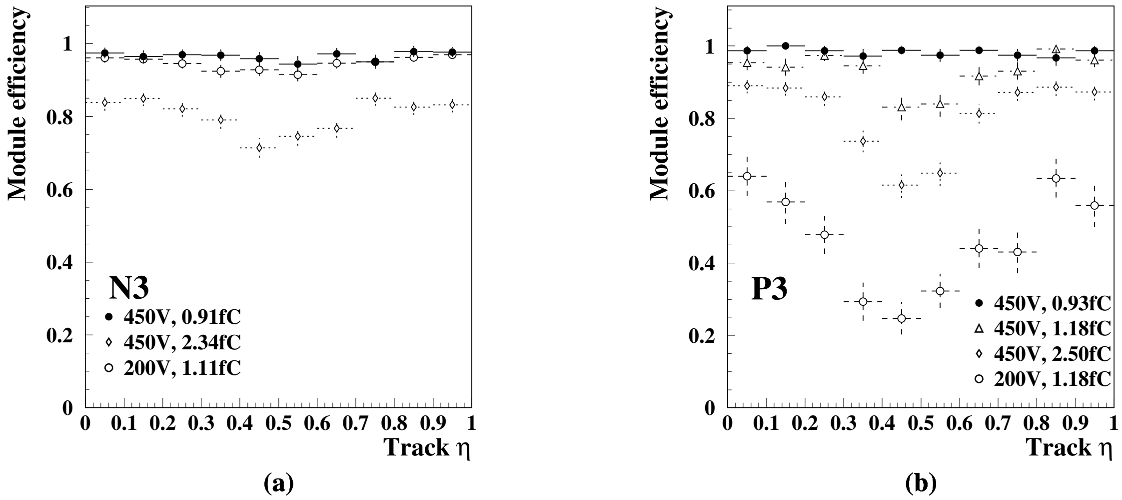

Figure 3.9: The variation of module efficiency with track η for (a) module N3 and (b) module P3 at various thresholds and bias voltages.

Figures 3.9a and 3.9b show the variation of module efficiency with the track η for the modules N3 and P3. At high bias voltage and low threshold, the efficiency of both modules is seen to be uniform with η. When the binary threshold is increased the module first becomes inefficient at $\eta \sim 0.5$ where charge sharing between strips is maximal. At higher binary thresholds, inefficiency is seen at all η. The efficiency at $\eta = 0.0$ and $\eta = 1.0$ is also reduced when a module is operated under-depleted. This is because the active volume of the detector, and hence the produced charge, is reduced.

In the previous section, a plateau efficiency of around 95% was found in all modules. In both modules N3 and P3, the small module inefficiency at 450 V and ~ 1.0 fC is seen to be distributed across all η and not concentrated around $\eta = 0.5$. This suggests that the inefficiency is introduced in module read-out rather than being an intrinsic inefficiency due to the detector design.

3.5.4 Module efficiency and binary threshold

Figure 3.10 shows the variation of detector efficiency with binary threshold for the 6 cm and 12 cm regions of the detectors. The bias voltage of each detector was chosen such that the module was fully efficient at 1.0 fC. The plots can be interpreted as showing the fraction of events in which the charge collected on one strip exceeds a given threshold. They therefore show $I(t) = \int_t^\infty \phi(q)dq$ where $\phi(q)$ is the probability distribution of collected charge, q, and t is a binary threshold. The ionisation energy of silicon is 3.6 eV. A charge of 1.0 fC corresponds to 6250 electrons and an incident particle losing an energy of 22.5 keV.

The median pulse height is the binary threshold at a module efficiency of 50%. The median pulse height of modules N2 and N3 is approximately 4.3 fC. Although no data for module N1 is available above 2.5 fC, it is clear that the median pulse height is lower than in modules N2 and N3. In the 6 cm region, the modules P1, P2 and P3 have median pulse heights of 2.2 fC, 3.6 fC and 3.3 fC respectively.

The Bethe-Bloch equation gives the mean rate of energy loss with distance of a particle in matter. The mean energy loss of a MIP traversing 300 μm of silicon is predicted to be 116 keV. A 180 GeV/c pion loses a mean energy of 170 keV (see figure 2.4). For a thin section of material traversed by relativistic particles, the variation of energy loss around the mean is given by the Landau distribution.

The function $I(t) = \int_t^\infty \phi_L(q)dq$, where ϕ_L is the Landau distribution for 180 GeV/c pions in 300 μm silicon, has been superimposed on figures 3.10a-3.10d. The Landau curves for charge collection efficiencies (CCE) of 50% to 90% have also been plotted. The median pulse height predicted by the integrated Landau for 100% CCE is 6.5 fC.

Figure 3.11a shows the median pulse height of each detector expressed as a fraction

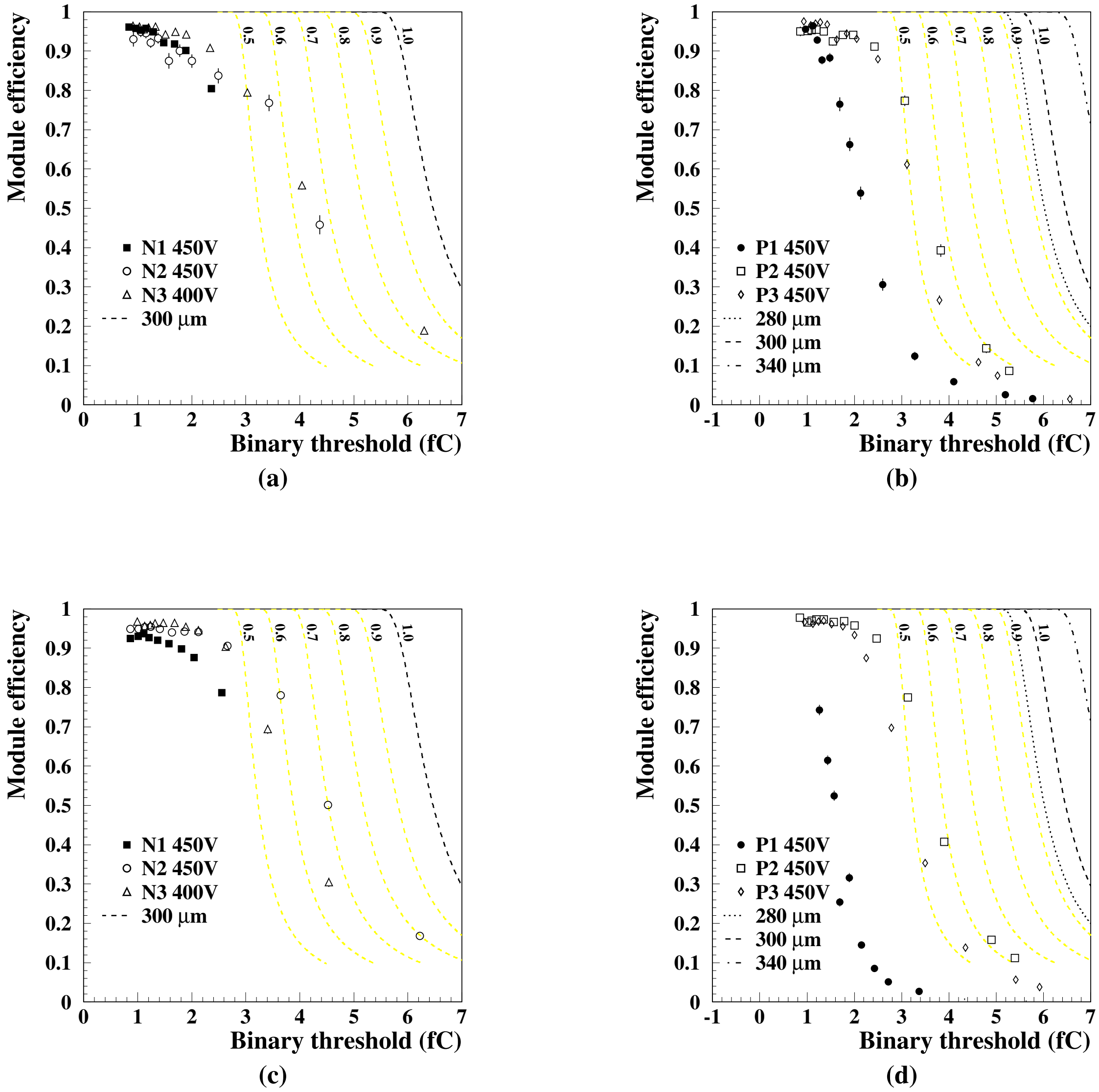

Figure 3.10: Module efficiency plotted against binary threshold for **(a)** The 6 cm region of the n-in-n detectors; **(b)** The 6 cm region of the p-in-n detectors; **(c)** The 12 cm region of the n-in-n detectors; **(d)** The 12 cm region of the p-in-n detectors. On each figure, the integrated Landau distribution for a 300 μm detector has been plotted for charge collection efficiencies between 50% and 100%. In **(b)** and **(d)** The integrated Landau distribution for 100% charge collection efficiency is also plotted for 280 μm and 340 μm thick detectors.

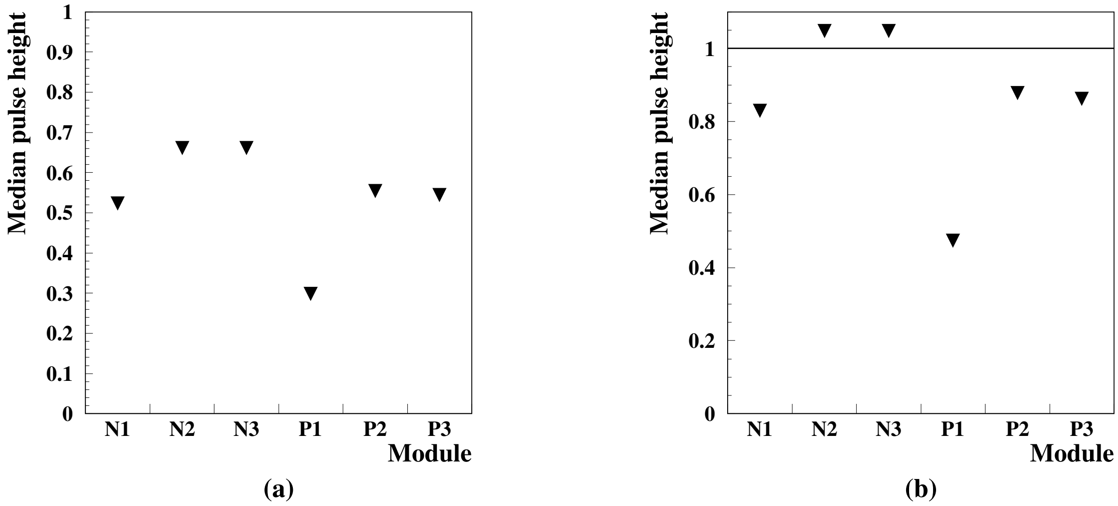

Figure 3.11: The median pulse height of each module expressed as a fraction of: **(a)** the value predicted by the Landau distribution; **(b)** the median pulse height of a Landau scaled to agree with the restricted Bethe-Bloch equation. The differing detector thicknesses have been taken into account in both plots.

of the value predicted by the Landau distribution. The differing detector thicknesses have been taken into account. The observed median pulse heights are seen to be between 35%-50% lower than predicted in the n-in-n modules and 45%-70% lower in the p-in-n modules. The average value of the Landau distribution plotted in figure 3.10 is, however, given by the Bethe-Bloch equation. The restricted Bethe-Bloch equation (section 2.3) more accurately predicts the energy deposited by highly relativistic particles in a thin section of material.

For 180 GeV/c pions ($\gamma\beta = 1285.7$), the Bethe-Bloch and restricted Bethe-Bloch equations predict mean energy losses of 5.67 MeV cm^{-1} and 3.58 MeV cm^{-1} respectively. The restricted Bethe-Bloch equation has a parameter T_{max}, the maximum energy transfer from the incident particle to an electron that then remains in the material. In [40], a value of $T_{max} \sim 500$ keV was found for 1 mm thick silicon and is used here. The dependence of $-dE/dx$ on T_{max} is logarithmic and so only the order of magnitude of this parameter is important. Assuming that the median pulse height of a Landau scales in a similar way to the average energy loss, a median pulse height of 4.1 fC is predicted by the restricted Bethe-Bloch equation for 300 μm thick silicon. Figure 3.11b compares the measured median pulse heights with this prediction. Again, the expected median pulse heights in modules P1 and P3 have been scaled to take into account the different detector thicknesses. The observed median pulse heights of modules N1, P1 and P3 are seen to be $\sim$ 85% of the predicted value. The much lower median pulse height of module P1 may indicate that its charge collection efficiency reaches a plateau value above a bias voltage of 450 V. Modules N2 and N3 have median pulse heights $\sim$ 5% above that predicted. This may be due to the difference in shape between the integrated Landau and the experimental distributions which is discussed below.

In figure 3.10, the shape of the experimental distributions differs from the theoretical curve, especially at low thresholds. It has been observed [68, 69] that the actual distribution of energy deposited in material by relativistic particles is described by a Landau distribution convolved with a Gaussian. The Gaussian distribution has components representing noise and the finite binding energy of electrons in a material. The experimental data points from the p-in-n detectors indicate a charge distribution similar in shape but slightly wider than the Landau distribution. The measured charge distribution of the n-in-n detectors is seen to be much broader than predicted. The noise of the n-in-n and p-in-n modules will be shown in section 3.5.7 to be similar. Higher noise in the n-in-n detectors cannot, therefore, be used to explain the broader charge distribution. The pulse shaping of the LBIC is optimised for use with p-in-n detectors. A component of the broadening may be due to the mismatch between charge collection in n-in-n detectors and the LBIC pulse shaping.

The charge distributions of the p-in-n modules are approximately Landau in shape. The median pulse heights are, however, at least 15% below the values predicted by the restricted Bethe-Bloch equation. Two processes which reduce the charge collected on a detector strip are charge sharing and charge trapping.

In [49], the distribution of charge collected on strips of an unirradiated detector was compared with the Landau distribution. The experimentally measured charge is found to be significantly lower than the Landau prediction. This is attributed to charge sharing between strips, which is not taken into account when plotting the Landau. Even if only the strip closest to a particle track registers a hit, an amount of charge less than the binary threshold may have been collected on neighbouring strips. It has already been demonstrated that charge sharing is responsible for some inefficiency in the modules of this test beam (section 3.5.3). In section 3.5.5, it is shown that there is charge sharing in at least 10% of events.

In irradiated detectors, the charge collected is also reduced by charge trapping in radiation induced defects. Reductions in charge collection efficiency of around 15% have been observed after a fluence of 2×10^{14} 1 MeV n cm^{-2} [43].

In summary, the differences between the theoretical integrated Landau and the experimentally measured threshold scan can be explained in terms of the loss of ionisation electrons from the silicon detectors, charge sharing, charge trapping and pulse shaping.

3.5.5 Cluster widths

Figure 3.12 shows the variation with detector bias voltage of the fraction of efficient clusters with a width of one strip. An efficient cluster is within ± 160 μm of the particle track and is in a good event. In the n-in-n detectors, the fraction decreases from nearly unity at 100 V to between 0.85 and 0.9 at 200 V. Above 200 V, the fraction of clusters with one strip is approximately constant. The data from the p-in-n modules follow

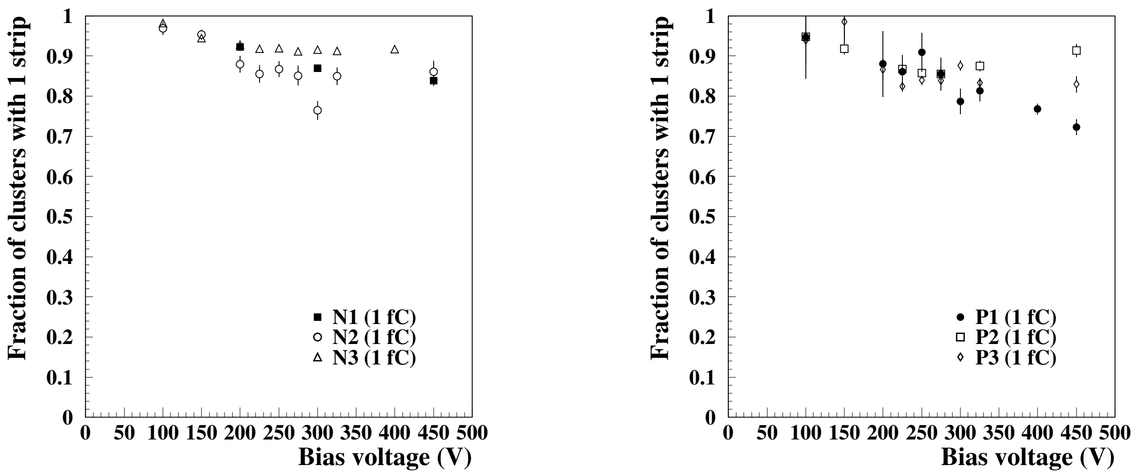

Figure 3.12: The variation with bias voltage of the fraction of single-strip clusters in the 6 cm region of **(a)** the n-in-n modules and **(b)** the p-in-n modules. The fractions are for a binary threshold of 1.0 fC, found by a linear interpolation from the fraction at several different thresholds.

a similar pattern. The fraction in modules P2 and P3 falls from unity to about 0.85 at 200 V and is constant above this voltage. The fraction of single-strip clusters in module P1 does not reach a plateau value between 200 V and 450 V. A similar variation is seen in the 12 cm region of the detectors.

The fall in the fraction of single-strip clusters with increasing bias voltage is due to an increasing fraction of two-strip clusters. Figure 3.13 shows the variation with η of the fractions of one-strip and two-strip clusters. The majority of two-strip clusters are seen to be produced by particles passing close to the inter-strip gap. As the bias voltage of an irradiated n-in-n detector is reduced below the depletion voltage, the width of the depletion region around the strips is reduced and less charge is produced by an incident particle. Charge sharing for particles with $\eta \sim 0.5$ increasingly results in inefficiency, as observed in section 3.5.3, rather than two-strip clusters. As the bias voltage of a p-in-n detector is decreased below the detector depletion voltage, the width of the undepleted

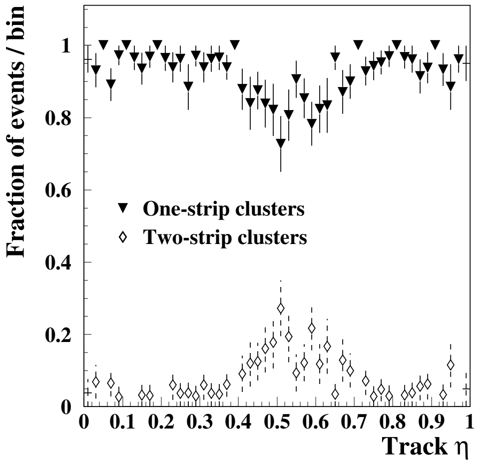

Figure 3.13: The variation with η of the fractions of one and two-strip clusters in module P6 biased at 450 V with a binary threshold of 0.93 fC.

bulk increases and the active volume is reduced. The probability of an incident particle with $\eta \sim 0.5$ inducing a signal on two strips therefore decreases with decreasing bias voltage.

3.5.6 Residual distributions

For a given module, the residual of an efficient event is the distance between the centre of the hit strip and the pion track intersect with the detector. If only single-strip clusters were produced, the residuals would have a top hat distribution of width 80 μm and RMS width 23.1 μm. A typical residual distribution of module N3 is shown in figure 3.14a. A residual distribution of module P3, biased at 450 V and with the binary threshold set to 1.43 fC, is shown in figure 3.14b.

Figure 3.15 shows the variation of the residual distribution RMS with bias voltage.

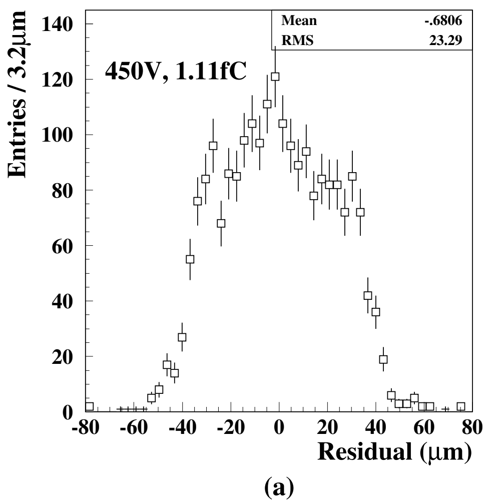

Figure 3.14: Residual distributions for module (**a**) N3 at 450 V and 1.11 fC; and (**b**) P3 at 450 V and 1.43 fC.

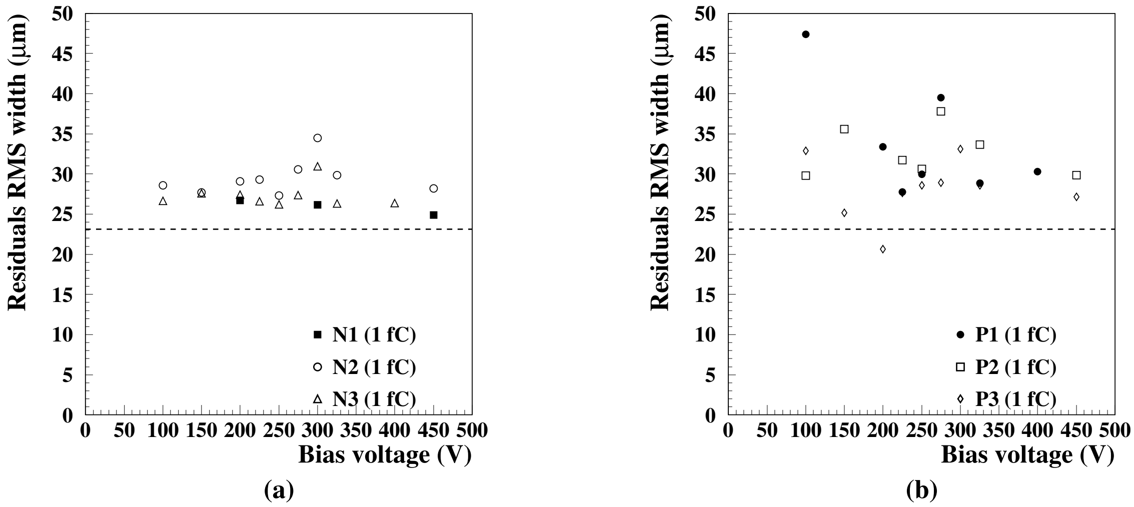

Figure 3.15: The variation with detector bias voltage of RMS widths of the residual distributions for (**a**) the 6 cm region of the n-in-n modules; (**b**) the 6 cm region of the p-in-n modules. The error on each point is of the order of 5 μm. The dashed line drawn on each plot shows the RMS width of an 80 μm wide top-hat distribution.

Data are only shown for the 6 cm regions but are similar in the 12 cm regions. Again, results are interpolated to a threshold of 1.0 fC. The RMS widths of the n-in-n modules are seen to have an approximately constant value of between 25 μm and 28 μm.

The residual distributions in the p-in-n detectors are wider, especially at lower bias voltages. At 450 V, the RMS values are, within errors, equal to those of the n-in-n modules. When p-in-n detectors are operated below full depletion, a signal is produced on the detector strips by induction across the undepleted bulk surrounding the strips. This induction is not as localised as direct charge collection and the residual distribution is, consequently, wider [56].

3.5.7 Noise occupancy

Several caveats should be borne in mind when considering the noise occupancy figures presented in this section. Firstly, the noise occupancy measured in a test beam has components from detector noise, FEE noise and particles in the halo around the beam. The FEE used on the hybrids are not the final ATLAS solution and the FEE contribution to noise cannot be easily identified and removed. The noise occupancy is also sensitive to the definitions of noisy and dead channels and in this test beam only a crude algorithm has been used to remove bad channels. Finally, more rigorous noise results can be obtained from laboratory tests of modules such as in [70].

The noise occupancy, as defined in section 3.4.2, is shown in figures 3.16 for a binary threshold of 1.0 fC in the 6 cm and 12 cm regions of the detectors. The noise occupancy in the 6 cm regions is between 1×10^{-4} and 1×10^{-3} in both types of module. The noise occupancy in the 12 cm regions of the p-in-n detectors is higher, between 5×10^{-4} and 5×10^{-3}. In the 12 cm region of the n-in-n modules, however, the noise occupancies are similar to the values found in the 6 cm region.

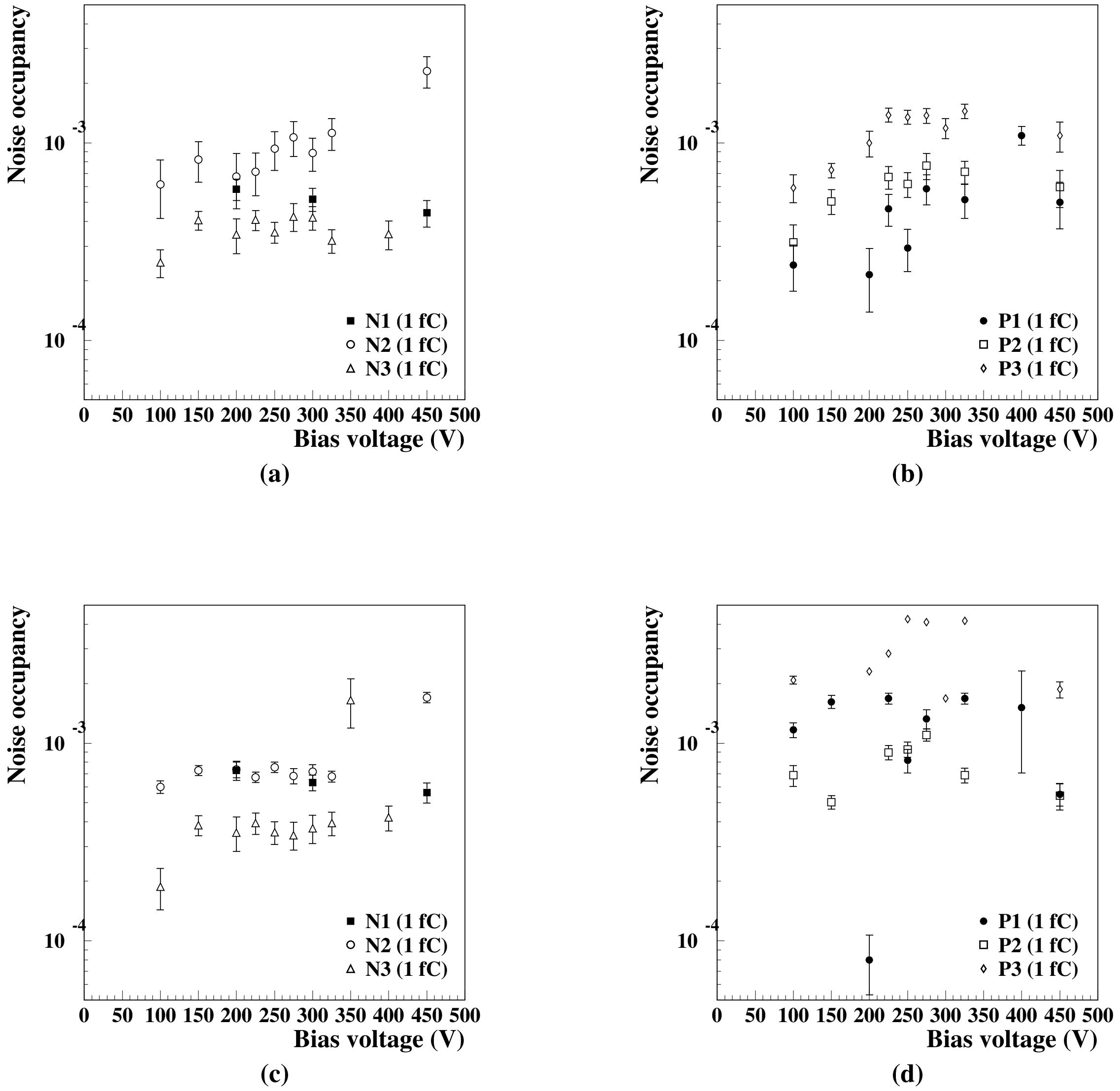

Figure 3.16: The variation with detector bias voltage of the noise occupancy in the **(a)** 6 cm and **(c)** 12 cm regions of the n-in-n modules and the **(b)** 6 cm and **(d)** 12 cm regions of the p-in-n modules. The noise occupancy at 1.0 fC is shown and was found using a linear interpolation between noise occupancies at several thresholds.

The module specifications require a noise occupancy of less than 5×10^{-4}. The 12 cm regions of the p-in-n modules therefore fail this requirement. The FEE used in this test beam are, however, not the chosen solution for ATLAS.

3.6 Conclusions

The performance of three irradiated n-in-n and three irradiated p-in-n detectors has been compared in a test beam. The irradiation and thermal annealing of the detectors were chosen to emulate the radiation fluence and temperatures expected in the first 10 years of LHC operation. The test beam results presented here, therefore, give an indication of the expected performance of two silicon microstrip technologies at the end of the minimum lifetime of ATLAS.

The read-out of 6 cm long and 12 cm long strips has been studied in all six detectors. For a given detector, the module efficiency and precision was found to be similar for both strip lengths.

With increasing bias voltage, p-in-n detectors deplete from the non-strip side whilst n-in-n detectors deplete from the strip side. This is seen most clearly, in the data of this test beam, when module efficiency is plotted against bias voltage. The n-in-n modules were found to operate at full efficiency above a bias voltage of 150 V, which is approximately half the detector depletion voltage. The efficiency of the n-in-n modules falls slowly as the bias voltage is lowered below 150 V. The p-in-n modules were found to reach maximum efficiency above bias voltages between 160 V and 450 V depending on the module. These voltages are greater than or approximately equal to the CV determined depletion voltages which show a similar variation from module to module. For a bias voltage below the plateau voltage, the efficiency of the p-in-n modules falls rapidly. All n-in-n modules and two of the three p-in-n modules operated at maximum efficiency when biased at 300 V, therefore fulfilling the post-irradiation module specifications.

The difference in behaviour of under-depleted p-in-n and n-in-n detectors was also observed to affect module precision. In under-depleted n-in-n modules, charge is still collected directly on detector strips. In under-depleted p-in-n detectors, a signal is produced by induction across the undepleted bulk. Induction is less localised than direct charge collection and results is a wider residual distribution and a degraded precision. At a bias voltage of 450 V, however, both technologies displayed a similar precision of approximately 27 μm.

The distribution of charge collected at a detector strip was investigated by measuring module efficiency at several binary thresholds. The charge collected in n-in-n and p-in-n detectors was found to be approximately 35% and 45% lower respectively than predicted by the Landau distribution. This difference was attributed to the loss of ionisation electrons from the detector, charge sharing, charge trapping and pulse shaping. Evidence for charge sharing in at least 10% of events was observed in a study of cluster widths.

The noise occupancy in the 6 cm regions of both types of module and the 12 cm region of the n-in-n modules was measured to be approximately 5×10^{-4}. A higher noise occupancy of 1.5×10^{-3} was seen in the 12 cm region of the p-in-n modules. This is above the specification value but the FEE used in this test beam are not the chosen solution for ATLAS.

p-in-n detectors have been demonstrated to operate satisfactorily after irradiation and are cheaper to produce than n-in-n detectors. The ATLAS Collaboration, therefore, decided to use p-in-n detectors in the SCT. A more detailed study of module P2 and an unirradiated detector of similar design was undertaken in the summer of 1998. The results of this test beam can be found in chapter 4.

Chapter 4

Test beam studies of p-in-n silicon microstrip detectors

4.1 Introduction and aims

As explained in the previous chapter, a decision was made in early 1998 to use p-in-n detectors in the ATLAS SCT. Microstrip detectors in the SCT will operate in a 2 T magnetic field and charged particles with $p_T > 1$ GeV will pass through the silicon detectors at a maximum absolute angle of 19^o to the detector normal. The principal aim of the August 1998 test beam was to demonstrate that p-in-n detectors can be operated in a magnetic field and with non-normally incident particles.

Two p-in-n detectors were studied; one unirradiated, the second of an identical design but irradiated and annealed according to the TDR 10 year scenario (section 3.2.1). The detectors are described in the next section. The rest of this chapter is divided into three main sections. The first describes the experimental apparatus and data recording. The second section describes the analysis of the data. Results are presented in the final section.

4.2 The detectors

The two p-in-n detectors were of the standard dimensions, 300 μm thick with 768 capacitively coupled read-out strips and polysilicon bias resistors. Both were provided by SINTEF [52]. The irradiated detector was previously tested in the November 1997 test beam and a description of its irradiation and thermal annealing can be found in section 3.2 where it is labelled as detector P2. The depletion voltage of the unirradiated detector was found, using capacitance-voltage (CV) measurements, to be 65 V [71]. The irradiated detector had a CV determined depletion voltage of 150 V [56] and demonstrated full charge collection efficiency above 300 V [56]. In chapter 3, the detector efficiency was found to reach a plateau value at approximately 200 V.

4.2.1 Detector read-out

In this test beam, the hybrids used to read out the detectors were identical in design to those used in the November 97 test beam (section 3.3.1). A D-type pitch adapter was used to connect each detector to the read-out electronics. The hybrids were populated with LBIC, CDP and HAC chips.

4.3 Experimental set-up

The experimental set-up of the test beam is shown in figure 4.1. The apparatus was installed in the CERN SPS H8 beam line. The beam used was composed of 180 GeV/c pions and had an approximate beam spot size of 15 mm$\times$ 15 mm. Particles were delivered in bursts every 14.4 seconds.

The two binary modules were placed with strips oriented vertically in the Uppsala box, a light tight and thermally insulated box (figure 4.2). In figure 4.1, the irradiated detector is labelled as M1 and the unirradiated module is labelled as M2. A flow of dry

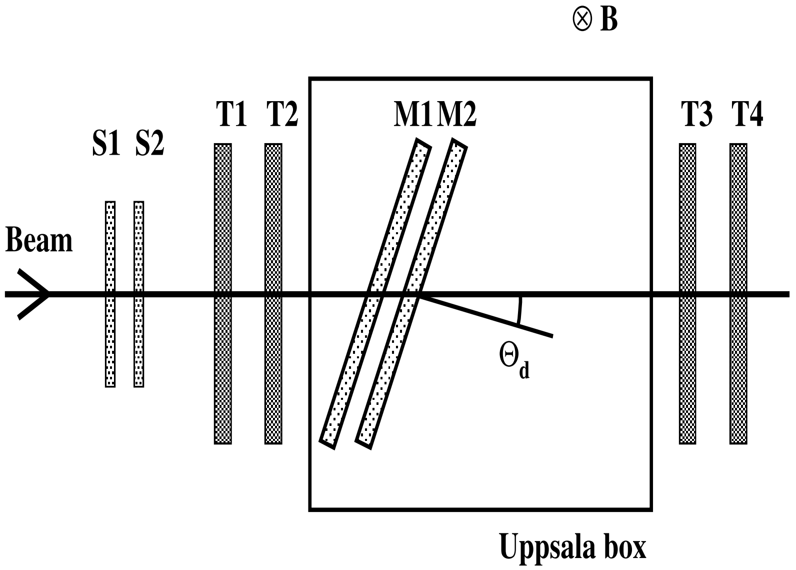

Figure 4.1: A schematic view from above of the H8 test beam set-up. The telescope modules (T1-4) are used in track finding and projection. The scintillators (S1-2) provide a read-out trigger. The binary modules (M1-2) can be rotated around a vertical axis as shown. The Uppsala box is detailed in figure 4.2

.

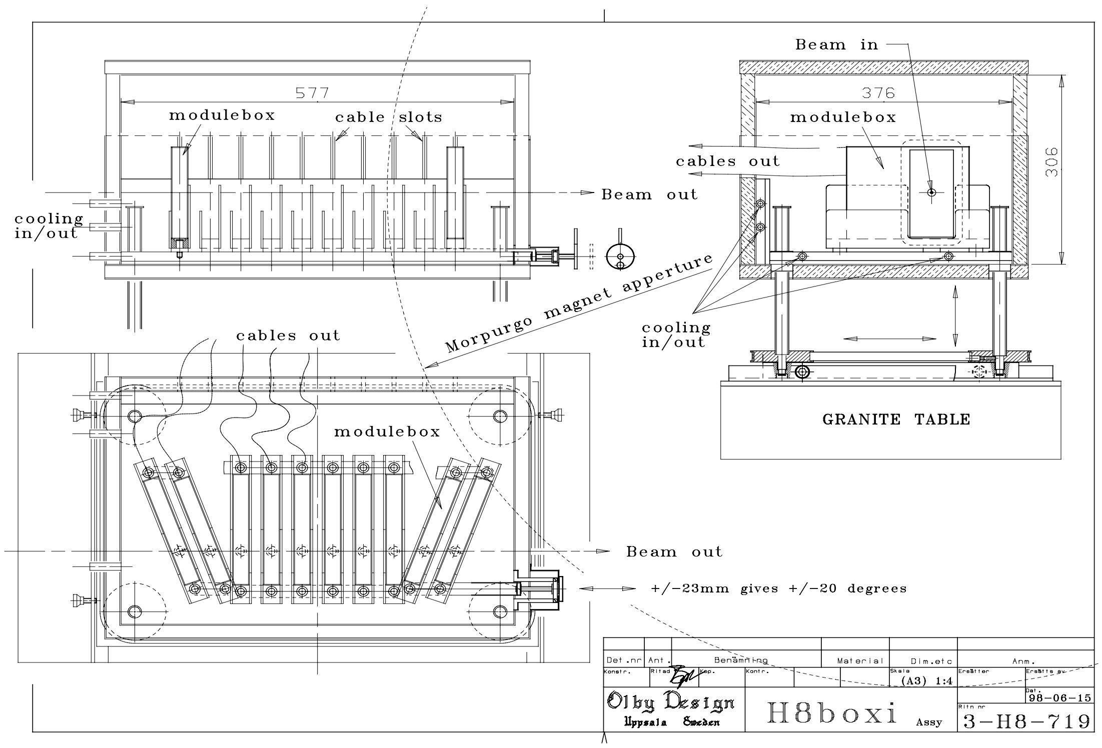

Figure 4.2: The Uppsala box which held binary modules in the test beam. The box is thermally insulated and holds up to 10 modules which can be rotated by ± 20 degrees from perpendicular to the beam (Courtesy of the University of Uppsala, Sweden).

nitrogen was maintained through the inside of the box which was kept at a temperature of -8 ± 1^oC. It was possible to rotate the modules around a vertical axis by $\pm 20^o$ from perpendicular to the beam. This angle of rotation will be referred to as θ_d in the rest of this chapter.

The binary modules were positioned so that the beam passed through the centre of a 6 cm region, that is a region of the detector where only one strip was connected to each LBIC input channel. The satisfactory read-out of 12 cm strips was demonstrated in the November 97 test beam (chapter 3). Also, the main difference between 6 cm and 12 cm strip read-out is increased noise in the 12 cm strips. Since the noise is strongly dependent on the front-end electronics and the CDP/LBIC combination used is not a final solution, the testing of 12 cm strip read-out was not considered to be a useful exercise.

The telescope modules (T1-T4) and scintillators (S1-S2) were the same as those used in the November 97 test beam and are described in section 3.3.2.

The granite table on which the apparatus was installed was on rails and could be slid into the Morpurgo magnet. This is a super-conducting dipole magnet which provides a 1.56 T vertical magnetic field in a cylindrical space 4 m in length and 1.6 m in diameter. The magnetic field is uniform to 10% in the middle 2 m of the cavity [72].

4.3.1 Data acquisition and processing

The off-detector electronics and data acquisition system were very similar to those used in the November 97 test beam (section 3.3.3). As in the previous year, the data were summarised into a Data Summary Tape (DST) before performing the final analysis. In this test beam, tracks were found using at least 3 of the 4 telescope modules.

4.3.2 Detector alignment in a magnetic field

The software alignment of detectors for runs with no magnetic field was described in section 3.3.5. The alignment process for runs with the magnetic field turned on is similar and described below.

The magnetic field was not entirely uniform along the length of the assembly. Determining the magnetic field at several positions and finding the curved particle trajectory through the apparatus would have been a difficult task. Instead, the detectors were aligned assuming straight particle tracks. The track curvature was therefore reflected in the detector positions in the alignment file. Straight lines could then be used to interpolate tracks between detectors. This technique has been used in previous test beams [63].

4.3.3 Determining the angle of binary modules

During this test beam, runs were taken with the binary modules rotated around a vertical axis by between -20^o and +15^o. As shown in figure 4.2, this rotation was achieved by moving a lever arm on the Uppsala box. The arm is attached to the end of the module housings which are free to rotate around axes situated along the beam line. A screw mechanism is used to move the arm and a scale allows the detector angle to be determined. In table 4.1, the angle found mechanically is compared with that found during the software alignment of binary modules. The two angles are seen to agree within two degrees at large angles but not at smaller angles.

To investigate this disagreement at smaller angles, a simple simulation of the test beam was used. An 80 μm pitch detector was simulated at a realistic distance from the origin, from where particle tracks were generated. The spatial distribution around

Angle in Uppsala box (θ_d)	Alignment file angle (θ_a)	
	M1	M2
-20	19.8	20.1
-15	16.8	17.1
-10	12.0	12.5
-5	8.2	9.0
0	6.2	7.1
5	7.2	8.1
10	11.4	12.0
15	17.3	18.2

Table 4.1: A comparison of the angle of the binary modules in the Uppsala box and that found for each module during alignment. Alignment allows only the absolute value of the angle to be found.

the origin and gradient of the tracks were chosen to be similar to the beam parameters observed in the test beam. The detector was simulated as being rotated around a vertical axis by an angle θ_d. This angle and other dimensions of the set-up were used to find the true position in the detector of the simulated track intersect and the local position, x_t, of the nearest strip. It was assumed that only the strip nearest to the track recorded a hit and that no clusters of two or more contiguous strips were produced.

A detector is aligned in software by minimising the RMS width of the track residual distribution. The accuracy of the software alignment therefore depends on the sensitivity of the RMS width to errors in the alignment parameters. To investigate the sensitivity to the detector rotation, an angle, θ_a, not necessarily equal to θ_d, was used to project the track to the detector to find a local position x_a. The track residual was $x_a - x_t$. For each value of θ_a, 10000 tracks were generated to find the width of the residual distribution. Since only single strip clusters are simulated, when $\theta_d = \theta_a$ the residual distribution is a top hat distribution of width 80 μm. The RMS width of such a distribution is $80/\sqrt{12}$ μm which is 23.1 μm.

Figure 4.3 was produced using the simulation and shows the effect on the width

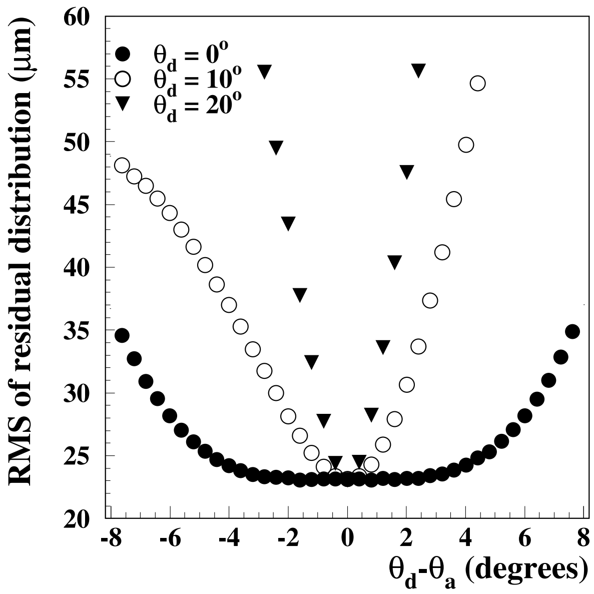

Figure 4.3: The variation with $\theta_d - \theta_a$ of the measured residual distribution RMS. θ_d is the actual detector angle and θ_a is the detector angle used to project tracks to the binary module.

of the track residual distribution of using an incorrect binary detector angle in track projection. The plot shows the sensitivity of the alignment procedure to detector angle. When $\theta_d = 0$ the detector is perpendicular to the beam. If an incorrect angle of 5^o is used in track projection when $\theta_d = 0$, figure 4.3 shows that the residuals RMS width increases by around 2 μm from $80/\sqrt{12}$ μm. In practice, given limited statistics and an imperfect distribution shape, the RMS can only be determined with an accuracy of 5 μm. It is therefore not surprising that the alignment file and mechanically measured angles disagree at $\theta_d \approx 0^o$.

At larger angles, the RMS is seen to increase more rapidly with $|\theta_d - \theta_a|$. Since θ_d and θ_a agree at larger angles, the mechanically found angle is assumed to be correct at all angles and is used as the detector angle in the following analyses.

4.4 Offline data analysis

Both binary modules were positioned such that the majority of beam particles passed through a 6 cm region. Only events in which the particle trajectory, reconstructed from the telescope modules, passed through the inner 124 strips of this region have been used in the following analysis. Bad channels in the two modules were identified using the algorithm described in section 3.4.1.

4.4.1 Event selection

Beam particle trajectories were found using hits in at least three of the four telescope modules. Only events in which just one track was reconstructed were used in the analysis. This eliminated any ambiguity as to which track a hit in a binary module should be attributed. If the particle traversed the binary module within $\pm 160\ \mu$m of a bad channel the event was discarded. If a cluster of 10 strips or wider was found in the binary module that event was also discarded. The first event in each burst of beam particles was always inefficient and was not used.

The module efficiency was found to be uniform with the time between scintillator trigger and read-out clock pulse within the 25 ns window. No cuts on the TDC measured time were therefore necessary.

For reasons not fully understood, the raw data hitmap of detector strips was shifted to the right by 8 bits in around 2% of events. In the raw data, the hitmap for each CDP is preceded by some header information added by the HAC chip. In shifted events, the last eight bits of this header were interpreted as the first eight read-out channels of a CDP chip. The shifted events could be identified by a high occupancy in the first 8 channels of each CDP chip and were discarded.

With the above described cuts, both modules exhibited a maximum efficiency (see below for definition), with respect to bias voltage and threshold, of around 97%. In over two thirds of inefficient events it was found that both binary modules were inefficient suggesting a source of inefficiency related to the binary read-out system rather than individual detectors. Such an efficiency is not of interest and was eliminated by using the binary module not being investigated as an anchor plane and requiring it to be efficient in a good event. Doing this raised the maximum efficiency of both detectors above 99%.

All events passing the above criteria were used in the subsequent module analysis. Typically 7000 good events were obtained from a 25000 event run.

4.4.2 Definitions of efficiency and noise occupancy

The definitions of efficiency and noise occupancy are identical to those used in chapter 3:

- An event is efficient if there is a hit strip within ± 160 μm of the particle trajectory as found using the telescope modules.
- A noise hit is outside of ± 200 μm of the track intersect.
- The noise occupancy of a run is the average number of noise hits in an event as a fraction of the number of good channels in the detector region being studied.

4.4.3 The data sample

Data were taken with and without an applied magnetic field. Without a magnetic field, a bias scan was performed with the detector angle, θ_d=0^o. With the magnetic field, data were taken at several bias voltages and with $-20^o \leq \theta_d \leq 15^o$. In p-in-n detectors, holes are collected at the strip surface. Using equation 2.10 and a hole Hall mobility of 0.0358 m^2 V^{-1}s^{-1} [35], the expected Lorentz angle can be calculated to be -3.2^o in the 1.56 T field of the Morpurgo magnet. The variation of detector performance with angle was expected to be symmetric around the Lorentz angle, hence the range of θ_d. Data were taken with LBIC discriminator thresholds of 1.0 fC and 1.3 fC. This threshold is referred to as the binary threshold, or simply the threshold, in this chapter. A 1.0 fC binary threshold will be used in ATLAS.

4.5 Results

4.5.1 Module efficiencies with no magnetic field

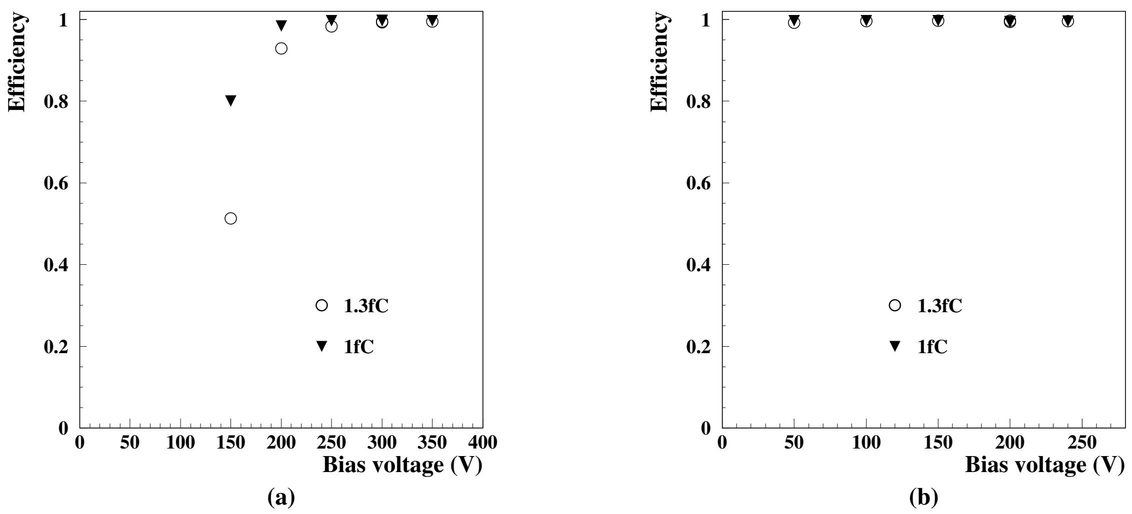

Figure 4.4: The efficiency of **(a)** the irradiated and **(b)** the unirradiated modules plotted against bias voltage for two binary thresholds. There was no magnetic field and the beam particles were normally incident.

In figure 4.4a, the efficiency of the irradiated module is shown as a function of bias voltage and for two binary thresholds. The detector reached full efficiency between 200 V and 250 V for a 1 fC threshold and at 300 V for a 1.3 fC threshold. Full detector efficiency therefore approximately coincides with the full charge collection voltage. These results are consistent with measurements made on the same detector in the November 97 test beam.

The unirradiated module is seen in figure 4.4b to be fully efficient down to the lowest measured bias voltage of 50 V. In unirradiated p-in-n detectors, the depletion region grows from the strip side and therefore fully efficient operation of the detector below the depletion voltage of 65 V is expected.

4.5.2 Detector efficiencies is a magnetic field

Figures 4.5a and 4.5b show the variation with bias voltage of the irradiated detector efficiency in the Morpurgo magnet and at three detector angles. Full efficiency is reached at a similar voltage to that found without a magnetic field. Figures 4.5c and 4.5d show the unirradiated detector to be fully efficient above 50 V at all angles investigated. The two modules satisfy the requirements of fully efficient operation above 150 V before irradiation and above 300 V after irradiation (section 2.6).

Figures 4.6a and 4.6b show the variation of detector efficiency with binary threshold for $\theta_d = -15^o$, 0^o and 15^o. The irradiated module shows a small loss of efficiency above 1 fC when biased at 300 V. No such loss is seen in the unirradiated detector biased at 200 V.

A binary detector is inefficient when the charge collected on the strip nearest to the track is below the binary threshold. A particle traversing a 300 μm thick detector parallel to the detector normal produces a most probable charge of 4 fC [39]. The charge collected at the strips is reduced by a smaller sensitive volume when the detector is operated below full depletion and by inefficient charge collection.

The sharing of charge between two or more strips also decreases the charge collected

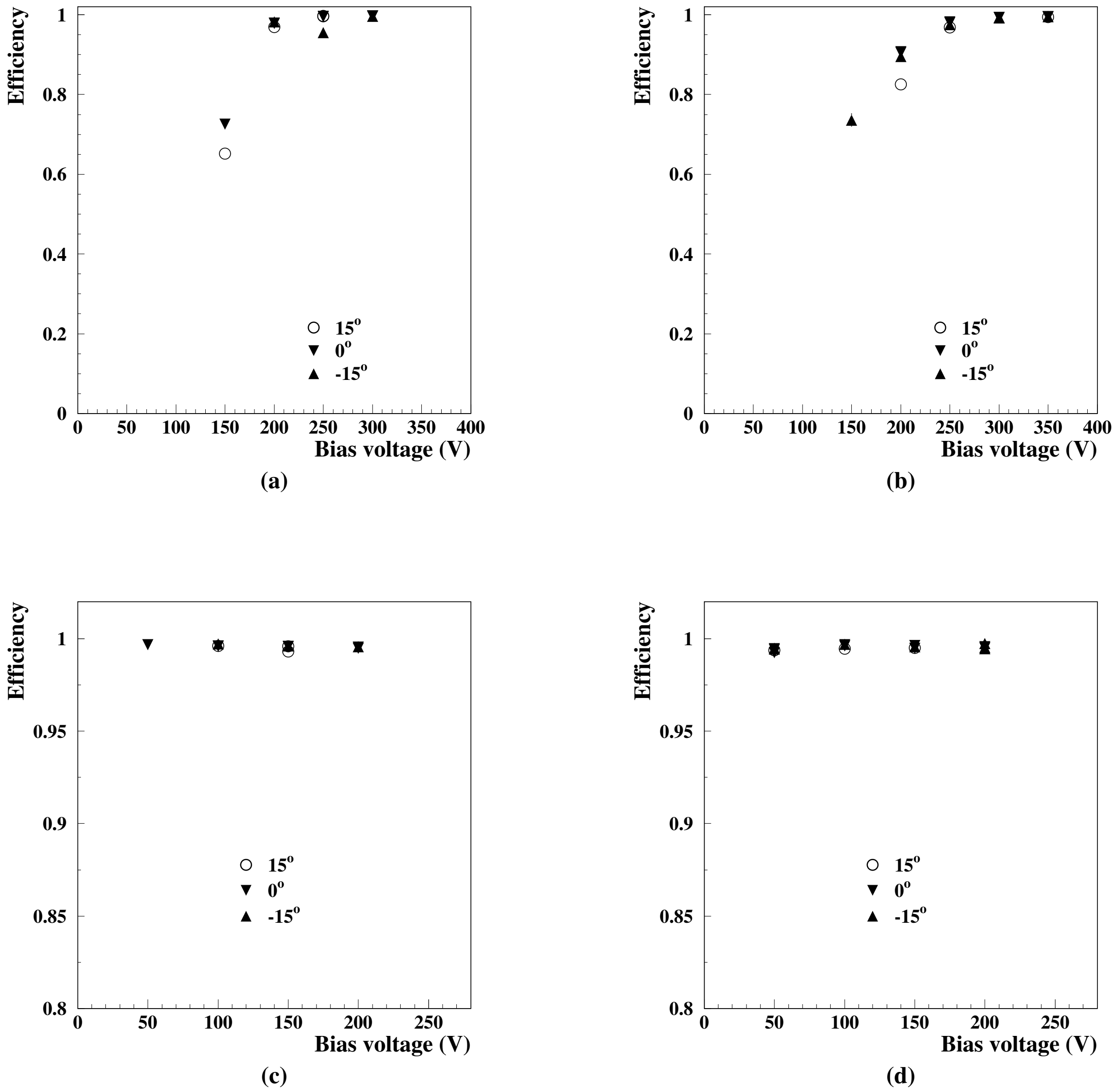

Figure 4.5: Module efficiency in a magnetic field plotted against bias voltage for various detector angles for the irradiated detector with a binary threshold of **(a)** 1.0 fC and **(b)** 1.3 fC and the unirradiated detector at **(c)** 1.0 fC and **(d)** 1.3 fC.

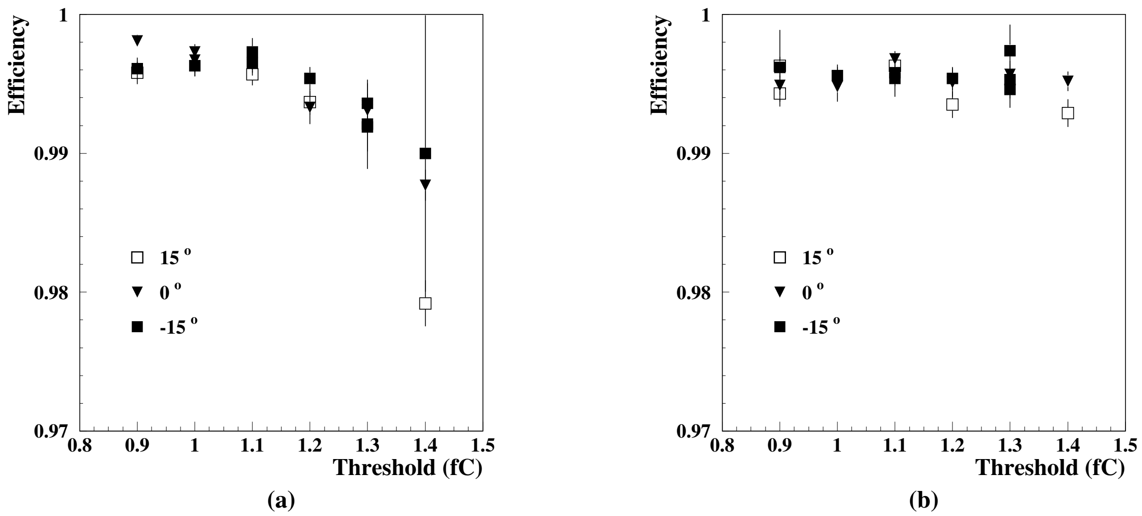

Figure 4.6: Module efficiency in a magnetic field plotted against binary threshold and detector angle for **(a)** the irradiated detector biased at 300 V and **(b)** the unirradiated detector biased at 200 V.

on any one strip and can affect the detector efficiency. For normally incident particles the probability of charge sharing is largest when the particle passes between two strips. The track η is a measure of the position of a track with respect to the strip positions and is defined:

$$\eta = \frac{x_t - x_s}{p} \tag{4.1}$$

where x_t is the local coordinate of the track intersect with the detector, x_s is the local position of the centre of the nearest strip to the left of the track and p is the strip pitch. A track with $\eta = 0.5$ passes through the centre of the inter-strip region where charge sharing should be maximal. In figure 4.7, the irradiated detector efficiency is plotted against η for two bias voltages and two thresholds. The efficiency is seen to be lowest at $\eta = 0.5$ where the collected charge, when shared between two strips, is below the binary threshold.

The sharing of charge between strips is increased when particles are non-normally

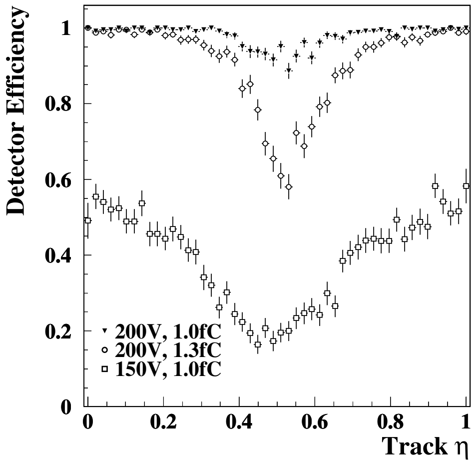

Figure 4.7: The irradiated module efficiency plotted against track η for two bias voltages and two binary thresholds. The detector angle, $\theta_d = 0^o$ and the magnetic field is turned on.

incident on the detector. When the angle between a particle path and the normal to the detector plane is greater than 15^o, the particle will always pass under two strips of a 300 μm thick, 80 μm pitch detector. The increased charge produced by the longer particle path length in the silicon does not fully compensate for this charge sharing and some detector inefficiency can occur at larger angles. In figures 4.8a to 4.8d, detector efficiency is plotted against detector angle. The irradiated detector shows some loss of efficiency at absolute angles greater than 10^o when the binary threshold is 1.3 fC. At a bias voltage of 200 V and threshold of 1.3 fC, the efficiency is highest at -5^o which is close to the expected Lorentz angle. No loss of efficiency at larger angles is seen in the unirradiated detector when biased at 100 V.

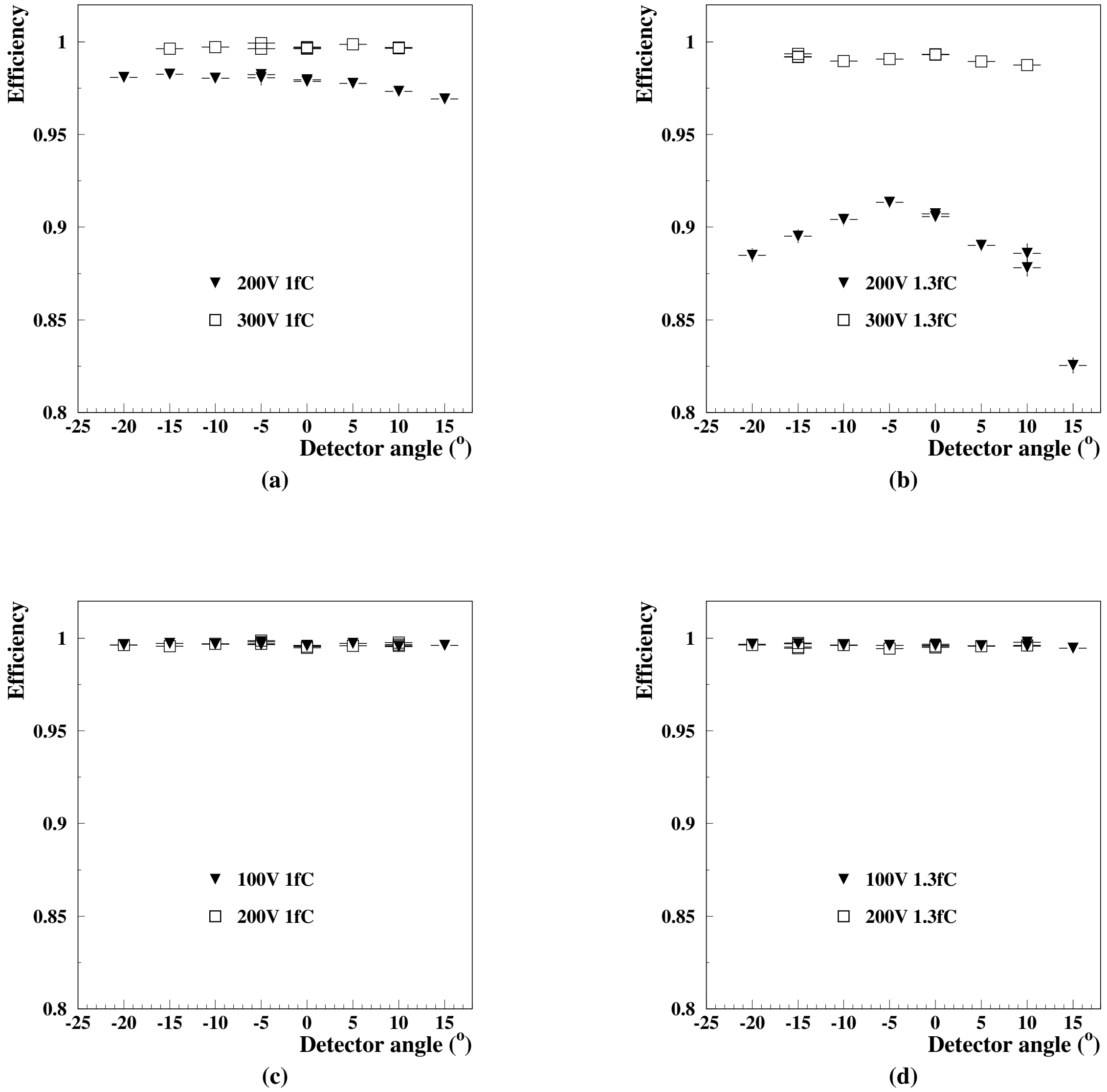

Figure 4.8: Detector efficiency in a magnetic field plotted against detector angle and bias voltage. Plots **(a)** and **(b)** show the irradiated detector efficiency at 1.0 fC and 1.3 fC respectively and **(c)** and **(d)** show the unirradiated detector results.

4.5.3 Two-strip clusters

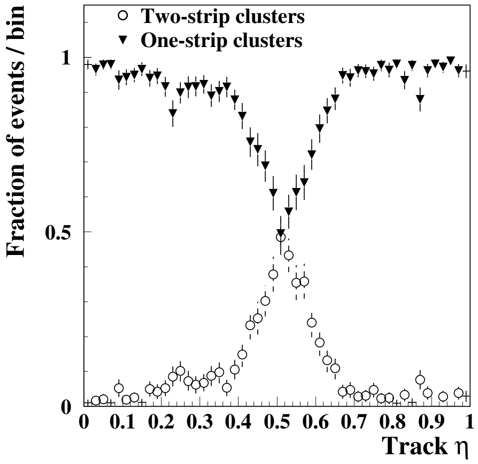

Figure 4.9: The fraction of clusters with one and two strips plotted against η for the unirradiated detector biased at 150 V and with a threshold of 1.0 fC. The beam particles are normally incident and the magnetic field is turned off.

A consequence of charge sharing between strips is the production of clusters of contiguous hit strips. When a detector is not in a magnetic field, normally incident particles only produce two-strip clusters when they pass through an inter-strip gap. This can be seen in figure 4.9 where the distribution with track η of one and two-strip clusters is plotted for the unirradiated module. A peak in the occurance of two-strip clusters is seen at $\eta = 0.5$.

As a detector is rotated away from perpendicular to the beam, the charge sharing between strips and the fraction of two-strip clusters increase. In figures 4.10a-d, the fraction of matched clusters with two strips is plotted against the detector angle, θ_d. A cluster is matched if its centre is within ± 160 μm of the telescope track.

For a binary threshold of 1 fC, the fraction of clusters with two strips in the unirradiated detector rises from a minimum of 0.13 at small angles to over 0.6 at -20^o. The

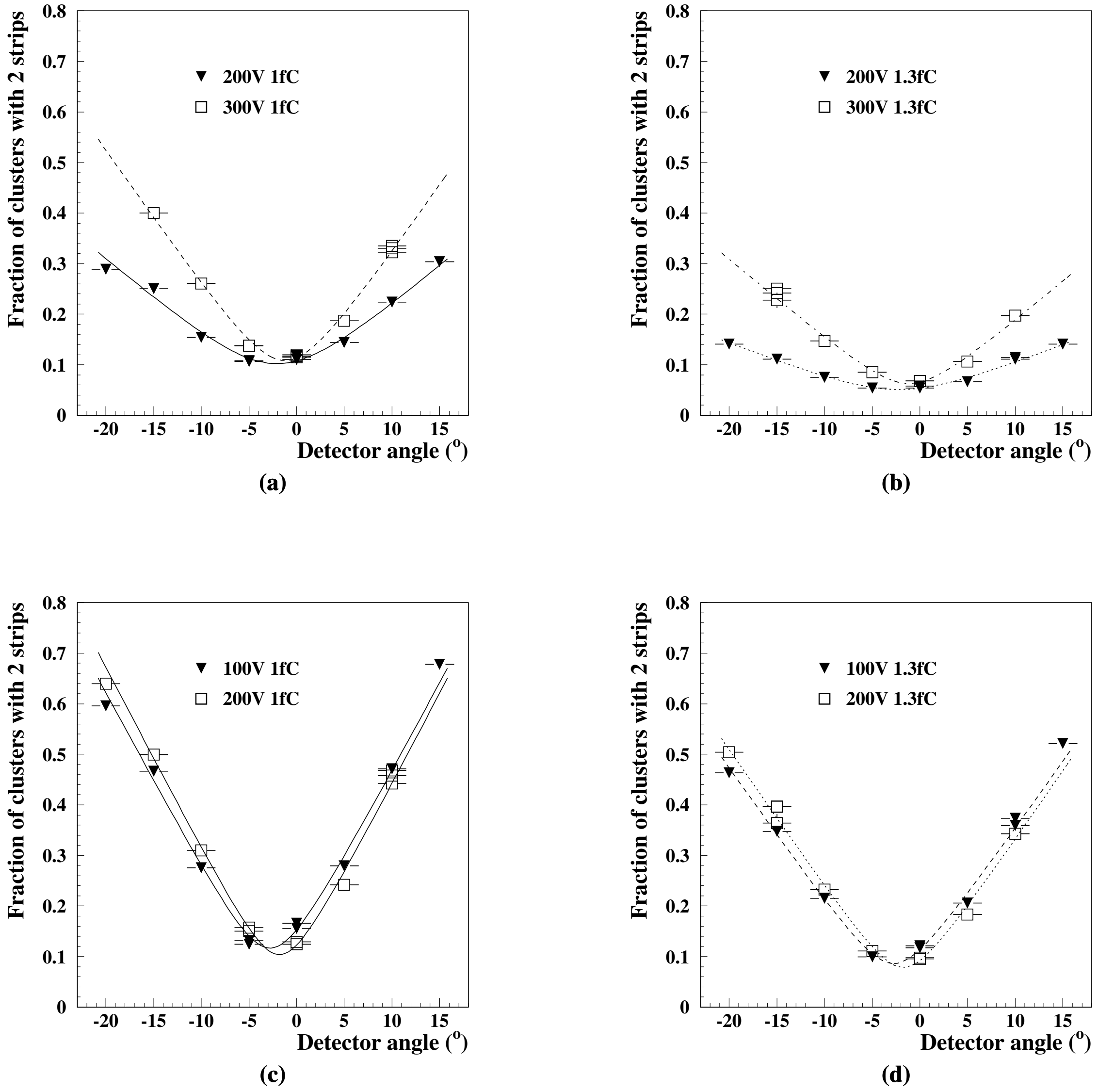

Figure 4.10: The fraction of clusters with two strips plotted against detector angle for **(a-b)** the irradiated detector and **(c-d)** the unirradiated detector. Parabolas have been fitted to the points. The angles of the curve minima are listed in table 4.2.

frequency of two-strip clusters at a given detector angle varies little when the bias voltage is increased from 100 V to 200 V. This suggests that the charge collection efficiency is already at a maximum at 100 V. As expected, there are fewer two-strip clusters when the binary threshold is raised to 1.3 fC.

At both bias voltages and both thresholds shown, the irradiated detector has a lower frequency of two-strip clusters at a given angle than the unirradiated detector. The difference is small when the irradiated detector is biased at 300 V. This suggests that charge collection in the irradiated detector is close to maximal at around 300 V which agrees with measurements made with analogue electronics [56, 67].

Module	Bias voltage (V)	Threshold (fC)	Angle at minimum (^{o})
1	200	1.0	-2.1
1	300	1.0	-1.2
1	200	1.3	-2.2
1	300	1.3	-1.1
2	100	1.0	-2.8
2	200	1.0	-1.8
2	100	1.3	-2.8
2	200	1.3	-1.7

Table 4.2: The angle at which the parabolas in figure 4.10 are at a minimum. The average angle is -2.0 ± 0.1^o

Minimal charge sharing occurs when the spatial distribution of charge collected at the strip surface is narrowest. It will be shown in section 4.5.4 that this is achieved when the detector angle is equal to the Lorentz angle. The minima in plots 4.10a-d therefore provide a measure of the Lorentz angle in the 1.56 T Morpurgo magnet. Parabolas have been fitted to the experimental points and the minima of these curves are listed in table 4.2. The average angle of the minimum is -2.0 ± 0.1^o, where the error has been calculated using the spread of the values in table 4.2. This value is smaller than the theoretically predicted $\theta_L = -3.2^o$.

4.5.4 Comparison with a model of charge distribution

A model of charge production and diffusion in silicon detectors in magnetic fields has been developed by E. Belau et al. in [42]. To compare this model with the experimental two-strip cluster frequency results, a simple simulation of a silicon detector was developed.

In [42], Belau et al. derive a theoretical spatial distribution of charge at the strip surface of a fully depleted detector. The model assumes that particles are normally incident on the detector. The first step in calculating the distribution is to assume that charge is produced in a cylinder around a traversing particle. The second step is to consider the drift of this charge due to the electric field of the applied bias, a magnetic field and diffusion.

The distribution from [42] was modified to take into account particles incident at an angle to the detector normal. In figure 4.11, the predicted charge distribution at the strip surface is shown for two detector angles ($\theta_d = 0^o$ and $\theta_d = 3.2^o$) both with and without a magnetic field. The origin of the horizontal axis corresponds to the position of entry of the particle into the back of the detector. A magnetic field and non-normally incident particles are seen to broaden the charge distribution. When the Lorentz and detector angles are finite and equal, the charge distribution is seen to be displaced but of the same width as when $\theta_d = \theta_L = 0$.

The theoretical spatial charge distribution was used in a simulation of a 300 μm thick, 80 μm pitch detector. The detector surface was segmented into 80 μm regions, each representing the area from which charge would be collected by one read-out strip. For a given track η and detector angle, the surface charge distribution was found and integrated over these 80 μm regions to give the charge on each strip. The resulting cluster width can be found by comparing this charge with the binary threshold. For

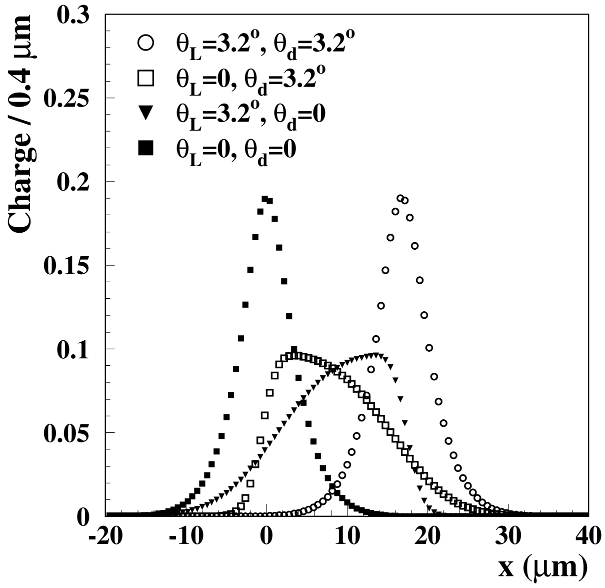

Figure 4.11: The theoretical spatial distribution of charge collected at the strip side of a detector for two detector angles (θ_d) and with ($\theta_L \neq 0$) and without ($\theta_L = 0$) a magnetic field. See text for details of the simulation used.

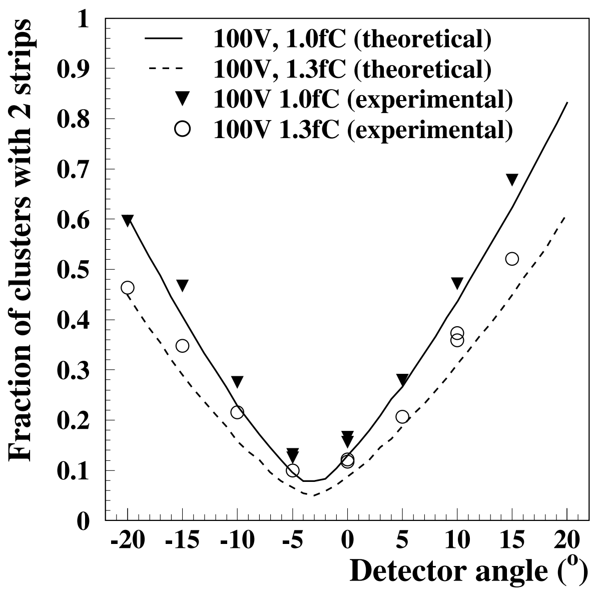

Figure 4.12: The theoretical variation with detector angle of the fraction of clusters with two strips for a bias voltage of 100 V and binary thresholds of 1.0 fC and 1.3 fC (lines). The test beam results for the unirradiated detector, previously shown in figure 4.10, have been superimposed on the plot.

a fixed track angle, the cluster width depends only on the track η. The theoretical fraction of clusters with two strips was found by sampling the cluster width at many points between $\eta = 0$ and $\eta = 1$.

The simulation was used to model the behaviour of the unirradiated detector in the test beam. The depletion voltage of the simulated detector was set to 65 V and a Lorentz angle of -3.2^o was chosen. Figure 4.12 shows the simulation predicted variation of the frequency of two-strip clusters with detector angle. The experimentally found points, previously shown in figures 4.10c and 4.10d, have been superimposed on the plot. The experimental data and theoretical curves are seen to be in good agreement, given that capacitive coupling between strips is not included in the simulation.

4.5.5 Detector precision

If only the nearest strip to a particle track records a hit in a binary detector of pitch p, the residual distribution has an RMS width of $p/\sqrt{12}$. It was demonstrated in the previous section that, even with minimal charge sharing, some two-strip clusters are formed.

The position of a multi-strip cluster is the average position of its strips. The position of a two-strip cluster is the centre of the inter-strip gap. For normally incident particles, two-strip clusters are only produced by particles with a track $\eta \approx 0.5$ and the distribution of residuals for two-strip clusters is therefore narrower than $p/\sqrt{12}$. In figure 4.13a, the residual distributions for one and two-strip clusters are plotted for the unirradiated detector with $\theta_d = 0^o$ and with the magnetic field turned on. The distribution for two-strip clusters is seen to be narrower than that for one-strip clusters. The one-strip cluster distribution differs from the theoretical top-hat function in having finite gradient edges due to multiple scattering of beam particles and the finite spatial resolution of the telescope modules. The residual distribution for all cluster widths is shown in figure 4.13b.

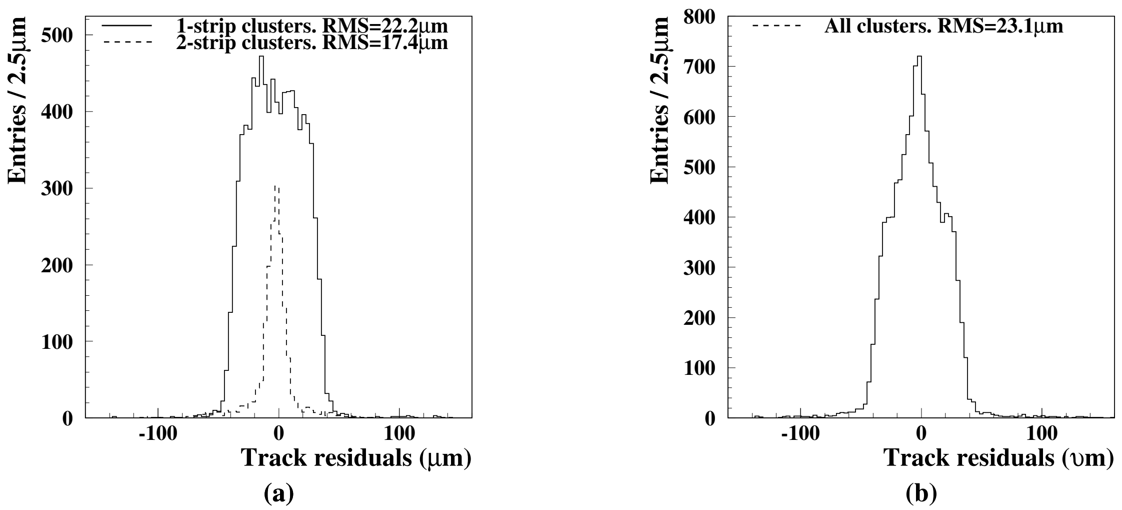

Figure 4.13: The track residual distribution for **(a)** one and two-strip clusters and **(b)** all clusters. The distributions are from the unirradiated detector biased at 200 V and with a binary threshold of 1.0 fC. The magnetic field is turned on and beam particles are normally incident.

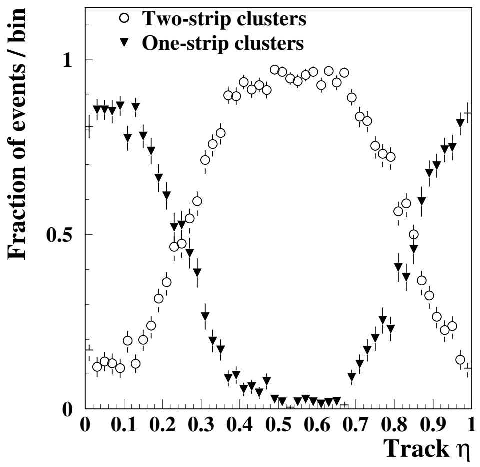

Figure 4.14: The fraction of one and two-strip clusters plotted against η for the unirradiated detector biased at 100 V, with a binary threshold of 1.0 fC and with $\theta_d = -20^o$. The magnetic field is turned on.

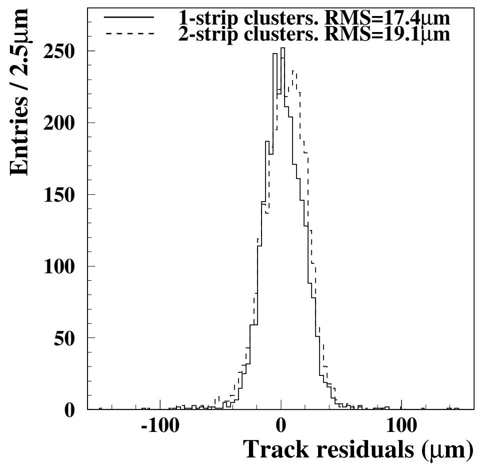

Figure 4.15: The track residual distributions for one and two-strip clusters for the unirradiated detector in a magnetic field, biased at 100 V, with a binary threshold of 1.0 fC and with $\theta_d = +15^o$.

Figure 4.14 shows the fraction of one and two-strip clusters plotted against η for the unirradiated module with $\theta_d = -20^o$. By comparing figures 4.14 and 4.9 it is seen that the inter-strip region in which two-strip clusters are formed is wider for a larger detector angle. This widening results in a broader two-strip cluster distribution. Figure 4.15 shows residual distributions of the unirradiated detector at an angle, $\theta_d = +15^o$. The single-strip distribution narrows because the region around a strip in which such clusters are formed becomes smaller.

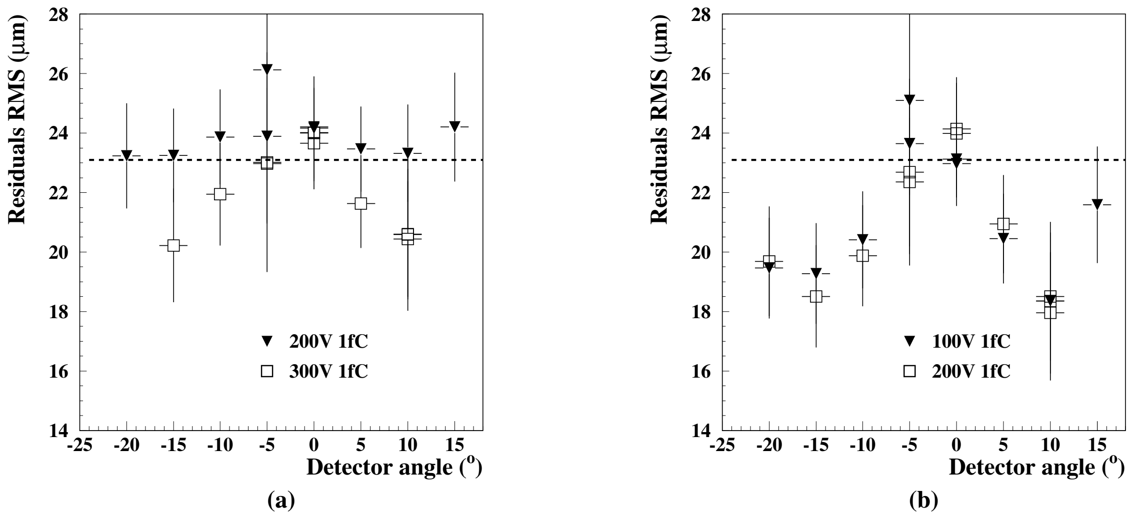

Figure 4.16: The RMS width of the residual distribution for **(a)** the irradiated and **(b)** the unirradiated modules in a magnetic field plotted against detector angle. The dashed line indicates the top-hat distribution RMS width of 23.1 μm.

Figures 4.16a and 4.16b show the residual distribution RMS width as a function of θ_d for two bias voltages and for a binary threshold of 1.0 fC. The data were taken with the magnetic field turned on. All matched clusters of a run have been used to find the widths plotted. A maximum cluster width of 10 is imposed by good event selection cuts. At the Lorentz angle, the RMS width is close to the expected value of $80/\sqrt{12}\ \mu\text{m} = 23.1\ \mu$m. The precision improves either side of the Lorentz angle until $|\theta_d - \theta_L| \approx 10^o$. Beyond this point the precision appears to worsen. Similar residual RMS widths were found using a binary threshold of 1.3 fC.

4.5.6 Noise occupancy

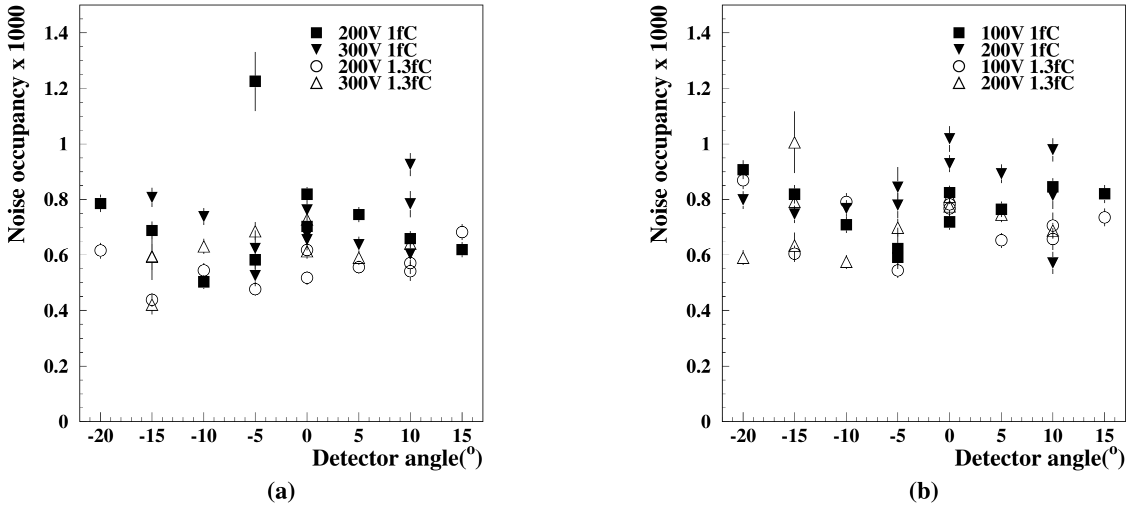

Figure 4.17: The noise occupancy of **(a)** the irradiated detector and **(b)** the unirradiated detector plotted against detector angle, bias voltage and binary threshold.

The noise occupancy of the two modules is plotted against detector angle in figure 4.17. No variation with angle is seen. As expected, the noise is higher for the lower binary threshold of 1.0 fC. The noise in the unirradiated module is slightly higher than in the irradiated module.

The observed noise occupancy is marginally higher than the maximum of 5×10^{-4} given in the SCT module specifications (section 2.6). The FEE used in this test beam are, however, not the chosen ATLAS final solution.

4.6 Conclusions

The performance of two p-in-n silicon microstrip detectors in a magnetic field and with non-normally incident particles has been studied. The unirradiated detector demonstrates full charge collection and fully efficient operation at bias voltages above 50 V for binary thresholds of 1.0 fC and 1.3 fC. Full charge collection and fully efficient operation of the irradiated detector are observed above a bias voltage of 300 V. A plateau efficiency greater than 99% was observed in both modules. With a sufficiently high bias voltage to give fully efficient operation at $\theta_d = 0$, neither detector showed any loss of efficiency for $|\theta_d - \theta_L| < 15^o$ with a binary threshold of 1.0 fC. Some loss is observed, however, in the irradiated detector when the binary threshold is raised to 1.3 fC. For the range of angles of incident particles expected in the ATLAS SCT, both modules satisfy the module operating voltage and efficiency specifications.

Charge sharing was shown to be minimal when the detector angle, θ_d, and Lorentz angle, θ_L, are equal. The Lorentz angle in a 1.56 T magnetic field was measured to be 2.0 ± 0.1^o. The fraction of clusters with two strips, a measure of charge sharing, increases with $|\theta_d - \theta_L|$. The experimentally measured variation is found to be in good agreement with predictions from a theoretical model of charge production and diffusion.

A detector precision of better than 24 μm was found for both modules. The noise occupancy is of the order of 7×10^{-4} and close to the maximum occupancy permitted by the SCT module specifications.

Chapter 5

Explicit R-parity violation in SUSY

5.1 Introduction

Supersymmetry (SUSY) is one of the most theoretically favoured extensions of Standard Model physics. This chapter investigates the possibility of discovering and measuring the mass of three SUSY particles in a baryon number violating scenario.

Chapter 1 discussed the concept of and motivations behind SUSY. The first part of this chapter describes a specific SUSY model and R-parity violation. The software tools used to generate SUSY events and to model the ATLAS detector performance are then discussed. The subsequent section describes the phenomenology of the SUSY scenario studied. Finally, the algorithm used to extract SUSY particle masses is discussed and results are presented.

5.2 Supersymmetry

5.2.1 The Minimal Supersymmetric Standard Model

The Minimal Supersymmetric Standard Model (MSSM) is the supersymmetric extension of the SM with minimal particle content. As in the SM, there are three families of leptons and quarks. Each of the SM fermions has a SUSY partner. Two complex Higgs doublets are needed to give mass to all fermions and there are five physical, spin-zero Higgs bosons: A, $H^{\pm}$, H^0 and h^0. These have spin-half superpartners called higgsinos. The superpartners of the $W^{\pm}$ and Z bosons mix with the higgsinos to give mass eigenstates: the charginos, $\tilde{\chi}^{\pm}_{1,2}$, and neutralinos, $\tilde{\chi}^{0}_{1,2,3,4}$.

The MSSM has 105 more free parameters than the Standard Model [7]. Phenomenological observations such as small CP violation and the lack of flavour changing neutral currents can be used to constrain the MSSM to 19 extra free parameters [73]. Another method of constraining the MSSM is to impose boundary conditions on parameters at the Grand Unification Theory (GUT) scale. One such constrained model, minimal supergravity or mSUGRA [74], involves gravitational interactions in SUSY breaking and automatically fulfils the phenomenological MSSM constraints [73]. The SUSY sector of mSUGRA is defined by the following boundary conditions [7]:

1. Gauge coupling strengths are equal at the GUT scale, M_U. This condition can be used to define M_U.

2. All gauginos have a mass $m_{\frac{1}{2}}$ at M_U.

3. Scalar sparticles have a mass m_0 at M_U.

4. All trilinear Higgs-sfermion-sfermion couplings are equal to A_0 at M_U.

mSUGRA point	m_0 (GeV)	$m_{\frac{1}{2}}$ (GeV)	A_0 (GeV)	$\tan\beta$	signμ
1	400	400	0	2.0	$+$
2	400	400	0	10.0	$+$
3	200	100	0	2.0	$-$
4	800	200	0	10.0	$+$
5	100	300	300	2.1	$+$
6	200	200	0	45	$-$

Table 5.1: The values of the mSUGRA parameters at the six LHC points [20, 21].

In addition to m_0, $m_{\frac{1}{2}}$ and A_0, a further two input parameters are needed: β, the ratio of the vacuum expectation values of the two Higgs doublets and the sign of the SUSY conserving Higgs mass, μ. SUSY measurement and detection studies in ATLAS have concentrated on the six points in the mSUGRA parameter space listed in table 5.1. At each of these points, the lightest supersymmetric particle (LSP) is the χ_1^0.

In the majority of ATLAS mSUGRA studies it is assumed that a discrete, multiplicative symmetry, R-parity, is conserved. The R quantum number of a particle is defined:

$$R = (-1)^{3B+L+2S} \tag{5.1}$$

where B, L and S are the baryon number, lepton number and spin of the particle [75]. Leptons and sleptons have $L = +1$, $B = 0$ and anti-leptons and anti-sleptons have $L = -1$, $B = 0$. Quarks and squarks have $L = 0$, $B = \frac{1}{3}$. It follows that SM particles have $R = 1$ and supersymmetric particles have $R = -1$. The R quantum number of a system of particles is the product of the individual particles' R quantum numbers. If R-parity is conserved, supersymmetric particles must be produced in pairs and the decay products of a SUSY particle must include an odd number of SUSY particles. A consequence of R-parity conservation is that the LSP is stable. In mSUGRA, the

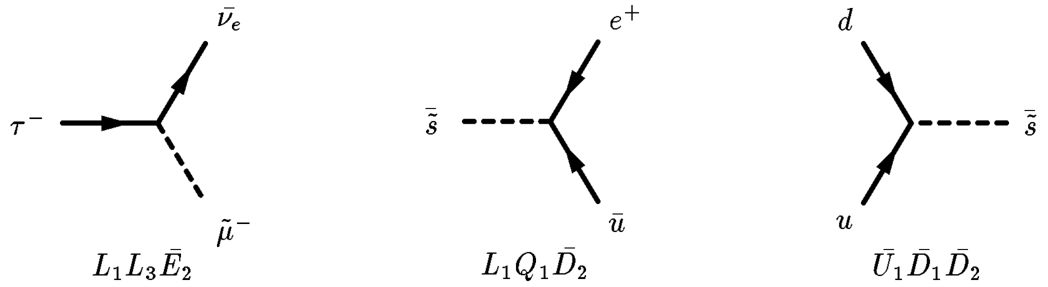

Figure 5.1: Examples of vertices introduced by the LLE, LQD and UDD terms in the R-parity violating superpotential.

weakly interacting and neutral $\tilde{\chi}_1^0$ is the LSP and is assumed to leave the detector without interacting. A signature of R-parity conserving (RPC) mSUGRA is therefore missing transverse energy.

The conservation of R-parity is principally motivated by the long measured lifetime of the proton ($\tau(p \to e\pi) > 10^{32}$ years [39]). To understand this, it is easiest to consider first the terms added to the R-parity conserving MSSM superpotential to introduce R-parity violation (RPV) [75]:

$$W_{\not{R}_p} = \frac{1}{2}\lambda_{ijk} L_i L_j \bar{E}_k + \lambda'_{ijk} L_i Q_j \bar{D}_k + \frac{1}{2}\lambda''_{ijk} \bar{U}_i \bar{D}_j \bar{D}_k \tag{5.2}$$

In the SUSY Lagrangian, SM and SUSY particles are grouped together into lepton (L_i) and quark (Q_i) SU(2) doublet superfields and electron (E), down(D) and up(U) SU(2) singlet superfields. In equation 5.2, λ_{ijk}, λ'_{ijk} and λ''_{ijk} are Yukawa couplings between these superfields. The subscripts i, j and k are family indices. λ_{ijk} is antisymmetric under $i \leftrightarrow j$ and λ''_{ijk} is antisymmetric under $j \leftrightarrow k$. $W_{\not{R}_p}$ therefore adds $9 + 27 + 9 = 45$ free parameters to the MSSM superpotential.

Figure 5.1 shows examples of R-parity violating vertices introduced by the LLE, LQD and UDD terms in equation 5.2. The LLE and LQD terms are seen to violate lepton number conservation and the UDD term baryon number conservation.

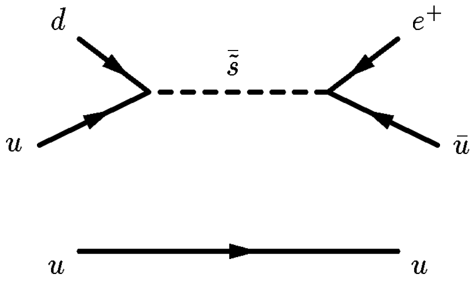

Figure 5.2: Proton decay via the R-parity violating $L_1Q_1\bar{D}_2$ and $\bar{U}_1\bar{D}_1\bar{D}_2$ vertices.

Proton decay can occur, for example, via the $L_1Q_1\bar{D}_2$ and $\bar{U}_1\bar{D}_1\bar{D}_2$ vertices (figure 5.2). The lifetime of the proton has been measured to be greater than 10^{32} years [39] and, for the given example, this imposes $\lambda'_{112}.\lambda''_{112} \lesssim 2.10^{-27}(\frac{\tilde{m}}{100\ \mathrm{GeV}})^2$ [75] where $\tilde{m}$ is the mass of the exchanged strange squark. It is therefore natural to set one of the two Yukawa couplings to zero which is equivalent to conserving either lepton or baryon number. Both lepton and baryon number violation are needed for proton decay. RPV couplings are also constrained by limits on contributions, via the exchange of virtual SUSY particles, to other SM processes [75, 76].

RPV models consistent with current measurements can be constructed. In [75], it is argued that there are no theoretical or phenomenological reasons to favour RPC models over RPV models. It is therefore important to consider the discovery and measurement potential of both scenarios.

The difference in signature between RPV and RPC SUSY models depends on the strength of the RPV coupling. When RPV couplings are small compared to MSSM gauge couplings, the predominant consequence of R-parity violation is that the LSP can decay into SM particles. For RPV couplings of order 10^{-6} or smaller [77], the LSP has a sufficiently long lifetime to decay outside of the detector. The experimental signature is then identical to that of an RPC model. If RPV couplings are in the range $10^{-4} < \lambda, \lambda', \lambda'' < 10^{-2}$ [77], the LSP decays in the beam pipe and the missing energy signature, seen in RPC models, is not present.

If the RPV couplings and MSSM gauge couplings are of the same order of magnitude, RPV production processes and decays of particles heavier than the LSP become important. For a large λ'' coupling, for example, the branching fractions of RPC and RPV decays of a squark can be of the same order of magnitude.

5.3 Event simulation

For this analysis, events were generated using a private version of HERWIG. ATLFAST 2.0 [78] was used to simulate the ATLAS detector.

5.3.1 Event generation

In June 1999, the publicly available release of HERWIG was version 5.9 [79]. The release of a new version 6.1 [80,81] was planned later in the year. Whilst HERWIG 5.9 simulates just SM particles, versions from 6.0 upwards include the production and decay of MSSM particles. Version 6.1 also incorporates R-parity violating interactions.

The private version 6.0 used in this analysis includes all RPC SUSY processes and a subset of all RPV interactions. The limitations of this private version are described later in this section.

HERWIG generates SUSY events using a list of sparticle masses and decay modes. This information is produced using a modified version of ISASUSY [82]. ISASUSY iteratively solves the renormalisation group equations (RGE) of a given SUSY model. The RGEs are then used to evolve the free parameters of the model to find sparticle masses and couplings at the electroweak (EW) breaking scale. SUSY models implemented in ISASUSY include mSUGRA, non-universal SUGRA and gauge-mediated SUSY breaking (GMSB). The modified ISASUSY includes R-parity violating decays calculated for user defined values of the RPV Yukawa couplings (equation 5.2).

HERWIG factorises event generation into four subprocesses: Initial state radiation (ISR), the elementary hard process, final state radiation (FSR) and hadronisation. The colour flow through an event is recorded and used by HERWIG in hadronisation. In baryon number violating decays, the colour connection of an event is non-trivial and HERWIG 6.0 was modified to deal with such processes.

Not all RPV vertices are included in the version of HERWIG used for this analysis. The following processes are included:

1. All two-body squark and slepton decays

2. All three-body neutralino decays

3. The RPV production process $qq \rightarrow \tilde{\chi}_1^0 l^{\pm}$ via the LQD term (equation 5.2)

Three-body chargino and gluino RPV decays are not included and only the above-mentioned RPV production process is implemented.

As discussed in the previous section, RPV production and RPV decays of particles other than the LSP are only important for large RPV couplings. This version of HERWIG is therefore adequate for studies where the RPV coupling is small and only the decay of the LSP is important.

When the analysis of this chapter was near completion, a revised version 6.02 of HERWIG became available. HERWIG 6.02 and HERWIG 6.0 differ in two ways relevant to this work. Firstly, the QCD renormalisation scale at which SUSY production is calculated was lowered in HERWIG 6.02, raising α_s and the total SUSY production cross section. The total cross section in the new version is in good agreement with

ISAJET 7.40 [82] and PROSPINO [83]. At mSUGRA point 5, the cross section is 20 % higher in the newer version of HERWIG than in HERWIG 6.0. Too much significance should not be placed on this 20% difference because the error on the total production cross section could be of the same order. Changing the parton distribution functions can change the SUSY cross section by 10 % and corrections of second order and higher, which are not implemented in HERWIG, may have a similar order effect.

The second difference in HERWIG 6.02 is the correction of an error in the sign of a chargino-neutralino-W coupling. With the correct sign, some cancellation occurs which reduces the associated neutralino and chargino production cross section. At point 5, the fractional production cross section is 14.6 % in HERWIG 6.0 and 7.7 % in HERWIG 6.02. All implicit signatures used in this analysis are from squark and gluino production and therefore the results presented here should be slightly pessimistic. The ratios of SUSY production rates quoted in this chapter are taken from HERWIG 6.0. The individual process production rates, however, have been scaled to give a total SUSY cross section which agrees with HERWIG 6.02.

5.3.2 ATLAS detector simulation

Detector simulation can be performed at three levels of sophistication. The most sophisticated simulations are full Monte Carlo studies which track individual particles through a detailed description of the detector geometry and material. Such simulations agree well with experiment but are slow and CPU intensive. At the other end of the spectrum are parton level simulations. These determine the topology of an event from its partons and leptons. There is, for example, no hadronisation of partons or taus.

Particle level simulations are a compromise between the fast but approximate parton level simulations and the accurate but slow full Monte Carlos. The stable, final state particles remaining after the hadronisation of quarks are the starting point of the simulation. In particle level simulations, all stable particles except neutrinos, muons and the SUSY LSP (if stable) are used to determine the energy deposited in a grid in (η, ϕ) space representing calorimeter cells. From a list of the energy in each cell, jets can be reconstructed. The energy deposited around an electron or muon can be used to determine whether it is isolated. Parameters such as the transverse momentum of an electron or the missing transverse momentum of an event are known from the particle generator and can be smeared to model detector inaccuracy as measured in test beams and full Monte Carlo simulations.

ATLFAST, a particle level simulation of the ATLAS detector, is described in more detail below.

Energy deposition in ATLFAST

In ATLFAST, calorimeter cells are of dimension $\Delta\eta \times \Delta\phi = 0.1 \times 0.1$ in the barrel ($|\eta| < 3$) and $\Delta\eta \times \Delta\phi = 0.2 \times 0.2$ in the forward regions ($3 < |\eta| < 5$). These cell sizes correspond approximately to the hadronic calorimeter cell sizes in the ATLAS detector [31]. From a list of stable particles generated by an event generator such as HERWIG, the energy deposited in each calorimeter cell is found. The effect on charged particles of the Inner Detector's solenoidal 2 T magnetic field is taken into account.

Calorimeter cell clustering

The next step is to search for clusters of calorimeter cells. A simple cone algorithm is used in this study and is described here. Firstly, calorimeter cells with an energy greater than 1.5 GeV are located for use as cluster initiator cells. The initiator cell with the highest energy is considered first. The total energy is found in all cells within a cone with half-angle $\Delta R = \sqrt{\Delta\eta^2 + \Delta\phi^2} = 0.4$ of the initiator cell. If this energy is greater than 10 GeV then the cells in the cone are identified as a cluster. The same procedure is then applied to the initiator cell with the next highest energy and not already included in a cluster. The treatment of overlapping cones is discussed in the next paragraph. The algorithm is repeated until all initiator cells have been considered. The position of a cluster is the energy weighted barycentre of the constituent cells.

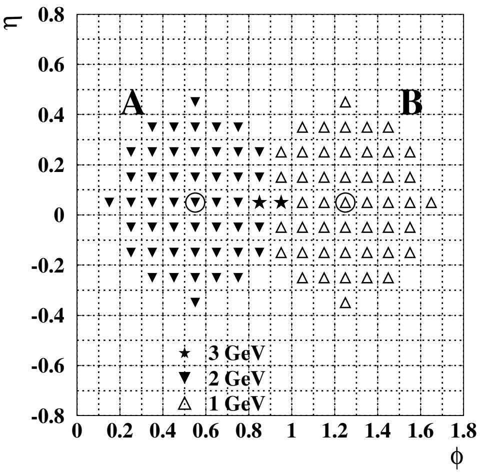

Figure 5.3: A simple simulation of the energy deposited in calorimeter cells by two overlapping jets.

In ATLFAST, it is possible to use the cone algorithm with and without energy sharing between overlapping clusters. The two algorithms are best explained using a diagram. Figure 5.3 shows the energy in $\Delta\eta \times \Delta\phi = 0.1 \times 0.1$ calorimeter cells for two hypothetical overlapping jets. Jet A and Jet B have energies of $E_A^{(T)} = 98$ GeV and $E_B^{(T)}$ =49 GeV and azimuthal angles $\phi_A^{(T)} = 0.5$ and $\phi_B^{(T)} = 1.2$. Assuming $\eta_A^{(T)} = \eta_B^{(T)} = 0$, the invariant mass of the two jets is $m_{inv}^{(T)} = \sqrt{2E_A^{(T)}E_B^{(T)}(1 - \cos(\phi_A^{(T)} - \phi_B^{(T)}))} = 47.52$ GeV. For simplicity, the jet energy is spread uniformly throughout a cone of half-angle $\Delta R = 0.4$. In real jets, the energy distribution is peaked at the jet centre and only ~90% of a hadronic shower is within $\Delta R = 0.4$ [84]. It is assumed that ATLFAST identifies the jet centre (marked with a circle) as the cluster initiator cell. The two cells with an energy of 3 GeV have contributions from both jets and are referred to here as shared cells.

Method	E_a	E_b	$\Delta\phi$	m_{inv}
Correct energy sharing	98	49	0.700	47.52
No energy sharing	100	47	0.708	47.53
Energy sharing	98.1	48.9	0.708	48.02

Table 5.2: A comparison of the cone algorithm with and without energy sharing between overlapping clusters. The first row lists the true parameters of the jets. See the text for more details of the study.

The first step in the cone algorithms with and without energy sharing is the same. The initiator cell of cluster A has the highest energy and is considered first. The shared cells are associated with cluster A which therefore has an energy of 100 GeV. The cells not already used and within $\Delta R = 0.4$ of the initiator cell of jet B have a total energy of 47 GeV. The azimuthal angle of a cluster is given by:

$$\phi = \frac{\sum_i E_i \phi_i}{E} \tag{5.3}$$

where E_i and ϕ_i are the energy and azimuthal angle of an individual calorimeter cell and E is the total cluster energy. Associating the same cells with the cluster as in the energy calculation, the azimuthal angles of the clusters are $\phi_A = 0.507$ and $\phi_A = 1.215$. The two clusters have an invariant mass of $m_{inv} = 47.53$ GeV.

If the energy sharing option of ATLFAST is used, the energy of the clusters is then recalibrated. The energy in shared cells is divided between the two clusters in the ratio of their total energies as found without energy sharing. The position of the cluster, however, is not recalibrated. In the example, the recalibrated cluster energies are $E_A = 98.08$ GeV and $E_B = 48.91$ GeV. The invariant mass of the two clusters is then $m_{inv} = 48.02$ GeV.

The results of the two approaches are summarised in table 5.2. When energy sharing is used, the cluster energies are nearer the jet energies than without. The error in the invariant mass, however, is larger with energy sharing. This effect was found to be more pronounced when there is more overlap between cones. A similar increase in the invariant mass of three overlapping clusters was found.

In this study, the invariant mass of three jets is used. The jets are often close together and energy sharing between clusters is not used. This choice is fairly academic anyway since precision mass measurements would not be performed using a simple cone algorithm. The use of clustering algorithms is discussed in more detail at the end of this chapter.

Isolated leptons

Once ATLFAST has identified clusters, the list of generated particles is searched for photons, muons and electrons within the pseudorapidity range of the Inner Detector ($|\eta| < 2.5$) and with transverse momentum greater than approximately 5 GeV. The four-momentum of isolated muons, photons and electrons is smeared according to an energy, luminosity and particle dependent function determined by full simulation [85]. Low luminosity ($L = 10^{33}$ cm^{-2} s^{-1}) parameterisations have been used throughout this analysis. The calorimeter clusters of electrons and photons are identified by comparing cluster positions with the smeared coordinates of the generated particle. A photon, electron or muon is labelled as isolated if:

- The separation in (η,ϕ) between the smeared coordinates of the particle and the nearest cluster not associated with the particle is greater than $\Delta R = 0.4$.

- The total energy in calorimeter cells within $\Delta R = 0.2$ of the particle is less than 10 GeV greater than the smeared transverse momentum of the generated particle.

Jets and jet flavour tagging

The calorimeter clusters not associated with isolated photons, electrons or muons and with an energy greater than 10 GeV are labelled as jets. The jet energies are smeared according to an energy and luminosity dependent function. A jet is initially labelled as a b-jet or c-jet if it is within $\Delta R < 0.2$ of a generated b-quark or c-quark with $p_T > 5$ GeV and $|\eta| < 2.5$.

b-tagging efficiency	Rejection factor	
ϵ_b(%)	u,d,s,g jets (r_q)	c jets (r_c)
33	1400±400	22.9±2.0
43	220±30	10.8±0.6
53	91±7	6.7±0.3
64	32±2	4.2±0.1

Table 5.3: b-tagging efficiencies and mis-tagging rejection factors implemented in ATL-FAST

In actual experiments, totally efficient b-tagging is unachievable and there is a finite chance of mis-tagging other flavour jets as b-jets. Table 5.3 lists four different b-tagging efficiencies and the corresponding mis-tagging rejection factors available in ATLFAST. These numbers were found using full Monte Carlo simulations in [29]. The rejection factors are, in fact, a function of the transverse momentum of the jet and the numbers shown are an average over all p_T (see [78]). ATLFAST simulates realistic b-tagging performance by only tagging ϵ_b of jets matched with a b-jet. $1/r_c$ and $1/r_q$ of jets matched with c-quarks and other flavour quarks respectively are mis-tagged as b-jets[a].

The missing transverse momentum of an event is calculated by ATLFAST using the energy and position of calorimeter clusters and cells.

A good agreement between full Monte Carlo simulations and ATLFAST has been demonstrated in $A/H \rightarrow \tau\tau$ and $h \rightarrow b\bar{b}$ decay channels [86].

[a]In reality, the rejection factor against mis-tagging gluon jets is worse than for light quark jets because the decays of a gluon into $b\bar{b}$ and $c\bar{c}$ have finite branching ratios of 4% and 6% respectively.

5.4 A brief literature survey

Some work has already been done on the discovery potential of R-parity violating SUSY at the LHC. In [87], it is assumed that RPC SUSY will be searched for first. The paper therefore investigates the possibility of extracting an implicit RPV signature from cuts designed to detect RPC SUSY. It is found that after one year of running the LHC will be able to detect spartons from RPV SUSY with masses of up to 1 TeV.

The implications of a non-zero λ coupling (see equation 5.2) is explored in [77]. Again, it is found that a signal of RPV mSUGRA would be visible over a large region of parameter space. If the LSP decays into only electrons and muons, precision measurements of the free parameters of the model can be made.

The consequences of a non-zero λ'' coupling are investigated in [88] using the FORCE datacard of ISAJET. The study focuses on mSUGRA point 5 but also briefly considers the other LHC mSUGRA points. At point 5, it is shown that an inclusive signature can be used to detect the presence of new physics. Some explicit signatures are also investigated and the following mass measurements are made:

- LSP mass, $m(\tilde{\chi}_1^0) = 122 \pm 3.1(\mathrm{stat}) \pm 1.3(\mathrm{syst})$ GeV
- Light right-slepton mass, $m(\tilde{l}_R) = 157 \pm 5.1(\mathrm{stat}) \pm 1.6(\mathrm{syst})$ GeV
- $\tilde{\chi}_2^0$ mass, $m(\tilde{\chi}_2^0) = 233 \pm 4.1(\mathrm{stat}) \pm 2.3(\mathrm{syst})$ GeV
- Light left-squark mass, $m(\tilde{q}_L) = 664 \pm 30(\mathrm{stat}) \pm 7(\mathrm{syst})$ GeV

Very tight kinematic cuts are used in this analysis and the width of the obtained $\tilde{\chi}_1^0$ mass peak is largely defined by the cuts. The cone and mulguisin [89] clustering algorithms are compared. Neither is found to be significantly better than the other for the analysis presented.

5.5 LHC mSUGRA point 5 with non-zero λ''_{212}

5.5.1 Motivations for choosing point 5 and non-zero λ''_{212}

This analysis is a more detailed study of one part of the work presented in [88]. The results in this chapter are therefore for mSUGRA point 5 (table 5.1). In RPC models, the stable $\tilde{\chi}_1^0$ is a good candidate for weakly interacting massive particles (WIMPs) which may form some of the dark matter in the universe. The parameters of point 5 were originally chosen to be consistent with cosmological density measurements [25] inferred from COBE observations [90]. Of course, with R-parity not conserved, this argument is no longer valid. Point 5 does, however, offer a variety of interesting SUSY signatures to study.

ijk	Jet flavour	λ''	ijk	Jet flavour	λ''
112	uds	10^{-6}	223	csb	1.25
113	udb	10^{-5}	312	tdc	0.43
123	usb	1.25	313	tdb	0.43
212	cds	1.25	323	tsb	0.43
213	cdb	1.25			

Table 5.4: Upper limits (2σ) on individual λ'' couplings [75].

Again for consistency with [88], the only non-zero RPV coupling in this analysis is λ''_{212}. The current limits on all λ'' couplings are shown in table 5.4. Only the λ''_{112} and λ''_{113} couplings are strongly constrained. In this analysis, a non-zero λ''_{212} allows the decay $\tilde{\chi}_1^0 \rightarrow cds$ (figure 5.4). The invariant mass of the jets from the c, d and s-quarks provide a measure of the $\tilde{\chi}_1^0$ mass. Except where jet-flavour tagging is used, the $\tilde{\chi}_1^0$ mass reconstruction in scenarios with non-zero λ''_{123}, λ''_{213}, λ''_{223}, λ''_{112} and λ''_{113} will be similar. The use of b-tagging is investigated in this analysis but is found to offer little advantage. The methods presented here can, therefore, be equally applied to scenarios with a different non-zero λ''.

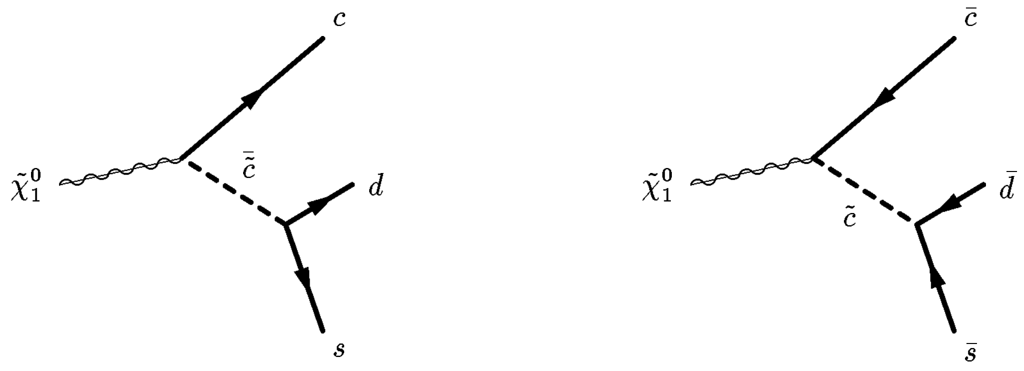

Figure 5.4: The R-parity violating decays of the LSP for $\lambda_{212} \neq 0$.

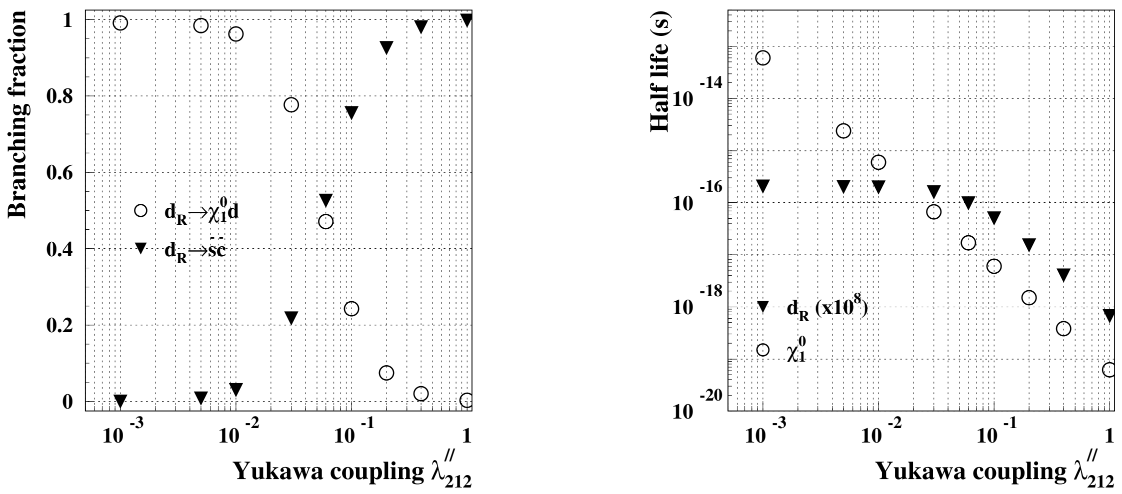

(a) **(b)**

Figure 5.5: **(a)** Branching fraction of RPC and RPV decays of $\tilde{d}_R$ plotted against λ''_{212}. **(b)** The lifetime of the $\tilde{\chi}_1^0$ and $\tilde{d}_R$ plotted against λ''_{212}.

In [88], ISAJET 7.31 was used as the event generator. R-parity violating vertices are not implemented in ISAJET 7.31 but it is possible to force the decay of a stable particle. To simulate a small but non-zero λ''_{212}, the $\tilde{\chi}_1^0$ was forced to decay into cds or $\bar{c}\bar{d}\bar{s}$. The version of HERWIG used for the analysis presented here is only valid for small λ''. For this reason, and to be compatible with previous work, a value of 0.005 was chosen for λ''_{212}.

The choice of $\lambda''_{212} = 0.005$ is supported by figures 5.5a-b. In figure 5.5a, the branching fraction of the RPC decay $\tilde{d}_R \to \tilde{\chi}_1^0 d$ and the RPV decay $\tilde{d}_R \to \bar{c}\bar{s}$ are plotted against λ''_{212}. At $\lambda''_{212} = 0.005$, the $\tilde{d}_R$ decay is dominated by the RPC channel. This value of the coupling is therefore within the limits of the version of HERWIG used. In figure 5.5b, the lifetime of the $\tilde{\chi}_1^0$ and $\tilde{d}_R$ are plotted against λ''_{212}. At $\lambda''_{212} = 0.005$, the $\tilde{\chi}_1^0$ has a lifetime of 2.4×10^{-15} s and thus decays in the beam pipe.

5.5.2 Characteristics of RPV point 5

Table 5.5 shows sparticle masses and principal decay modes for mSUGRA point 5 with $\lambda''_{212} = 0.005$. Squarks have masses of around 650 GeV and the gluino has a mass of 733 GeV. Sleptons are considerably lighter than spartons with a mass of approximately 200 GeV. The LSP is the $\tilde{\chi}_1^0$ with a mass of 121.5 GeV. The lightest Higgs in this scenario is the h^o. With a mass of 94.3 GeV it is just beyond the current Higgs lower mass limit of 79.6 GeV [12] and should be discovered by LEP 2 [91].

SUSY production cross sections for this point are listed in table 5.6. The total SUSY production cross section at point 5 was found to be 21.89 pb using HERWIG 6.02. Sparton production is seen to dominate in this mSUGRA model.

Figure 5.6 illustrates the dominant sparton decay chains of mSUGRA point 5. The $\tilde{q}_L$ decay chain studied in this analysis is shown in figure 5.6a. Two opposite sign, same family (OSSF) fermions are produced, the invariant mass distribution of which has a sharp upper edge at $m_{ll}^{(max)} = 109.1$ GeV. The $\tilde{\chi}_1^0$, right-slepton and $\tilde{\chi}_2^0$ masses are related to $m_{ll}^{(max)}$ by (Appendix A):

$$m_{ll}^{(\max)} = m_{\tilde{\chi}_2^0} \sqrt{1 - \frac{m_{\tilde{l}_R}^2}{m_{\tilde{\chi}_2^0}^2}} \sqrt{1 - \frac{m_{\tilde{\chi}_1^0}^2}{m_{\tilde{l}_R}^2}} \tag{5.4}$$

Parent	Mass (Gev)	Decay products	b.f.
$\tilde{u}_L(\tilde{c}_L)$	654.1	$\tilde{\chi}_1^+ d(s)$	0.653
		$\tilde{\chi}_2^0 u(c)$	0.330
$\tilde{d}_L(\tilde{s}_L)$	657.2	$\tilde{\chi}_1^- u(d)$	0.642
		$\tilde{\chi}_2^0 d(u)$	0.314
$\tilde{b}_1$	600.3	$\tilde{\chi}_1^- t$	0.414
		$\tilde{\chi}_2^0 b$	0.284
		$\tilde{t}_1 \mathrm{W}^-$	0.274
$\tilde{t}_1$	459.6	$\tilde{\chi}_1^+ b$	0.643
		$\tilde{\chi}_1^0 t$	0.231
		$\tilde{\chi}_2^0 t$	0.126
$\tilde{u}_R$	631.0	$\tilde{\chi}_1^0 u$	0.991
$\tilde{d}_R(\tilde{s}_R)$	628.4	$\tilde{\chi}_1^0 d(s)$	0.984
		$\bar{c}\ \bar{s}(\bar{d})$	0.008
$\tilde{c}_R$	631.0	$\tilde{\chi}_1^0 c$	0.989
		$\bar{s}\ \bar{d}$	0.002
$\tilde{b}_2$	628.8	$\tilde{\chi}_1^0 b$	0.675
		$\tilde{t}_1 \mathrm{W}^-$	0.150
$\tilde{t}_2$	670.7	$\tilde{t}_1 \mathrm{Z}^0/\gamma^*$	0.340
		$\tilde{\chi}_1^+ b$	0.265
h^0	94.3	$b\ \bar{b}$	0.882
H^0	611.7	$t\ \bar{t}$	0.946
A^0	606.8	$t\ \bar{t}$	0.921
H^+	612.2	$t\ \bar{b}$	0.968

Parent	Mass (Gev)	Decay products	b.f.
$\tilde{g}$	732.9	$\tilde{b}_1\bar{b}$, $\tilde{t}_1\bar{t}$ +c.c.	0.075
		$\tilde{d}_R\bar{d}$, $\tilde{s}_R\bar{s}$ +c.c.	0.049
		$\tilde{b}_2\bar{b}$ +c.c.	0.48
		$\tilde{u}_R\bar{u}$, $\tilde{c}_R\bar{c}$ +c.c.	0.047
		$\tilde{u}_L\bar{u}$, $\tilde{c}_L\bar{c}$ +c.c.	0.029
		$\tilde{d}_L\bar{d}$, $\tilde{s}_L\bar{s}$ +c.c.	0.027
$\tilde{e}_L^\pm(\tilde{\mu}_L^\pm)$	238.8	$\tilde{\chi}_1^0 \mathrm{e}^\pm(\mu^\pm)$	0.940
		$\tilde{\chi}_1^\pm \nu_e(\nu_\mu)$	0.042
$\tilde{\tau}_1^\pm$	156.8	$\tilde{\chi}_1^0 \tau^\pm$	1.000
$\tilde{\nu}_e(\tilde{\nu}_\mu)$	238.8	$\tilde{\chi}_1^0 \nu_e(\nu_\mu)$	1.000
$\tilde{e}_R^\pm(\tilde{\mu}_R^\pm)$	157.2	$\tilde{\chi}_1^0 \mathrm{e}^\pm(\mu^\pm)$	1.000
$\tilde{\tau}_2^\pm$	238.9	$\tilde{\chi}_1^0 \tau^\pm$	0.939
$\tilde{\chi}_1^0$	121.5	$\bar{c}\ \bar{d}$	0.5
		$c\ d$	0.5
$\tilde{\chi}_2^0$	233.0	$\tilde{\chi}_1^0 h^0$	0.646
		$\tilde{\tau}_1^\pm \tau^\mp$+c.c.	0.060
		$\tilde{e}_R^\pm \mathrm{e}^\mp$, $\tilde{\mu}_R^\pm \mu^\mp$ + c.c.	0.046
$\tilde{\chi}_1^\pm$	232.0	$\tilde{\chi}_1^0 \mathrm{W}^\pm$	0.897
		$\tilde{\tau}_1^\pm \nu_\tau$	0.066
$\tilde{\chi}_2^\pm$	520.1	$\tilde{\chi}_2^0 \mathrm{W}^\pm$	0.292
		$\tilde{\chi}_1^\pm \mathrm{Z}^0/\gamma^*$	0.258
		$\tilde{\chi}_1^\pm h^0$	0.202

Table 5.5: Sparticle masses and their principal branching fractions (b.f.) at mSUGRA point 5 with the R-parity violating coupling, $\lambda''_{212} = 0.005$. Several decay products listed on one line indicates that the branching ratio is the same for each decay i.e. $\Gamma_f(\tilde{g} \to \tilde{b}_1\bar{b}) = \Gamma_f(\tilde{g} \to \tilde{t}_1\bar{t}) = 0.075$. Charge conjugate has been abreviated as c.c.

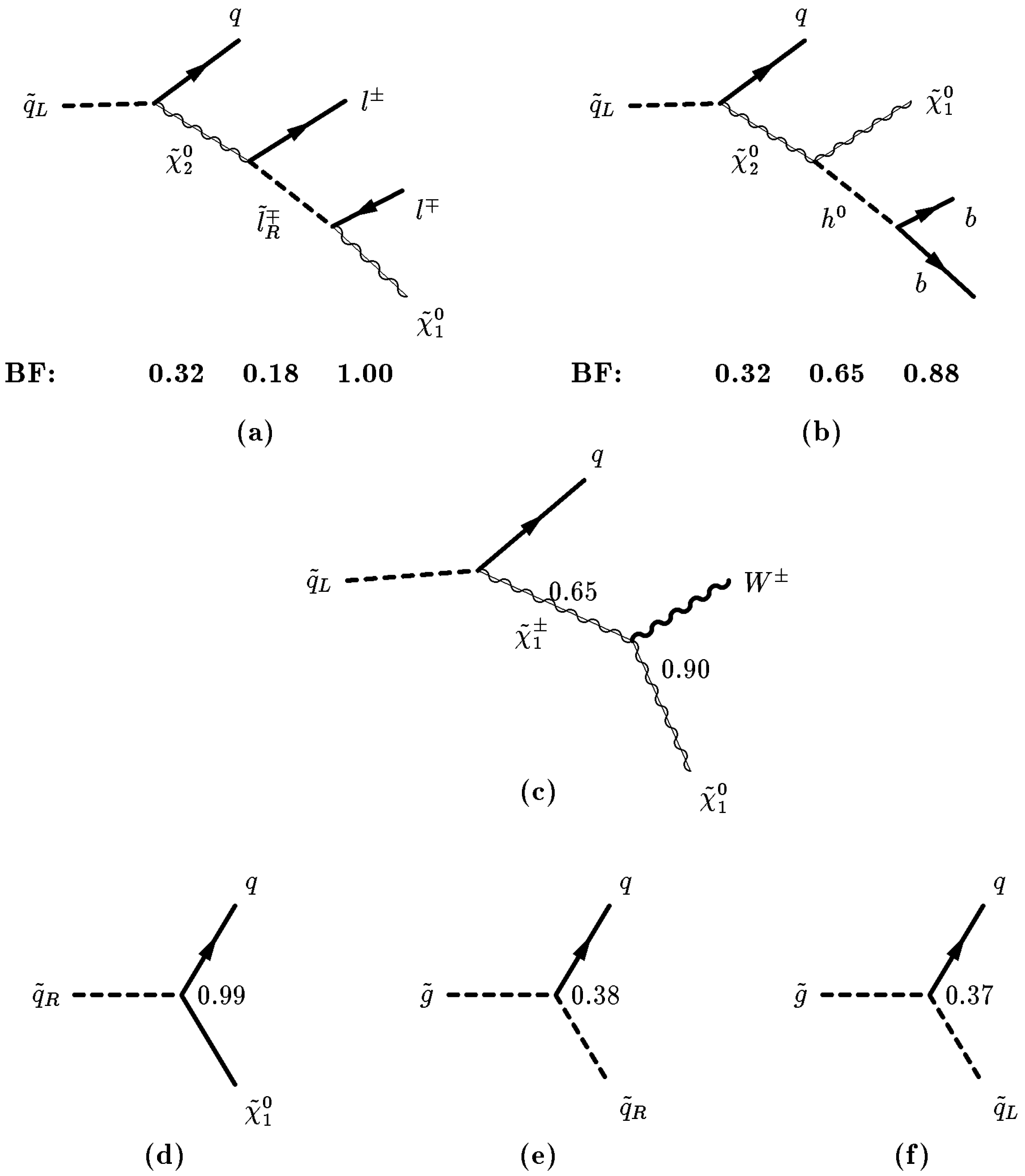

Figure 5.6: Important sparton decay chains at mSUGRA point 5. The RPV decay of the $\tilde{\chi}_1^0$ into c, d and s-quarks is not shown. The branching fractions for the vertices of each diagram are shown below (a-b) or in the angle of the vertices (c-f). These branching fractions are for $q = u, d, s, c, b$ and $l = e, \mu$ in (a), (b) and (f) and $q = u, d, s, c$ in (c), (e) and (d). The combined branching fractions of the decay chains are (a) 0.059 (b) 0.183 (c) 0.588.

Production products	Production cross section		Events in 3 years
	Fractional	(pb)	
$\tilde{q}_R\tilde{q}_R$	0.111 ± 0.001	2.43	77760
$\tilde{q}_L\tilde{q}_L$	0.132 ± 0.001	2.89	92480
$\tilde{q}_R\tilde{q}_L$	0.064 ± 0.001	1.40	44800
$\tilde{q}_R\tilde{g}$	0.232 ± 0.001	5.08	162560
$\tilde{q}_L\tilde{g}$	0.213 ± 0.001	4.66	149120
$\tilde{g}\tilde{g}$	0.097 ± 0.001	2.12	67840
$\tilde{l}\,\tilde{l}$	0.005 ± 0.000	0.11	3520
$\tilde{\chi}^{\pm}_{1,2}$, $\tilde{\chi}^{0}_{1,2,3,4}$	0.146 ± 0.001	3.20	102400
Total	1.0	21.89	$\sim 700 \times 10^3$

Table 5.6: SUSY production cross sections at mSUGRA point 5. The fractional cross sections were found using HERWIG 6.0. The absolute cross sections have been normalised to give a total SUSY production cross section of 21.89 pb, as found using HERWIG 6.02. The right-most column of the table lists the number of events expected after three years of low luminosity running ($\int dt\, L = 3.2 \times 10^4$ pb^{-1}).

In the RPC scenario, the $\tilde{\chi}^0_1$ leaves the detector without interacting and its mass can not be measured directly. Equation 5.4 and other variables sensitive to SUSY parameters must be combined to find $m_{\tilde{\chi}^0_1}$, $m_{\tilde{\chi}^0_2}$ and $m_{\tilde{l}_R}$ [25]. In the RPV scenario of this analysis, the $\tilde{\chi}^0_1$ mass can be measured directly. In principle, the $\tilde{l}_R$, $\tilde{\chi}^0_2$ and $\tilde{q}_L$ masses can then be found since all SM products of the decay chain can be detected.

The three-body decay $\tilde{\chi}^0_2 \to \tilde{\chi}^0_1 l^+ l^-$ has the same final state particle content as the $\tilde{\chi}^0_2$ decay in figure 5.6a. In this case, the edge of the OSSF lepton pair invariant mass distribution $m_{ll}^{(\mathrm{max})} = m_{\tilde{\chi}^0_2} - m_{\tilde{\chi}^0_1}$. At point 5, $\Gamma(\tilde{\chi}^0_2 \to \tilde{l}^{\pm} l^{\mp})/\Gamma(\tilde{\chi}^0_2 \to \tilde{\chi}^0_1 l^+ l^-) = 46$ and this decay is not a significant background.

If R-parity is conserved, the $\tilde{\chi}^0_2 \to \tilde{\chi}^0_1 h^o \to \tilde{\chi}^0_1 b\bar{b}$ decay (figure 5.6b) can be used to find the mass of the h^o [25]. After three years of running, a clear peak in the $b\bar{b}$ invariant mass is seen. In baryon number violating scenarios, the signal peak is difficult, or impossible, to extract because of the increased jet multiplicity [88]. For most non-zero λ'', at least one b-quark or c-quark is produced in the $\tilde{\chi}^0_1$ decay. The increased number of b-jets and mis-tagged c-jets introduces a large combinatorial background.

The left-handed squarks that do not decay into $\tilde{\chi}_2^0 q$ mostly decay via $\tilde{q}_L \to \tilde{\chi}_1^{\pm} q \to \tilde{\chi}_1^0 W^{\pm} q$ (figure 5.6c). This decay chain is less useful for finding model parameters. When the W decays hadronically (bf=67.9% [39]) the two jets are difficult to separate from at least eight other jets. In the case of the W decaying leptonically, the production of a neutrino prevents the determination of the W momentum.

Right handed squarks nearly always decay into $\tilde{\chi}_1^0 q$ (figure 5.6d). Gluinos decay into $\tilde{q}_R q$ and $\tilde{q}_L q$ with approximately equal probability (figures 5.6e-f).

5.6 Measuring the $\tilde{\chi}_1^0$ mass at RPV point 5

5.6.1 Introduction

In the RPV model of this analysis, the $\tilde{\chi}_1^0$ decays into three quarks. This section develops an algorithm to identify the jets from these quarks and find their invariant mass, thus measuring the $\tilde{\chi}_1^0$ mass. In this algorithm, a number of cuts are made on the data to reduce backgrounds from SUSY and SM processes. Three measures of the effectiveness of a set of cuts are presented in section 5.6.2. These are used in subsequent sections to optimise the algorithm.

In the RPV scenario being studied, two $\tilde{\chi}_1^0$s are produced in nearly all events. The $\tilde{\chi}_1^0$ with the highest transverse momentum is referred to as the hard $\tilde{\chi}_1^0$ and the other the soft $\tilde{\chi}_1^0$. The mean transverse momenta of the hard and soft $\tilde{\chi}_1^0$s from all SUSY production processes were measured at the generator level to be 292 GeV and 157 GeV.

5.6.2 Effectiveness of cuts

The effectiveness of the algorithm used to separate the $\tilde{\chi}_1^0$ mass peak from backgrounds is quantified by three variables: the precision of the mass measurement, the bias of the mass peak and the reconstruction efficiency.

The precision of the mass measurement is defined to be the error on the mean of a Gaussian fitted to the data. The reconstructed mass distribution has a shoulder at around 150 GeV and so the Gaussian fit is performed over the range $0 < m_{jjj} < 140$ GeV.

The bias of the mass peak is defined as $b_m = m_{jjj} - m_{\tilde{\chi}_1^0}$ where m_{jjj} is the reconstructed $\tilde{\chi}_1^0$ mass and $m_{\tilde{\chi}_1^0}$ is the true $\tilde{\chi}_1^0$ mass (121.5 GeV at point 5).

Two reconstruction efficiencies will be used in this chapter. The reconstruction efficiency ϵ_1 is the fraction of generated events in which one well matched $\tilde{\chi}_1^0$ is reconstructed. The reconstruction efficiency ϵ_2 is the fraction of generated events in which two well matched $\tilde{\chi}_1^0$s are reconstructed. Two $\tilde{\chi}_1^0$s are generated in nearly all events. A reconstructed $\tilde{\chi}_1^0$ is defined to be well matched if the spatial separation between it and the HERWIG generated $\tilde{\chi}_1^0$ is small. The separation between a reconstructed $\tilde{\chi}_1^0$ at $(\eta_{recon}, \phi_{recon})$ and the generated $\tilde{\chi}_1^0$ at $(\eta_{parton}, \phi_{parton})$ is measured using:

$$\Delta R_{mat} = \sqrt{(\phi_{parton} - \phi_{recon})^2 + (\eta_{parton} - \eta_{recon})^2} \tag{5.5}$$

To determine what constitutes a well matched $\tilde{\chi}_1^0$, the $\tilde{\chi}_1^0$ mass peak was found, using the algorithm presented later in this chapter, with different upper limits on ΔR_{mat}. As the combinatorial background is removed by requiring better matching, the $\tilde{\chi}_1^0$ mass peak width approaches a minimum due to jet measurement errors alone. The width of the

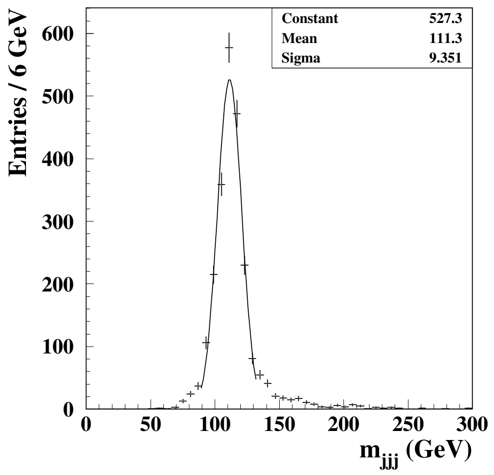

Figure 5.7: The mass distribution of reconstructed $\tilde{\chi}_1^0$s well matched spatially to the HERWIG generated sparticle. The jet combinations used to generate the plot were selected using the "Jet cuts" ($n_{jet}^{(max)} = 10$) presented in section 5.6.4 and the ΔR_{mat} cuts described in the text. Simulated data for three years of running were used. There are 2080 events in the peak.

hard $\tilde{\chi}_1^0$ mass peak reaches a plateau value of approximately 10.0 GeV at $\Delta R_{mat}^{(a)} < 0.03$. The soft $\tilde{\chi}_1^0$ mass peak width is at a minimum below $\Delta R_{mat}^{(b)} < 0.05$. The hard and soft $\tilde{\chi}_1^0$s are therefore defined to be well matched if $\Delta R_{mat} < 0.03$ and $\Delta R_{mat} < 0.05$ respectively.

The mass peak for well matched $\tilde{\chi}_1^0$s (both hard and soft) is plotted in figure 5.7. Not all energy deposited by softer jets is within a cone of width $\Delta R = 0.4$. For this reason, the centre of the matched $\tilde{\chi}_1^0$ mass peak is 8% lower than the true mass of 121.5 GeV. This plot indicates that the bias of a mass peak in which there is minimal background should be $b_m \approx -10$ GeV.

5.6.3 The data sample

A data sample of 7×10^5 simulated SUSY events is used to determine sparticle masses. This data set corresponds to three years of low luminosity running ($L = 10^{33}$ cm^{-2} s^{-1}, $\int dtL = 3.2 \times 10^4$ pb^{-1}). The ratios in which different SUSY particles are generated were given in table 5.6. The SUSY data sample does not include any events in which only SM particles are produced.

5.6.4 Cuts against SUSY backgrounds

The cuts used to extract a $\tilde{\chi}_1^0$ mass peak from SUSY events can be classified as jet, lepton or b-tagging cuts.

Jet cuts

The principal difficulty in measuring the $\tilde{\chi}_1^0$ mass is identifying jets from the $\tilde{\chi}_1^0$ decay. It is instructive to consider the jet multiplicity in events.

Figures 5.8a and 5.8b show the jet multiplicity distribution of all SUSY events and for $\tilde{q}_R\tilde{q}_R$, $\tilde{q}_L\tilde{q}_L$ and $\tilde{q}_R\tilde{q}_L$ production. Nearly all right-squarks decay via $\tilde{q}_R \to \tilde{\chi}_1^0 q \to qqqq$ and one might therefore expect a mean multiplicity of 8 jets for $\tilde{q}_R\tilde{q}_R$ production. Gluon radiation by quarks, however, raises the mean multiplicity to 10.5 jets. The three jets from harder $\tilde{\chi}_1^0$s are spatially close together and some merging of jets occurs resulting in a small number of events with fewer than 8 jets (6% for all SUSY production). In $\tilde{q}_R\tilde{q}_R$ events, the $\tilde{\chi}_1^0$s are produced directly in the right-squark decay and have a higher mean transverse momentum than $\tilde{\chi}_1^0$s from longer decay chains (376 GeV for the hard $\tilde{\chi}_1^0$). As a consequence, there is more jet merging and there are more events with less than 8 jets (14%). Gluinos (not shown in figure) mostly decay into a squark and a quark and $\tilde{g}\tilde{g}$

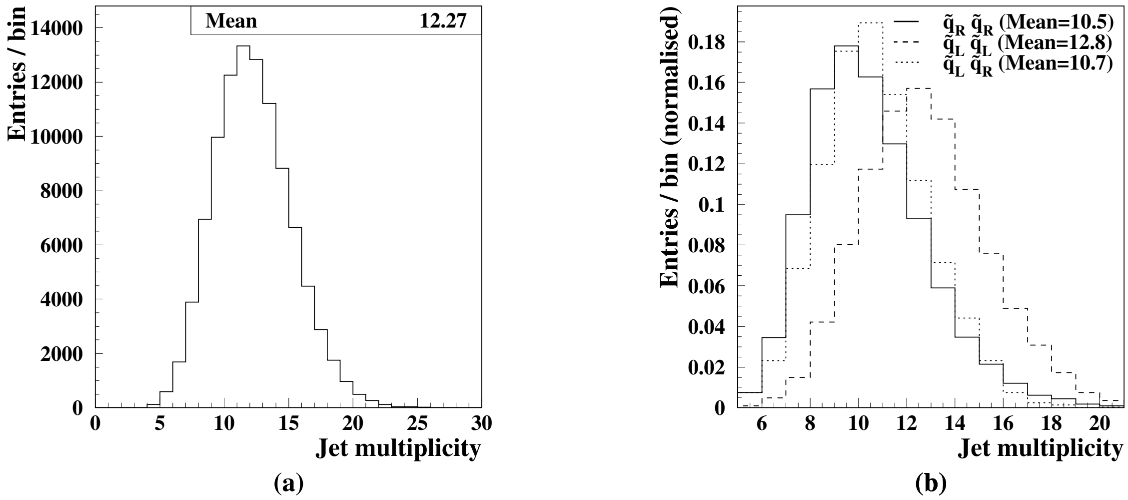

Figure 5.8: The jet multiplicity in events at mSUGRA point 5. Distributions are shown for **(a)** all SUSY production and **(b)** $\tilde{q}_R\tilde{q}_R$, $\tilde{q}_R\tilde{q}_L$ and $\tilde{q}_L\tilde{q}_L$ production.

events have a higher mean jet multiplicity of 13.6.

When λ''_{212} is small, there are nearly always two $\tilde{\chi}^0_1$s produced in an event and one can therefore search for two sets of three jets with similar invariant mass. An upper limit on the invariant mass difference of $\delta m_{jjj} = |m^{(a)}_{jjj} - m^{(b)}_{jjj}| < 20$ GeV is used in this analysis. This value was chosen to be approximately twice the width of the matched $\tilde{\chi}^0_1$ mass peak in figure 5.7. This criterion alone does not sufficiently reduce the combinatorial background: In an event with 11 jets there are 9240 ways of choosing two sets of three jets.

One way to reduce the combinatorial background is to only use events with a certain number of jets. The lower bound in this analysis, $n^{(min)}_{jet}$, is 8: the minimum number of quarks produced in a $\tilde{q}_R\tilde{q}_L$, $\tilde{q}_L\tilde{q}_L$ or $\tilde{q}_R\tilde{q}_R$ event. The upper limit, $n^{(max)}_{jet}$, should be high enough to allow some gluon radiation but low enough to keep the combinatorial background small. It is studied in more detail later in this section.

To further restrict the number of jet combinations considered, cuts are placed on the

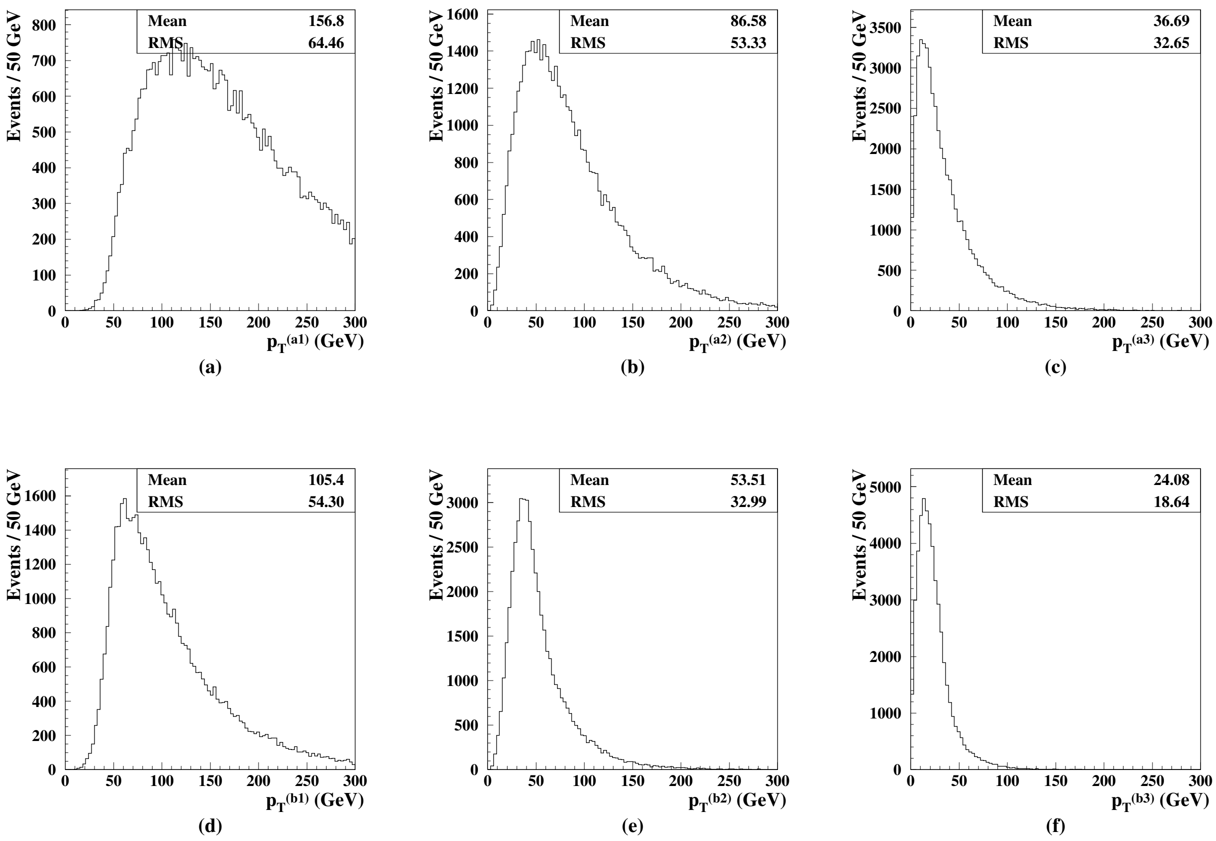

Figure 5.9: Histograms **(a)**, **(b)** and **(c)** show the transverse momenta of the hardest, middle and softest quarks respectively from the hard $\tilde{\chi}_1^0$ decay. Histograms **(d-f)** show the same but for the soft $\tilde{\chi}_1^0$. The transverse momenta were measured at the generator level.

jet kinematics. Figure 5.9 shows the transverse momenta of the HERWIG generated quarks from the hard $(p_T^{(a1)}, p_T^{(a2)}, p_T^{(a3)})$ and the soft $(p_T^{(b1)}, p_T^{(b2)}, p_T^{(b3)})$ $\tilde{\chi}_1^0$. The softest jet of the soft $\tilde{\chi}_1^0$ has a mean transverse momentum of only 24 GeV and so it is necessary to consider both high and low energy jets. The following transverse momentum cuts are used in this analysis (all p_T in GeV):

- $100 < p_T^{(a1)}$; $17.5 < p_T^{(a2)} < 300$; $15.0 < p_T^{(a3)} < 150$
- $17.5 < p_T^{(b1)} < 300$; $17.5 < p_T^{(b2)} < 150$; $15.0 < p_T^{(b3)} < 75$

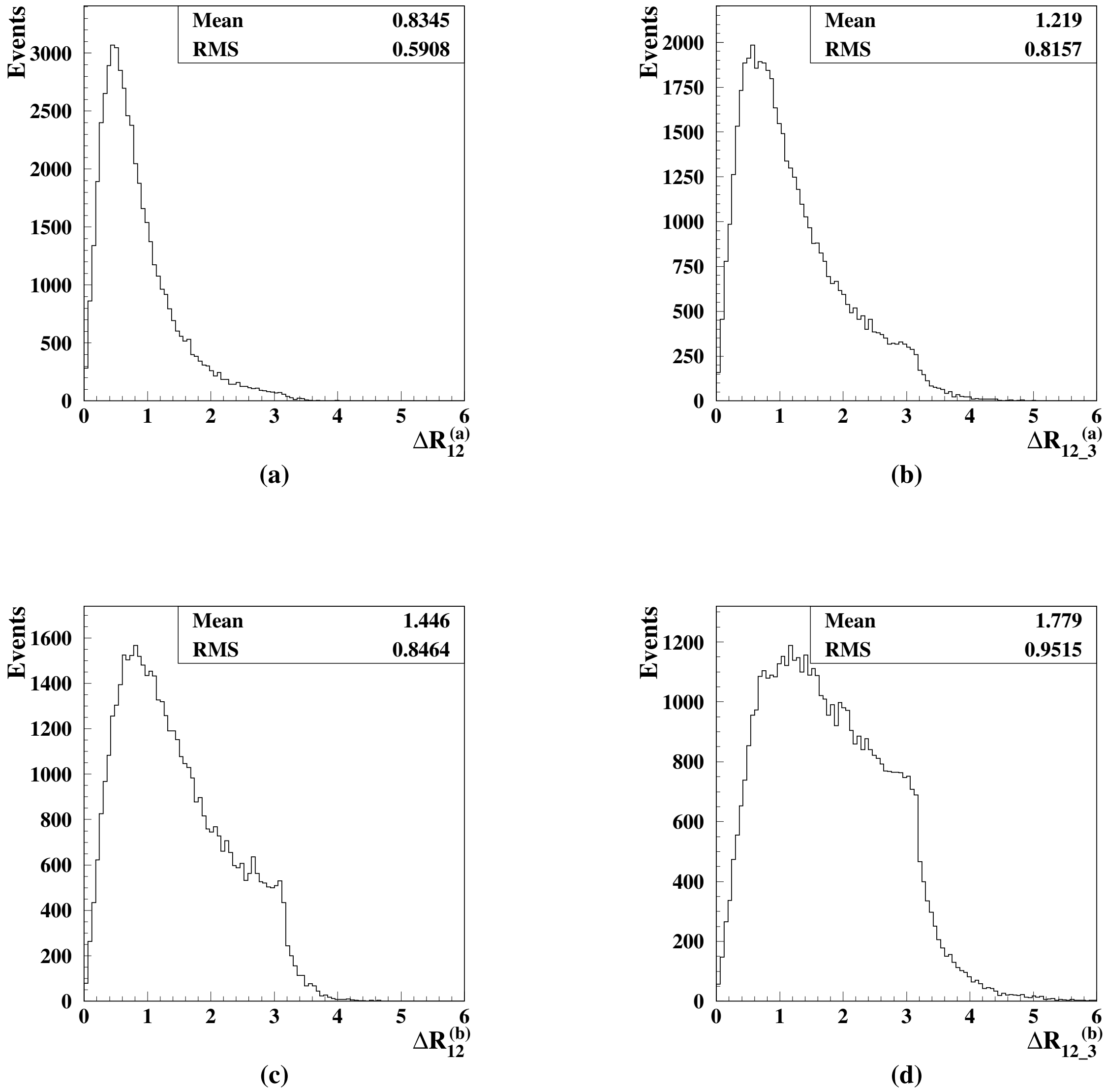

Figure 5.10: The distribution of the separation in (η, ϕ) of: **(a)** the two hardest quarks from the hard $\tilde{\chi}_1^0$ decay; **(b)** The combined momenta of the two hardest quarks and the softest quark from the hard $\tilde{\chi}_1^0$ decay. Histograms **(c)** and **(d)** show the same distributions for the soft $\tilde{\chi}_1^0$ quarks. The separation in ϕ of two quarks is taken to be the smallest of the two possible angles. This results in the observed discontinuities in the histograms at around $dr = \pi$.

Candidate sets of jets from the $\tilde{\chi}_1^0$ decay can also be identified by their spatial separation. Figure 5.10 shows, for both $\tilde{\chi}_1^0$s, the angle between the hardest and next hardest quarks (ΔR_{12}) and between the combined momentum vector of the two hardest quarks and the softest quark (ΔR_{12-3}). The following cuts were chosen based on figure 5.10:

- $\Delta R_{12}^{(a)} < 1.3$; $\Delta R_{12-3}^{(a)} < 1.3$
- $\Delta R_{12}^{(b)} < 2.0$

When applying kinematic cuts similar to the above, it is important to ensure that the cuts themselves are not defining the sought mass peak. It is shown later that the mass distribution of background events passing these cuts is significantly wider than the $\tilde{\chi}_1^0$ mass peak.

A hard quark is produced in the decay of a $\tilde{q}_R$, $\tilde{q}_L$ or $\tilde{g}$. In sparton-sparton events, two such hard quarks ($q^{(h1)}$, $q^{(h2)}$) are produced. When measured at the generator level, approximately 75% of such events have $p_T^{(h1)} > 200$ GeV and $p_T^{(h2)} > 100$ GeV. Over 80% of the hard quarks are within $|\eta| < 2$. By requiring that two jets in an event satisfy these cuts, the number of remaining jets from which the $\tilde{\chi}_1^0$s can be reconstructed is reduced, thus reducing the combinatorial background.

Using only cuts on the jet kinematics and jet multiplicity, a mass peak can be seen above the background from wrong combinations of jets. Figure 5.11a shows the mass peak obtained after three years of low luminosity running. The SUSY data sample used to obtain this plot was defined in section 5.6.3.

For each combination of jets passing the kinematic cuts, the reconstructed masses of both the hard and the soft $\tilde{\chi}_1^0$s are included in figure 5.11a. If two or more combinations of jets from one event pass the cuts, the masses from each combination are plotted with unity weight. This method is adopted because there is no way of choosing the best combination. One might, for example, select the jet combination with smallest δm_{jjj}. This variable, however, has a maximum value of 20 GeV which is about the precision of a measurement of δm_{jjj} given that the mass peak width due to detector resolution is

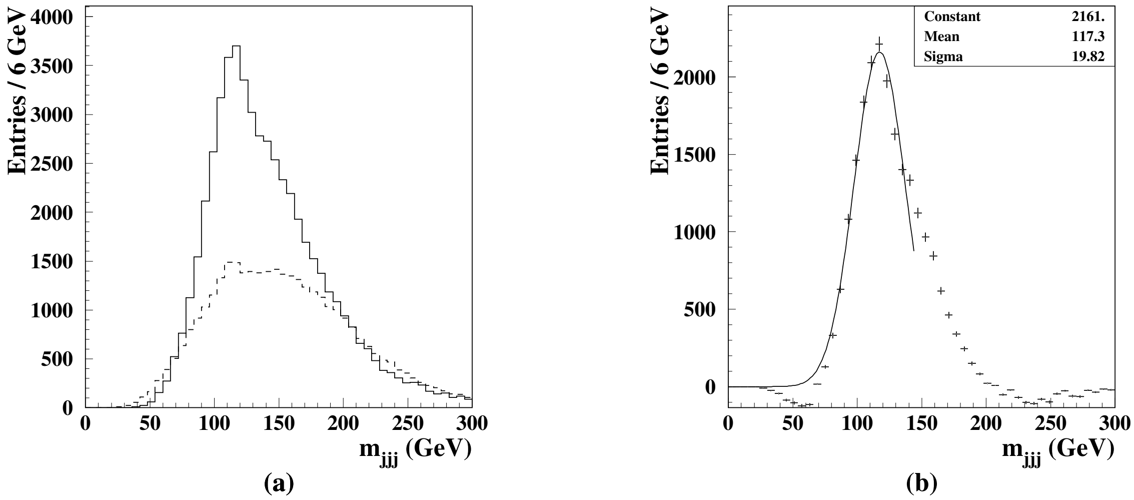

Figure 5.11: (**a**) The solid histogram shows the invariant mass distribution of the three-jet combinations passing the jet cuts described in the text ($n_{jet}^{(max)} = 10$). The dashed histogram shows the background distribution generated from the same data set of 700000 SUSY events (three years of low luminosity running). (**b**) shows the difference between the two histograms in (**a**).

10 GeV (see figure 5.7).

In events with more than one combination passing the cuts, two combinations of jets often differ only in the choice of jets for one of the two $\tilde{\chi}_1^0$s. For example, the jets identified as being from the hard $\tilde{\chi}_1^0$ may be the same in both combinations with the soft $\tilde{\chi}_1^0$ jets being different. In this case, the hard $\tilde{\chi}_1^0$ mass would be included in the histogram only once. The two soft $\tilde{\chi}_1^0$ masses would, however, be included with unity weight.

There is a broad combinatorial background beneath the $\tilde{\chi}_1^0$ mass peak, the shape of which is defined by the kinematic cuts and not by a physical process. A distribution of the same shape can therefore be generated from the same data as the $\tilde{\chi}_1^0$ peak by selecting 3-jet combinations that are not from a $\tilde{\chi}_1^0$ decay. It was found that the invariant mass distribution of 3-jet combinations with $20 < |\delta m_{jjj}| < 100$ GeV could be used as an approximation to the background. The shape of the tails of the generated background distribution is very similar to the shape of the $\tilde{\chi}_1^0$ mass peak tails. The generated background distribution, however, has fewer events in the central peak.

A generated and normalised background is superimposed on figure 5.11a. The generated distribution is normalised to the background under the $\tilde{\chi}_1^0$ peak using events in the distribution tails which are defined:

- $(\bar{m}_{jjj} - 3\sigma) < m_{jjj} < (\bar{m}_{jjj} - 2\sigma)$
- $(\bar{m}_{jjj} + 3\sigma) < m_{jjj} < (\bar{m}_{jjj} + 5.5\sigma)$

where $\bar{m}_{jjj}$ and σ are the mean mass and RMS width of the distribution respectively. Figure 5.11b shows the mass peak with the background subtracted. There is still a shoulder on the high mass tail of the distribution. This shoulder can be reduced with further cuts.

Lepton cuts

A pair of OSSF leptons are produced in the decay chain studied in this analysis (figure 5.6a). Requiring that these leptons are observed significantly reduces the number of reconstructed $\tilde{\chi}_1^0$s but leads to an improved mass peak. In any case, the leptons must be identified to find the slepton and $\tilde{\chi}_2^0$ masses and will be seen to be essential in reducing the SM background (section 5.6.5).

Figure 5.12 shows the transverse momenta of HERWIG generated leptons ($e^{\pm}$ or $\mu^{\pm}$) from the $\tilde{\chi}_2^0$ and right-slepton decays in the left-squark decay chain. These leptons are labelled l_a and l_b respectively for convenience of reference. Approximately 95% and 85% of the leptons in figures 5.12a and 5.12b respectively have a transverse momentum greater than 15 GeV.

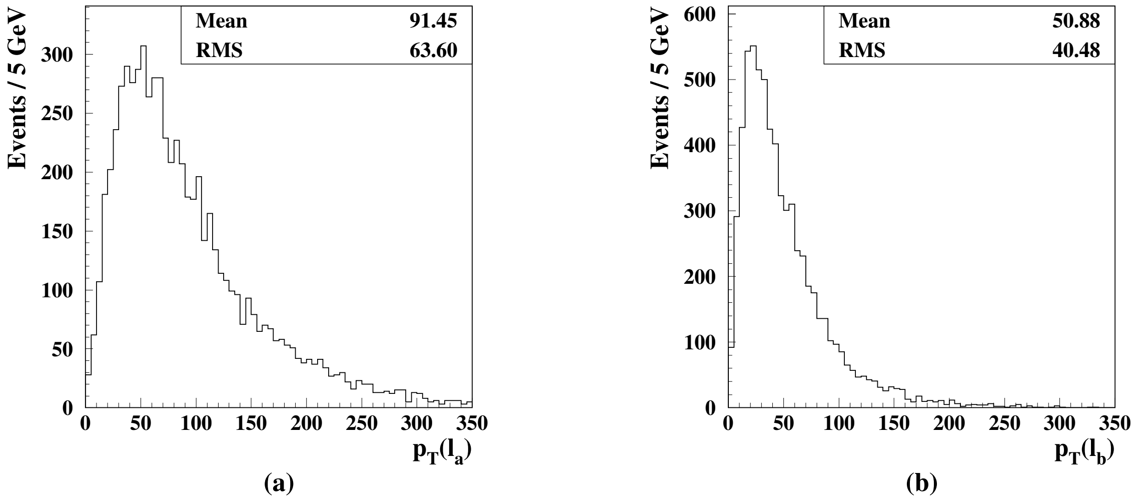

Figure 5.12: The transverse momentum distribution, measured at the generator level, of the lepton from: **(a)** the $\tilde{\chi}_2^0$ decay in the left-squark decay chain; **(b)** the right-slepton decay in the left-squark decay chain.

Events passing the jet cuts ($n_{jet}^{(max)} = 10$) and containing two OSSF leptons with $p_T > 15$ GeV were selected. The distribution of the invariant mass of the two leptons, m_{ll}, is plotted in figure 5.13. To determine the sample purity, the leptons were matched spatially to the HERWIG generated particles. 26% of lepton pairs found by ATLFAST had at least one lepton not from the decay chain, $\tilde{\chi}_2^0 \to \tilde{l}_R l \to ll\tilde{\chi}_1^0$. This background is shown as the hatched component of the histogram. Using dedicated cuts, the position of the sharp upper edge was measured in [88] to be at $109 \pm 0.3(\mathrm{stat}) \pm 0.11(\mathrm{syst})$ GeV. In this analysis, a requirement of exactly two OSSF leptons with $p_T > 15$ GeV and with $m_{ll} < 109$ GeV is added to the previously described jet cuts.

Figure 5.14 shows the $\tilde{\chi}_1^0$ mass distributions obtained with lepton and jet cuts. In figure 5.14a the distribution before background subtraction is shown for an upper limit of 10 jets. The mass peaks with background subtracted are shown in figures 5.14b-d for $n_{jet}^{(max)} = 9$, 10 and 11 respectively. Table 5.7 summarises the reconstruction efficiency, bias and mass precision for the three values of $n_{jet}^{(max)}$.

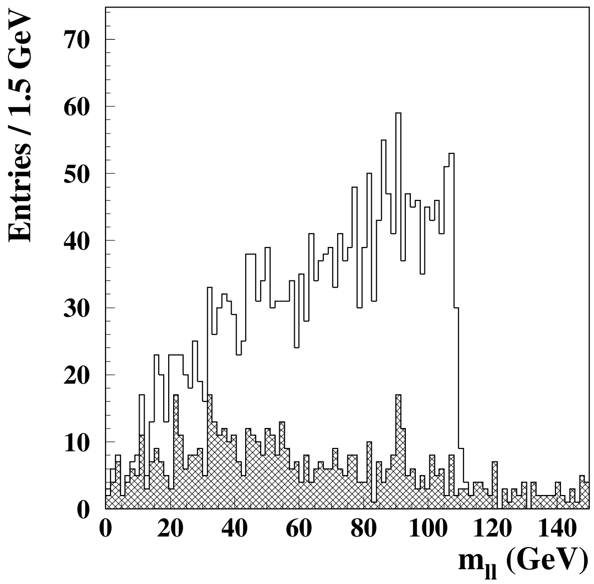

Figure 5.13: The invariant mass distribution of the 2 leptons found by applying the jet cuts described in the text and requiring two leptons with $p_T > 15$ GeV. The shaded section of the histogram shows the m_{ll} distribution of lepton pairs not from the decay $\tilde{\chi}_2^0 \rightarrow \tilde{l}_R l \rightarrow ll\ \tilde{\chi}_1^0$.

$n_{jet}^{(max)}$	Reconstruction efficiency		Bias	Mass precision
	ϵ_1(%)	ϵ_2 (%)	(GeV)	(GeV)
9	0.4	0.1	-3.0	0.87
10	1.1	0.4	-5.1	0.43
11	2.0	0.6	-5.0	0.26

Table 5.7: The efficiency, bias and precision of the $\tilde{\chi}_1^0$ reconstruction for the lepton and jet cuts. In three years, 27000 SUSY events in which exactly one $\tilde{\chi}_2^0$ decays via a slepton are expected. ϵ_1 is the fraction of these events in which at least one reconstructed $\tilde{\chi}_1^0$ was well matched to the generated sparticle. ϵ_2 is the fraction of events with two matched $\tilde{\chi}_1^0$s.

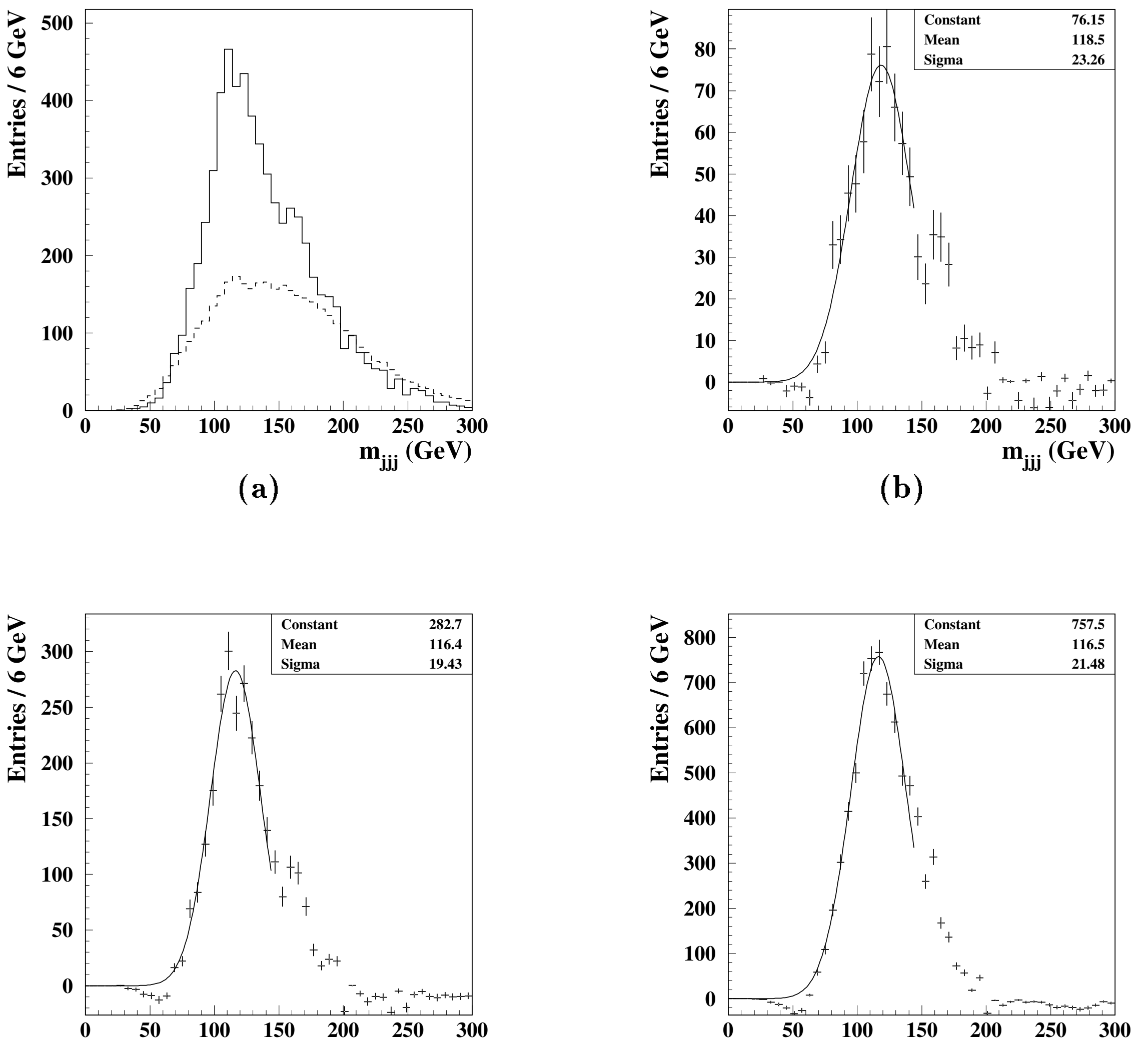

Figure 5.14: **(a)** The invariant mass of three-jet combinations passing the lepton and jet cuts (solid histogram) and generated background distribution (dashed histogram) for $n_{jet}^{(max)} = 10$. The m_{jjj} distributions with background subtracted are shown for **(b)** $n_{jet}^{(max)} = 9$, **(c)** $n_{jet}^{(max)} = 10$ and **(d)** $n_{jet}^{(max)} = 11$. All histograms were generated from a sample of 700000 SUSY events.

The optimal upper limit on the number of jets is $n_{jet}^{(max)} = 10$. For $n_{jet}^{(max)} = 11$ the reconstruction efficiency and mass precision are better but there is a small shoulder on the mass peak between 130 GeV and 150 GeV which is not present for lower values of $n_{jet}^{(max)}$. This shoulder results in a less negative bias for $n_{jet}^{(max)} = 11$ than for $n_{jet}^{(max)} = 10$. Using spatial matching of $\tilde{\chi}_1^0$s, it was shown, in section 5.6.2, that the expected bias is -10 GeV (see figure 5.7). The reconstruction efficiencies ϵ_1 and ϵ_2 are 1.5 and 1.8 times larger for $n_{jet}^{(max)} = 11$ than for $n_{jet}^{(max)} = 10$. The number of events in the $\tilde{\chi}_1^0$ mass peak increases by a factor of 3 when $n_{jet}^{(max)}$ is increased from 10 to 11. The ratio of good to background entries is therefore better in the peak with $n_{jet}^{(max)} = 10$.

A small peak is seen on the upper tail of the mass distributions in each of the plots in figure 5.14. The position of this peak approximately coincides with the mass of the lighter right-sleptons in the mSUGRA point 5 scenario. It was concluded in [88] that the slepton mass is found when the lepton from a slepton decay is not isolated but inside one of the three $\tilde{\chi}_1^0$ jets. Since the cone used to define a cluster is narrow ($\Delta R = 0.4$) the invariant mass of the three $\tilde{\chi}_1^0$ jets would in fact be approximately the invariant mass of the jets and the lepton. To produce figure 5.14, a cut of exactly 2 isolated leptons was applied to the data. If the lepton from the slepton decay is within a jet, a lepton from another source is needed to give a total of two isolated leptons.

To test the hypothesis that the secondary peak is due to a reconstructed slepton mass, the two leptons identified by ATLFAST were spatially matched to the HERWIG generated leptons from the $\tilde{\chi}_2^0$ and slepton decays. When the $\tilde{\chi}_1^0$ mass distribution was plotted using only events in which there was a good match between the ATLFAST and HERWIG leptons, the secondary peak was still observed. It was also noted that in events with matched leptons, only one slepton was generated by HERWIG. This evidence suggests that the hypothesis is incorrect and that the peak has another origin.

The number of events in the secondary peak is much smaller than the number of events in the signal and background peaks beneath it. It was, therefore, not possible to identify the source of the secondary peak.

b-tagging cuts

No b-quarks are produced in the $\tilde{\chi}_1^0$ decay if the only non-zero RPV coupling is λ''_{212}. Some wrong combinations of jets can therefore be eliminated by using b-jet tagging. In practice, for a high b-tagging efficiency there is a finite chance of mis-tagging non b-jets (table 5.3). The mis-tagging probability is highest for c-jets, two of which are produced in most events when $\lambda''_{212} = 0.005$. For a b-tagging efficiency of 64%, there is a 25% probability of mis-tagging a c-jet and therefore a 50% chance of rejecting a correct combination of 6 jets from 2 $\tilde{\chi}_1^0$s. For lower b-tagging efficiencies, an improved c-jet rejection can, however, be obtained.

b-tagging efficiency (%)	c-jet rejection factor	Reconstruction efficiency ϵ_1(%)	Reconstruction efficiency ϵ_2 (%)	bias (GeV)	mass precision (GeV)
100%	∞	1.08	0.38	-5.3	0.4
33%	22.9	1.04	0.38	-4.2	0.4
64%	4.2	0.67	0.23	-4.6	0.5

Table 5.8: The efficiency, bias and precision of the $\tilde{\chi}_1^0$ mass reconstruction with lepton, jet ($n_{jet}^{(max)} = 10$) and b-tagging cuts for three different b-tagging efficiencies.

To investigate the usefulness of b-tagging, a b-jet veto was added to the lepton and jet cuts. Any combination of three jets containing a b-tagged jet was rejected. Table 5.8 lists the bias, efficiency and precision of the $\tilde{\chi}_1^0$ mass reconstruction for three different b-tagging efficiencies.

A small improvement in the mass peak bias is seen for an unrealistic b-tagging efficiency of 100%. When a realistic b-tagging efficiency is used, however, the reconstruction efficiency is degraded without a significant improvement in the mass precision or the bias of the mass peak. b-tagging is, therefore, not used in this study.

Cuts summary

For convenience, the chosen cuts are listed together (all p_T in GeV):

- Number of jets in an event: $8 \leq n_{jet} \leq 10$
- Kinematic cuts on $\tilde{\chi}_1^0$ jets:
  - $100 < p_T^{(a1)}$; $17.5 < p_T^{(a2)} < 300$; $15.0 < p_T^{(a3)} < 150$
  - $17.5 < p_T^{(b1)} < 300$; $17.5 < p_T^{(b2)} < 150$; $15.0 < p_T^{(b3)} < 75$
  - $\Delta R_{12}^{(a)} < 1.3$; $\Delta R_{12-3}^{(a)} < 1.3$
  - $\Delta R_{12}^{(b)} < 2.0$
- Kinematic cuts on hard jets:
  - $p_T^{(h1)} > 200$; $|\eta^{(h1)}| < 2$
  - $p_T^{(h2)} > 100$; $|\eta^{(h2)}| < 2$
- Lepton cuts
  - $p_T^{(l^a)} > 15$; $p_T^{(l^b)} > 15$
  - m_{ll} <109 GeV

In this chapter, these cuts will be referred to as follows:

- Jet cuts = cuts on jet multiplicity + cuts on $\tilde{\chi}_1^0$ jets + cuts on hard jets
- Dilepton cuts = jet cuts + lepton cuts

It is shown in later sections that the dilepton cuts alone are sufficient to extract the $\tilde{\chi}_1^0$, slepton and $\tilde{\chi}_2^0$ masses from SUSY events.

The $\tilde{\chi}_1^0$ mass peak so far obtained has a central mass of 116.4 GeV which is significantly higher than the centre of the matched mass peak (111 GeV). The distribution from the dilepton cuts is also twice as wide as the matched peak. Later in this chapter it is shown that a $\tilde{\chi}_1^0$ mass consistent with the matched mass distribution can be obtained. This suggests that there is a significant number of background entries in the mass peak from the dilepton cuts and that this background biases the peak to a higher mass.

In some mSUGRA models, the lightest right-sleptons are more massive than the $\tilde{\chi}_2^0$ and the decay chain exploited by the dilepton cuts is not present. In such a scenario, it would be important to better understand the bias of the mass peak obtained with the jet cuts alone.

5.6.5 SM backgrounds

The dilepton cuts used to extract a $\tilde{\chi}_1^0$ mass from the SUSY background are exacting. The SM production processes listed in table 5.9 were used to investigate whether further cuts are needed to suppress SM backgrounds.

The cross section of QCD processes are large and it would be impossible to generate a useful fraction of the expected number of QCD events. The QCD cross section, however, is dominated by soft events. If it can be shown that such events would not pass some set of selection cuts, then only energetic QCD events need to be considered. For this reason, the QCD cross section is listed for ranges of $p_T^{(2-2)}$, the transverse momentum of both out-going partons of the hard process. Other SM background processes have been similarly divided.

Process	$p_T^{(min)}$ (GeV)	$p_T^{(max)}$ (GeV)	Cross section (pb)	Events in 3 years
QCD	10	100	4.95×10^9	1.6×10^{14}
QCD	100	200	1.26×10^6	4.0×10^{10}
QCD	200	300	5.87×10^4	1.9×10^9
QCD	300	400	8045	2.6×10^8
QCD	400	500	1766	5.7×10^7
QCD	500	600	507.1	1.6×10^7
QCD	600	700	173.6	5.6×10^6
QCD	700	10^8	122.7	3.9×10^6
$t\bar{t}$	10	100	258.3	8.3×10^6
$t\bar{t}$	100	10^8	321.3	10.3×10^6
Z+jets	10	100	4448	1.4×10^8
Z+jets	100	10^8	134.5	4.3×10^6
W+jets	10	100	5.67×10^4	1.8×10^9
W+jets	100	10^8	1411	45.2×10^6
SUSY	10	10^8	21.89	700000

Table 5.9: The cross sections of potential SM backgrounds. Each process is divided into ranges of $p_T^{(2-2)}$, the transverse momentum of each of the two out-going partons from the hard process.

Process ($p_T^{(min)}$, $p_T^{(max)}$)	Events generated	Events passing cuts: Jets	1 lepton	Dilepton	Dilepton cut 90% upper CL (in 3 years)
QCD (10,100)	2.5×10^6	0	0	0	-
QCD (100,200)	2.5×10^6	183	0	0	-
QCD (200,300)	4.0×10^6	31×10^3	54	0	1093
QCD (300,400)	2.0×10^6	121×10^3	194	0	299.0
QCD (400,500)	0.5×10^6	63×10^3	187	0	262.2
QCD (500,600)	0.5×10^6	104×10^3	377	0	73.6
QCD (600,700)	0.5×10^6	112×10^3	541	4	89.5
QCD (700,10^8)	0.5×10^6	162×10^3	1176	8	101.0
$t\bar{t}$ (10,100)	2.5×10^6	303	11	0	7.6
$t\bar{t}$ (100,10^8)	7.9×10^6	186×10^3	8.8×10^3	15	27.8
Z+jets (10,100)	0.5×10^6	0	0	0	-
Z+jets (100,10^8)	1.0×10^6	571	0	0	-
W+jets (10,100)	0.5×10^6	0	0	0	-
W+jets (100,10^8)	1.0×10^6	643	5	0	104
				Total	2058

Table 5.10: The number of SM events generated and passing the three sets of SUSY cuts described in the text. The right-most column gives the 90% upper confidence limit on the number of events passing the dilepton cuts.

Table 5.10 lists the number of SM events generated and passing three different sets of cuts:

- Jet cuts (defined in section 5.6.4)
- One-lepton cuts: Jet cuts + at least one lepton with $p_T > 15$ GeV
- Dilepton cuts (section 5.6.4)

Only 12 of the 13×10^6 generated QCD events pass the dilepton cuts. From just 12 events it is impossible to draw conclusions about which $p_T^{(2-2)}$ ranges should be regarded as a source of background events. Without more information, QCD events with $10 < p_T^{(2-2)} < 100$ cannot be disregarded. And for the generated sample of 2.5×10^6 events, this QCD $p_T^{(2-2)}$ range has a 90% upper confidence limit of 1.5×10^8 events.

Fortunately, the rejection power of the dilepton cuts at different $p_T^{(2-2)}$ can be inferred from the looser one-lepton and jet cuts. The effectiveness of a set of cuts against a certain process can be measured by the fractional cross section which is defined as $\sigma_f = \sigma n/N$ where σ is the process cross section, N is the number of events generated and n is the number of events passing the cuts. The rate at which events would pass the cuts is the product of σ_f and the LHC luminosity. Figure 5.15 shows σ_f plotted against $p_T^{(2-2)}$ for QCD events. The probability of a QCD event passing the jet cuts is seen to fall sharply below $p_T^{(2-2)} = 200$ GeV. It is inferred that a similar fall occurs for the 1 lepton and 2 lepton cuts and that the contribution from QCD events with $p_T^{(2-2)} < 200$ GeV is insignificant.

The last column of table 5.10 lists the 90% upper confidence limit on the number of events passing the 2 lepton cuts. A total of 2058 events is found for the processes considered. In the $\tilde{\chi}_1^0$ mass peak, there are 6404 entries before background subtraction (figure 5.14a). The combined distribution from SM and SUSY processes would, therefore,

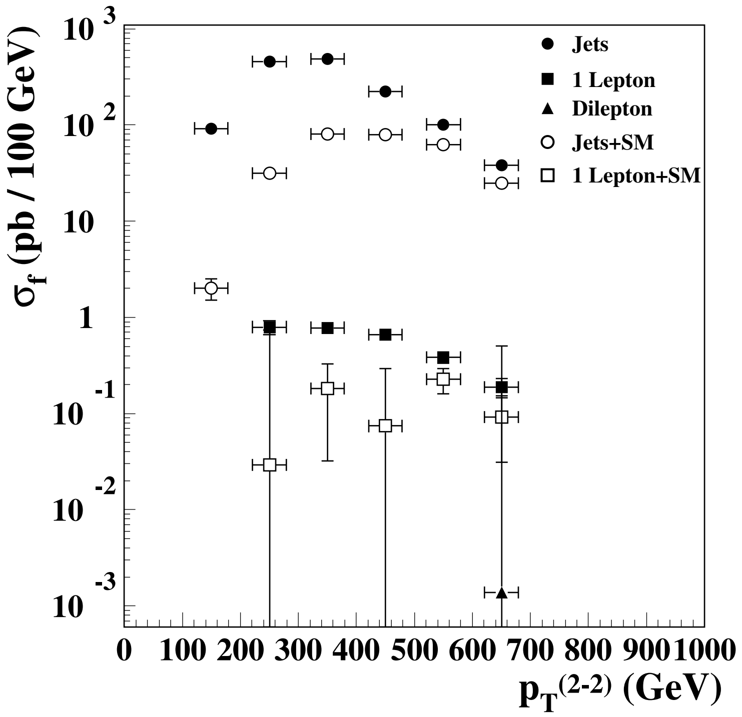

Figure 5.15: The fractional QCD cross section, σ_f, plotted against $p_T^{(2-2)}$ for various SM and SUSY cuts.

not be dominated by SM backgrounds and, by using a background subtraction, it should still be possible to extract a $\tilde{\chi}_1^0$ mass peak. In section 5.6.6, it will be shown that nearly all combinatorial SUSY background can be removed from the $\tilde{\chi}_1^0$ mass peak using the 2 leptons produced in the $\tilde{\chi}_2^0$ decay chain. This method is likely to also be effective at removing any SM background.

It is possible that the SM background has been underestimated. In [92], particle level simulations were shown to give lower QCD rates than full Monte Carlo simulations. If necessary, additional cuts can be used to further reduce the SM background. For example, the following cuts are used in [88] to obtain an implicit SUSY signature in

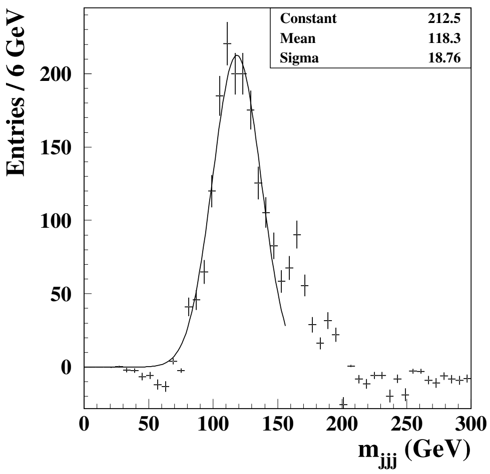

Figure 5.16: The $\tilde{\chi}_1^0$ mass distribution with BG subtracted for three-jet combinations passing the dilepton and SM cuts (700000 SUSY events generated).

RPV mSUGRA models:

- Thrust cut: $T = \max_{\vec{n}} \frac{\sum_i |\vec{p_i}.\vec{n}|}{\sum_i |\vec{p_i}|} < 0.9$
- Sphericity cut: $S = \frac{3}{2} \min_{\vec{n}} \frac{\sum_i |\vec{p_i}.\vec{n}|}{\sum_i |\vec{p_i}|} > 0.1$
- Transverse energy cut: $m_T^{(cent)} = \sum_{|\eta|<2} p_T^{(jet)} + \sum_{|\eta|<2} p_T^{(lepton)} > 1000$ GeV

The thrust and sphericity are maximised and minimised respectively by the choice of the vector $\vec{n}$. The sums are over all jet three-momenta. Both T and S measure the spherical symmetry of an event. For a pencil-like event, with partons produced back to back in narrow cones, $T = 1$ and $S = 0$. In an isotropic event $T = \frac{1}{2}$. The sums in $m_T^{(cent)}$ are over all jets and leptons with $|\eta| < 2$. In this chapter, these three cuts are referred to as the SM cuts.

In figure 5.15, σ_f is plotted for the SM cuts added to the jet and 1 lepton cuts. The SM background is reduced, especially at lower values of $p_T^{(2-2)}$. Figure 5.16 shows the $\tilde{\chi}_1^0$

mass peak with the SUSY and SM cuts applied to the SUSY data-set. The efficiency of reconstructing at least one well matched $\tilde{\chi}_1^0$, $\epsilon_1 = 0.84\%$. The reconstruction efficiency for two well matched $\tilde{\chi}_1^0$s is 0.27%. Although the $\tilde{\chi}_1^0$ reconstruction efficiency is lower than for just SUSY cuts, a $\tilde{\chi}_1^0$ mass peak can still be found.

5.6.6 Measuring the slepton and $\tilde{\chi}_2^0$ masses

Nearly all right-selectrons and right-smuons decay into a $\tilde{\chi}_1^0$ and a lepton. The slepton mass can be measured by finding the invariant mass of these two particles.

The dilepton cuts, defined in section 5.6.4, require a pair of OSSF leptons with $m_{ll}^{(max)} < 109$ GeV. These cuts are intended to select leptons from the $\tilde{\chi}_2^0$ and slepton decays in the left-squark decay chain. Spatial matching was used to assess the purity of events passing the cuts. In 74% of events, the 2 leptons found by ATLFAST were from the $\tilde{\chi}_2^0$ and slepton decays.

In section 5.6.4, a $\tilde{\chi}_1^0$ mass peak was found with width 19.4 GeV and centred at 116.4 GeV. A statistical subtraction was used to remove a broad background beneath the $\tilde{\chi}_1^0$ mass peak. Three-jet combinations passing the dilepton cuts and with m_{jjj} within 2 standard deviations (38.8 GeV) of the mass peak centre are used to find the slepton mass. The fact that a statistical background subtraction was used to obtain the $\tilde{\chi}_1^0$ mass peak indicates that a large fraction of the 3-jet combinations in this sample are from backgrounds.

For now, it is assumed that an accurate jet energy scale correction for high jet multiplicity is used. The 4-momenta of jets from $\tilde{\chi}_1^0$ decays are multiplied by a correction factor, $c_j = \frac{m_{\tilde{\chi}_1^0}}{m_{jjj}}$ where $m_{\tilde{\chi}_1^0}$ is the true $\tilde{\chi}_1^0$ mass and m_{jjj} is the invariant mass of the three jets before calibration. The jet energy scale correction will be considered in detail

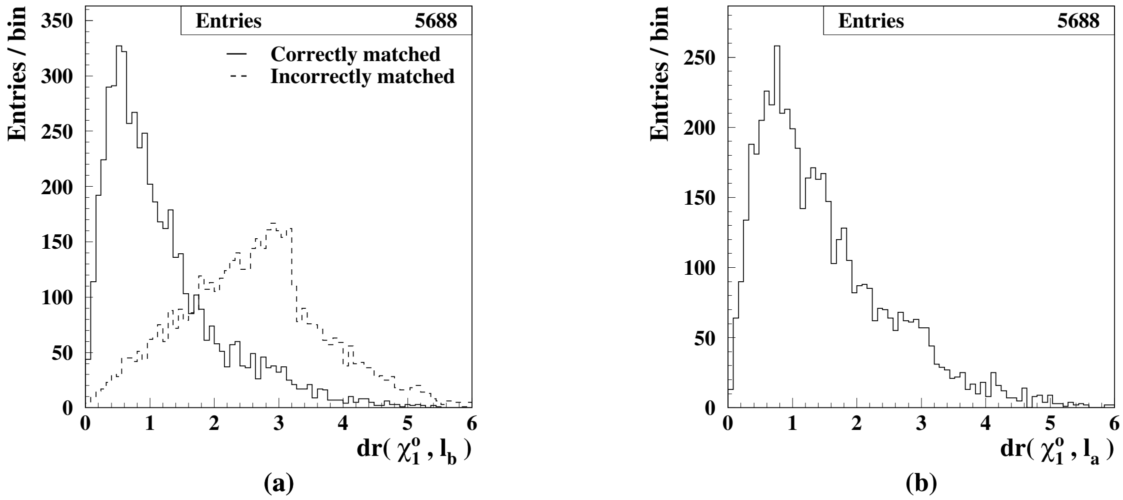

Figure 5.17: **(a)** The solid histogram shows the separation in (η,ϕ) of a $\tilde{\chi}_1^0$ and lepton from a slepton decay. The dashed histogram shows the separation between the same lepton and the other $\tilde{\chi}_1^0$ in the event. **(b)** The separation in (η,ϕ) of the lepton produced in the decay $\tilde{\chi}_2^0 \rightarrow \tilde{l}l$ and the $\tilde{\chi}_1^0$ from the slepton decay.

in section 5.6.9.

There are two leptons and two $\tilde{\chi}_1^0$s in each event selected by the dilepton cuts. The spatial separation of particles was used to identify the particles from the slepton decay. Figure 5.17a shows $dr(\tilde{\chi}_1^0, l_b)$, the angular separation between the $\tilde{\chi}_1^0$ from the slepton decay and the lepton, l_b, from the slepton decay measured at the generator level. Figure 5.17b shows $dr(\tilde{\chi}_1^0, l_a)$, the separation between the $\tilde{\chi}_1^0$ from the slepton decay and the lepton, l_a, from the $\tilde{\chi}_2^0$ decay. 65% of events have $dr(\tilde{\chi}_1^0,l_b) < dr(\tilde{\chi}_1^0,l_a)$. Also superimposed on figure 5.17a is the distribution of the separation between l_b and the $\tilde{\chi}_1^0$ from the other sparton decay chain of the event. On average, the $\tilde{\chi}_1^0$ and l_b from the same slepton are closer together than wrong combinations. In this analysis, the invariant mass of the lepton-$\tilde{\chi}_1^0$ pair with the smallest angular separation is used as a measure of the slepton mass.

Figure 5.18a shows the distribution obtained for m_{jjjl}, the invariant mass of the

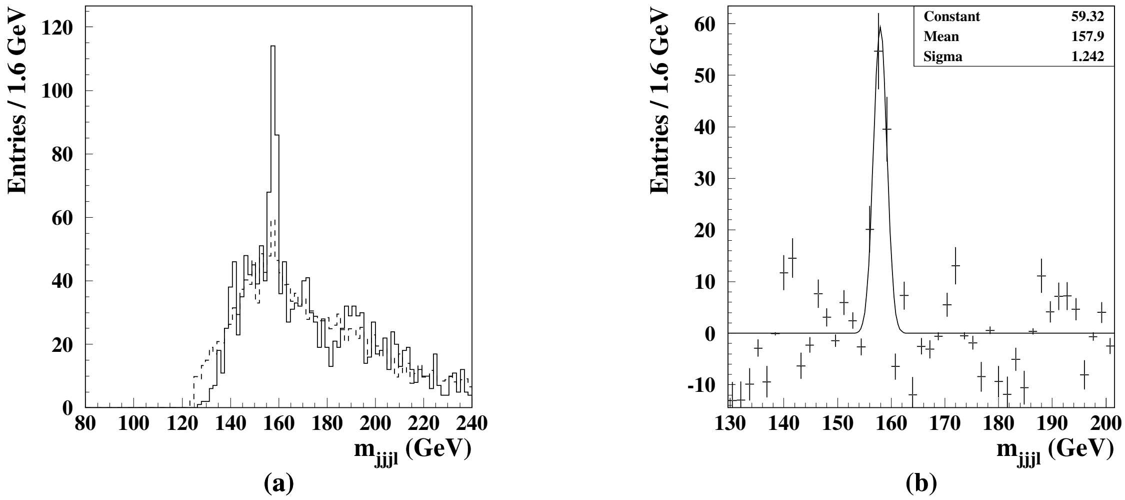

Figure 5.18: (**a**) The solid histogram shows the invariant mass of the $\tilde{\chi}_1^0$ and l_b found using the algorithm described in the text. A sharp peak at approximately 160 GeV is clearly visible. A generated background histogram is also shown (dashed histogram). (**b**) The m_{jjjl} distribution with background subtracted.

three jets and lepton. A narrow peak is seen at approximately the true slepton mass (157.2 GeV). There is large background under the slepton peak which has several sources:

- Background three-jet combinations from the $\tilde{\chi}_1^0$ mass peak
- Leptons not from the $\tilde{\chi}_2^0$ decay chain
- Wrong combinations of the $\tilde{\chi}_1^0$ and lepton

A background distribution to m_{jjjl} was generated by applying the above described slepton mass algorithm to the three-jet combinations used to generate the m_{jjj} background. The generated slepton mass background is superimposed on figure 5.18a. It has been normalised to the observed background using histogram bins with $m_{jjjl} > 175$ GeV.

Figure 5.18b shows the slepton mass peak with the background subtracted. The fitted Gaussian has a mean value of 157.9 ± 0.1 GeV and a width of 1.2 ± 0.1 GeV. A

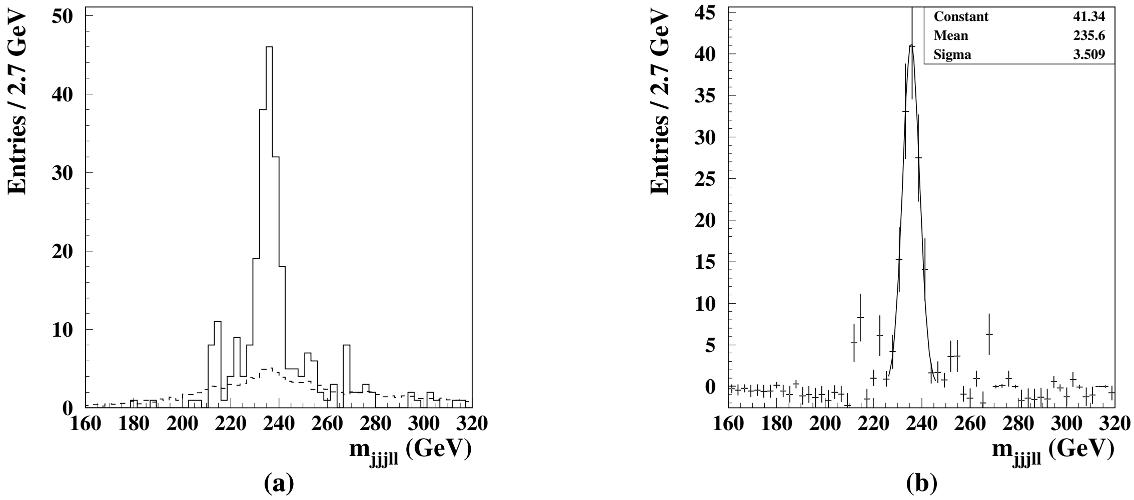

Figure 5.19: **(a)** The m_{jjjll} distribution obtained using the algorithm described in the text. The small background can be generated (dashed histogram). **(b)** The m_{jjjll} distribution with the generated background subtracted.

cleaner mass peak is obtained in the next section.

The $\tilde{\chi}_2^0$ mass is the invariant mass of the slepton and the unused lepton. Events with $|m_{jjjl} - 157.9| < 2.4$ GeV were used to obtain the $\tilde{\chi}_2^0$ mass peak shown in figure 5.19a. The small background below the peak can again be generated and subtracted to give the distribution shown in figure 5.19b. The Gaussian fitted to the peak has a mean value of 235.6 ± 0.3 GeV and a width of 3.5 ± 0.2 GeV. The systematic errors of the mass measurement are discussed in section 5.6.9.

5.6.7 Remeasuring the $\tilde{\chi}_1^0$ and slepton masses

By selecting events with a $\tilde{\chi}_2^0$ mass in the peak of figure 5.19b, the background entries in the slepton and $\tilde{\chi}_1^0$ peaks can be almost entirely removed. The $\tilde{\chi}_1^0$ and slepton mass distributions for these events are plotted in figures 5.20a and 5.20b. There are 170 entries in each histogram. The mean $\tilde{\chi}_1^0$ mass agrees, within errors, with the position of the

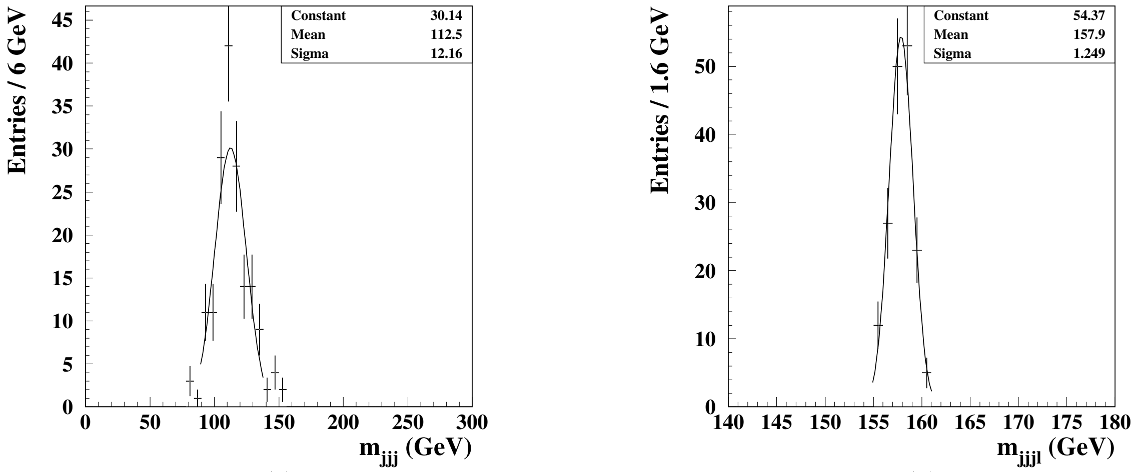

(a) (b)

Figure 5.20: **(a)** $\tilde{\chi}_1^0$ and **(b)** slepton mass distributions obtained using events with $|m(\tilde{\chi}_2^0) - 235.6| < 7.0$ GeV

Lepton	Entries	$\tilde{\chi}_1^0$		Slepton		$\tilde{\chi}_2^0$	
		Mean	Width	Mean	Width	Mean	Width
$e^\pm$	81	111.0 ± 1.1	8.6 ± 1.6	157.6 ± 0.2	1.2 ± 0.1	236.0 ± 0.6	3.6 ± 0.6
$\mu^\pm$	89	114.3 ± 1.5	12.5 ± 1.2	158.2 ± 0.1	1.2 ± 0.1	235.4 ± 0.5	3.8 ± 0.4
Both	170	112.5 ± 1.2	12.2 ± 1.6	157.9 ± 0.1	1.2 ± 0.1	235.6 ± 0.3	3.5 ± 0.2

Table 5.11: A summary of the values found for the $\tilde{\chi}_1^0$, slepton and $\tilde{\chi}_2^0$ masses. The widths listed are the widths of the Gaussian fitted to the centre of the mass distribution. All mean and width values are in GeV. The statistical error on each value is also shown.

matched mass peak in figure 5.7.

Table 5.11 summarises the masses found for the $\tilde{\chi}_1^0$, slepton and $\tilde{\chi}_2^0$. The two OSSF leptons identified by the cuts can either be electrons or muons. The contributions from both lepton types are shown in the table. Decay chains involving selectrons and smuons are seen to be selected by the cuts in approximately equal proportions. The mass peak centre and width measurements for electron and muon events are equal within errors.

In this analysis, 100% muon and electron identification efficiencies have been assumed. In the actual experiment, an electron efficiency of greater than 90% will be achievable for electrons with $p_T > 15$ GeV [84]. The muon reconstruction efficiency is better than 97% for muons with $p_T > 15$ GeV [84]. With these efficiencies one would expect the loss of around 21 of the 170 events passing all cuts.

5.6.8 Loosening the jet multiplicity cut

In sections 5.6.6-5.6.7, the dilepton cuts, defined in section 5.6.4, were used to select the sample of three-jet combinations with which leptons were combined to find the slepton and $\tilde{\chi}_2^0$ masses. The dilepton cuts impose an upper limit on the jet multiplicity of $n_{jet}^{(max)} = 10$. This maximum jet multiplicity was chosen to minimise the background contribution to the $\tilde{\chi}_1^0$ mass peak whilst retaining as many well reconstructed $\tilde{\chi}_1^0$s as possible (page 137). By adding cuts on the $\tilde{\chi}_2^0$ mass to the dilepton cuts, it was shown in section 5.6.7 that nearly all background entries can be eliminated. It is therefore possible to loosen the jet multiplicity cut and obtain clean $\tilde{\chi}_1^0$, slepton and $\tilde{\chi}_2^0$ mass distributions with more entries. Table 5.12 lists the masses obtained for various values of $n_{jet}^{(max)}$. Figure 5.21 shows the $\tilde{\chi}_1^0$, slepton and $\tilde{\chi}_2^0$ mass distributions for $n_{jet}^{(max)} = 12$. The mass peaks for $n_{jet}^{(max)} > 12$ were observed to have significant contributions from backgrounds.

5.6.9 Systematic errors

The uncertainty in the jet energy scale will dominate the systematic errors on the $\tilde{\chi}_1^0$, slepton and $\tilde{\chi}_2^0$ masses. A simple cone algorithm was used in this analysis to identify jets from the $\tilde{\chi}_1^0$ decay. A more sophisticated algorithm would be used in a precision mass measurement. It has nevertheless been demonstrated here that some light sparticle masses can be measured using the cone algorithm. The systematics of these measure-

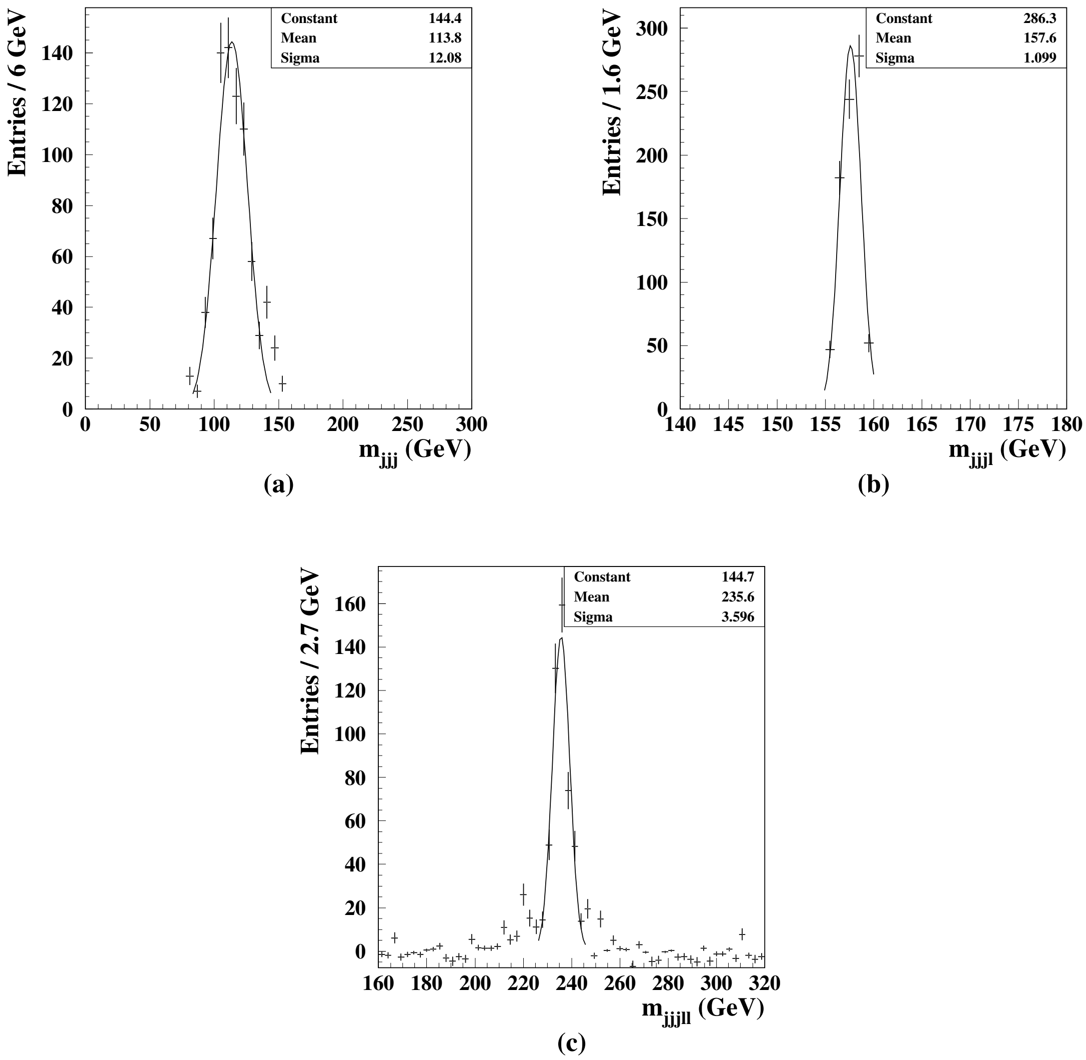

Figure 5.21: **(a)** $\tilde{\chi}_1^0$, **(b)** right-slepton and **(c)** $\tilde{\chi}_2^0$ mass distributions for $n_{jet}^{(max)} = 12$.

$n_{jet}^{(max)}$	Entries	$\tilde{\chi}_1^0$ mass	right-slepton mass	$\tilde{\chi}_2^0$ mass
10	170	112.5 ± 1.2	157.9 ± 0.10	235.6 ± 0.3
11	391	113.6 ± 0.8	157.9 ± 0.05	235.9 ± 0.2
12	803	113.8 ± 0.5	157.6 ± 0.02	235.6 ± 0.2
13	2864	114.3 ± 0.4	157.0 ± 0.1	233.2 ± 0.2

Table 5.12: $\tilde{\chi}_1^0$, right-slepton and $\tilde{\chi}_2^0$ masses found for four upper limits on the jet multiplicity, $n_{jet}^{(max)}$.

ments are considered below.

A logical next step in this analysis would be to use a jet clustering algorithm more suited to high multiplicity events. One choice might be the vector cell cluster algorithm which, instead of combining individual jets, finds the invariant mass of all calorimeter cells within a certain region. This algorithm minimises problems from energy sharing between clusters and out-of-cone energy losses. In [93], the cell vector algorithm was used to find the W mass from nearly colinear jets using parton level and full simulations. The results from the two simulations were found to differ significantly. An analysis using the cell vector algorithm is, therefore, best performed using full simulation and is beyond the scope of this study.

$\tilde{\chi}_1^0$ mass systematics

Several effects contribute to the mis-measurement of the mass of a particle reconstructed from 2 or more jets:

- Out-of-cone energy: Not all of a parton's energy is deposited within a cone of half-angle, $\Delta R = 0.4$. The fraction within the cone is p_T and process dependent. Using W+jets events, the ratio $p_T^{(jet)}/p_T^{(partons)}$ was found in [84] to be approximately 0.9 for $50 < p_T^{(parton)} < 200$ GeV. This ratio is much closer to unity if a cone with half-angle, $\Delta R = 0.7$ is used.
- Mis-measurement of the angular separation of jets [93].
- Final state radiation (FSR) of partons. [78] considers the reconstruction of the SM Higgs using the decay $H \to b\bar{b}$. The Higgs mass is found with and without FSR simulated. With no FSR or hadronisation, the Higgs mass peak is centred on its nominal mass of 100 GeV. A downward shift of the mass peak of 8 GeV is seen

when FSR is turned on. Hadronisation further decreases the mean mass of the peak.

A jet energy correction parameterisation is provided in ATLFAST based on a study of $H \to b\bar{b}$, $H \to u\bar{u}$ and $H \to gg$ reconstruction. The correction is made by multiplying jet 4-momenta by a p_T and jet-flavour dependent number. The correction has not been used in any of the results so far presented in this chapter.

In this study, the accuracy of the ATLFAST jet energy correction is first studied using the hadronic reconstruction of the top-quark. A sample of 2.1×10^5 $t\bar{t}$ events was generated using HERWIG 5.9 with a top mass of 175 GeV. One of the t-quarks was forced to decay leptonically, the other hadronically. Events with four jets, two b-tagged and two from light quarks, were used. The W was reconstructed first by combining the two non-b-jets. Events with a reconstructed W mass within 20 GeV of the true W mass were used to find the top mass. Each b-jet was combined with the W and the invariant mass of the combination with the highest transverse momentum was used as a measure of the top mass.

Figure 5.22 shows the top mass distributions obtained with and without jet energy correction. Before jet energy correction, the fitted Gaussian is centred at 149.9 GeV. When the jet energy correction is applied, the peak overshoots the generated top mass by 5 GeV. By reducing the correction factor by 3.2%, a mass peak with a mean equal, within errors, to the generated top mass was obtained. Each of the three peaks has a low mass tail due to FSR.

In ATLAS, approximately 1500 $t\bar{t}$ events with one top-quark decaying leptonically are expected per day. The reconstruction of the hadronically decaying Ws in these events will be instrumental in understanding jet energy scale systematics [84].

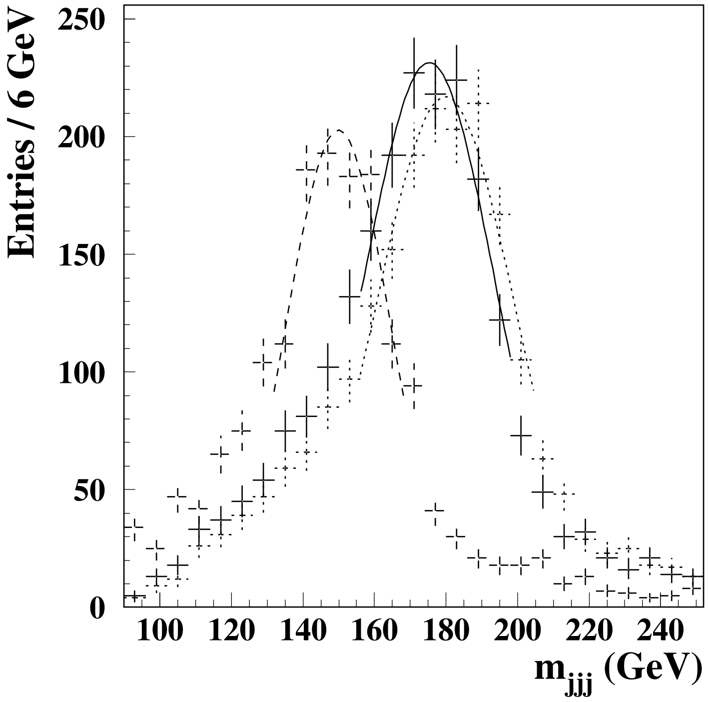

Figure 5.22: The reconstructed top mass for: no energy correction (dashed histogram, $m_t = 149.9 \pm 0.7$ GeV); the standard ATLFAST correction (dotted histogram, $m_t = 179.8 \pm 0.8$ GeV) and a modified ATLFAST correction (solid histogram, $m_t = 175.3 \pm 0.9$ GeV). The result are for 2.1×10^5 $t\bar{t}$ events generated with HERWIG 5.9 with the top mass set to 175 GeV.

When the modified ATLFAST jet energy reconstruction was applied to the $\tilde{\chi}_1^0$ jets in the 170 events passing all cuts ($n_{jet}^{(max)} = 10$), a $\tilde{\chi}_1^0$ mass peak centred at 129.5 GeV was obtained. The true $\tilde{\chi}_1^0$ mass is 121.5 GeV. Clearly the correction used to find the top mass is not directly applicable. Several possible sources of the discrepancy were investigated. The following are discussed in more detail below: different process kinematics, a different jet multiplicity in events and final state radiation.

The kinematics of the top-quark and $\tilde{\chi}_1^0$ decays are significantly different. The average separation of the two hardest jets in the $\tilde{\chi}_1^0$ decay was found to be approximately $\Delta R = 0.8$. In the $t\bar{t}$ study, the two hardest jets had an average separation of $\Delta R = 1.4$. If the three $\tilde{\chi}_1^0$ jets are nearly touching, one might expect out-of-cone energy losses to be reduced. Geometric arguments can be used to show that one third less energy would be lost from three touching cones than from three isolated jets. Also, in [93] the mismeasurement of the angular separation of jets was found to be significant for nearly colinear jets. In this study, however, no correlation was seen between the minimum jet separation and the reconstructed $\tilde{\chi}_1^0$ mass.

Another difference between the $t\bar{t}$ and SUSY events is a higher jet multiplicity in the latter. It was hypothesised that energy sharing between $\tilde{\chi}_1^0$ jets and jets from, for example, squark decays was responsible for a higher than expected $\tilde{\chi}_1^0$ mass. Again, however, no correlation was seen between the $\tilde{\chi}_1^0$ mass and the smallest separation between the $\tilde{\chi}_1^0$ jets and jets from squark decays or the other $\tilde{\chi}_1^0$.

Another possibility is that there is little FSR in the SUSY events selected by this analysis. To be in the narrow slepton peak, the reconstructed $\tilde{\chi}_1^0$ momentum and mass must be close to their generated values. It is possible that events with significant FSR do not pass the selection cuts of this study. This hypothesis is strengthened by the absence in the $\tilde{\chi}_1^0$ mass peak of the low mass tails seen in the top mass distribution. The study of jet energy corrections in [78] identifies and separates the effects of ISR, FSR and hadronisation on the position of a Higgs mass reconstructed from two b-quarks. The position of the mass peak centre falls 8% when FSR is turned on and a further 10% of the Higgs mass when hadronisation is turned on.

In HERWIG, it is difficult to simply turn off FSR. If it were possible, the hypothesis of reduced FSR in the $\tilde{\chi}_1^0$ events could be tested by comparing the shifts in the $\tilde{\chi}_1^0$ and

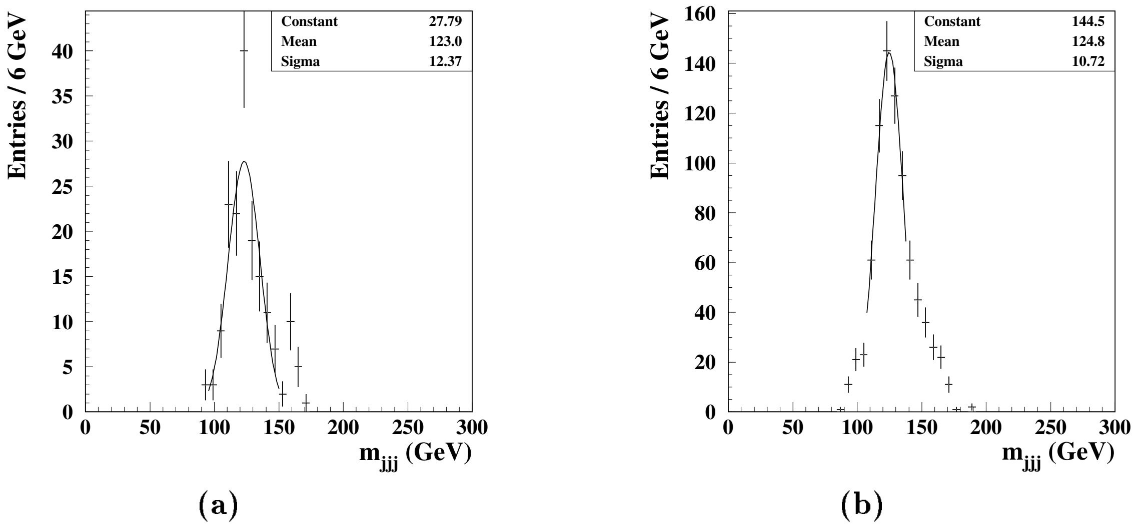

Figure 5.23: The $\tilde{\chi}_1^0$ mass distribution obtained using a modified ATLFAST jet calibration (see text for details) for **(a)** $n_{jet}^{(max)} = 10$ and **(b)** $n_{jet}^{(max)} = 12$.

top mass peaks when FSR is turned off. If there is indeed less FSR in the SUSY events, the $\tilde{\chi}_1^0$ mass peak would be expected to shift upwards by less than the top mass peak. In the absence of this test, the ATLFAST jet energy calibration factors were reduced by 0.44; the fraction, in [78], of the downward shift of the Higgs mass peak attributed to FSR. The factor of 0.968 needed to obtain a correct top mass was also applied to the $\tilde{\chi}_1^0$ jets. The resulting $\tilde{\chi}_1^0$ mass peaks for $n_{jet}^{(max)} = 10$ and $n_{jet}^{(max)} = 12$ are shown in figure 5.23. The distributions have mean values of 123.0 ± 1.2 GeV and 124.8 ± 0.6 GeV respectively. There is small shoulder in the distributions at around 160 GeV. The events in this secondary peak were found to have a wider separation between $\tilde{\chi}_1^0$ jets suggesting that any jet energy scale correction is highly dependent on process kinematics.

Using no jet energy correction, a $\tilde{\chi}_1^0$ mass of 112.5 GeV was obtained. Naïvely applying the standard ATLFAST jet calibration yields $m_{\tilde{\chi}_1^0} = 129.5$ GeV. These two values can be used to set an upper limit of $\sim$8 GeV on the systematic uncertainty in the $\tilde{\chi}_1^0$ mass. It was postulated, although not definitively demonstrated, that the ATLFAST

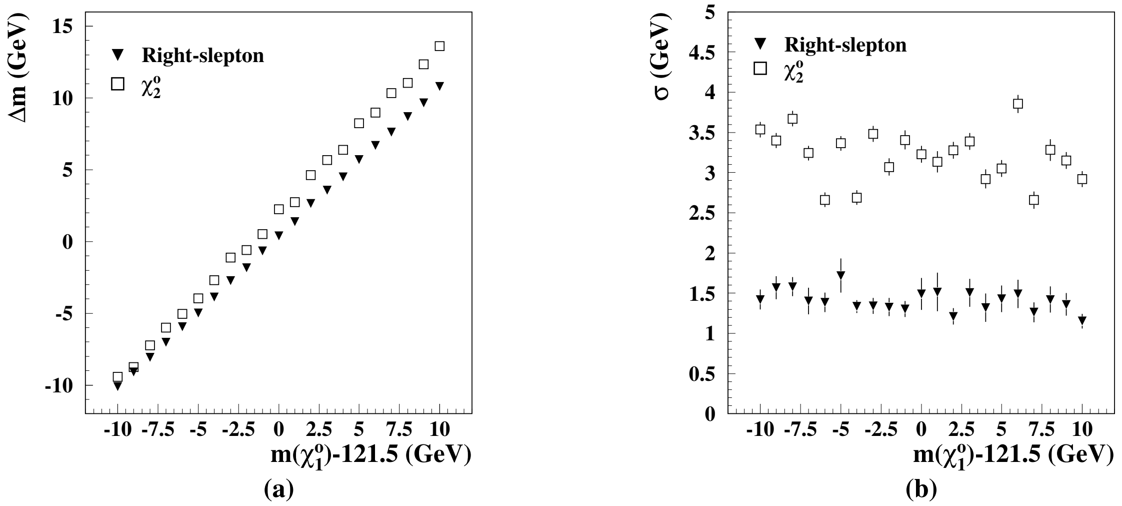

Figure 5.24: **(a)** The variation of the error on the right-slepton and $\tilde{\chi}_2^0$ masses with the difference between the true $\tilde{\chi}_1^0$ mass (121.5 GeV) and the mass, $m(\tilde{\chi}_1^0)$, assumed in jet energy correction prior to finding the slepton mass. **(b)** The width of the slepton and $\tilde{\chi}_1^0$ mass peaks plotted against $m(\tilde{\chi}_1^0)-121.5$.

jet calibration over-corrects the $\tilde{\chi}_1^0$ mass because of reduced FSR in the events selected by this analysis. By taking this into account, $\tilde{\chi}_1^0$ masses within 3.3 GeV of the true value were found. Given the uncertainty in the validity of this correction, the systematic error on the $\tilde{\chi}_1^0$ mass is estimated to be 5 GeV.

It is estimated that in the actual experiment, the uncertainty in the absolute jet energy scale will be of the order of 1% for jets with $p_T > 50$ GeV [84]. For lower energy jets an uncertainty of 2-3% is more likely. With real data, therefore, it may be possible to reduce the systematic uncertainty on the $\tilde{\chi}_1^0$ mass to 2% (2.4 GeV).

Slepton and $\tilde{\chi}_2^0$ mass measurement systematics

Before finding slepton and $\tilde{\chi}_2^0$ masses in section 5.6.6, a correction was applied to the 4-momenta of the jets from the $\tilde{\chi}_1^0$ decay. After this correction, the mass of all reconstructed $\tilde{\chi}_1^0$s is equal to the true mass and the width and bias of the mass peak are removed. A similar procedure would be followed in the actual experiment but the true mass would be unknown. Instead, the $\tilde{\chi}_1^0$ jets will be calibrated so that all $\tilde{\chi}_1^0$ masses are equal to the best estimate of the true mass. In the previous section, a systematic error of 5 GeV on the $\tilde{\chi}_1^0$ mass measurement was found. This error introduces a systematic error into the measurement of the slepton and $\tilde{\chi}_2^0$ masses.

Figure 5.24 shows an approximately linear variation of the errors on the slepton and $\tilde{\chi}_2^0$ masses with the error in the $\tilde{\chi}_1^0$ mass. The uncertainty in the jet energy scale will therefore contribute a systematic error of approximately 5 GeV to the slepton and $\tilde{\chi}_2^0$ masses.

A second contribution to the $\tilde{\chi}_2^0$ and slepton mass systematic is the uncertainty in the absolute lepton momentum scale. At the TeVatron this scale is known to approximately 0.1%. Work in [84] shows that an error of 0.02% in the electron momentum scale is possible. The systematic error on the muon momentum scale, however, will probably be closer to 0.1%. For the purposes of this analysis, a systematic error of 0.1% is used for both leptons. The average transverse momentum of the leptons is approximately 70 GeV (figure 5.12) and the systematic error on the momentum is therefore of order 0.1 GeV. It is assumed that the error on the angular measurement of leptons is small compared to the momentum systematic.

5.7 Conclusions

The majority of ATLAS SUSY studies have concentrated on R-parity conserving models. There are, however, no theoretical or empirical reasons to impose R-parity conservation. This chapter presents a study of mSUGRA point 5 with a non-zero RPV coupling,

$\lambda''_{212} = 0.005$. The study is the first to use a new version of the HERWIG event generator which correctly incorporates RPV vertices. The ATLAS detector is simulated using ATLFAST, a well tested particle level simulation.

The small RPV coupling of this study allows the LSP ($\tilde{\chi}_1^0$) to decay via a baryon number violating vertex into a charm, a down and a strange quark. It has been demonstrated that a $\tilde{\chi}_1^0$ mass peak can be found after three years of low luminosity running using cuts on jet kinematics and multiplicity and a statistical background subtraction. No flavour tagging of jets is used and the algorithm is therefore equally applicable to other RPV λ'' couplings. In fact, the algorithm could, in principle, be modified to find the $\tilde{\chi}_1^0$ mass in a variety of mSUGRA scenarios.

If the decay chain $\tilde{\chi}_2^0 \to \tilde{l}_R^{\pm} l^{\mp} \to l^{\pm} l^{\mp} \tilde{\chi}_1^0$ is open, as at point 5, a significantly improved $\tilde{\chi}_1^0$ mass peak with minimal background can be obtained. It was also shown that the masses of the light right-sleptons and the $\tilde{\chi}_2^0$ can be measured. The errors on these measurements were found to be dominated by the systematic uncertainty in the jet energy scale. Table 5.13 summarises the masses found and the associated errors.

Sparticle	True mass (GeV)	Measured mass (GeV)
$\tilde{\chi}_1^0$	121.5	124.8 ± 0.6(stat)± 5.0(had)
Right-smuon/selectron	157.2	157.6 ± 0.02(stat)± 5.0(had)± 0.1(EM)
$\tilde{\chi}_2^0$	233.0	235.6 ± 0.2(stat)± 5.0(had)± 0.1(EM)

Table 5.13: A summary of the masses found in this analysis and the statistical and systematic errors on each measurement. The systematic errors from hadronic (had) and electromagnetic (EM) calorimetry are shown separately.

Chapter 6

Conclusions

At the 1 TeV energy scale of the LHC, it is predicted that physics beyond the Standard Model will be observed. The ATLAS detector will surround one of the LHC interaction points and is designed to discover and investigate a wide range of possible new physics. ATLAS was described in chapter 1 of this thesis.

The ATLAS Inner Detector will provide high precision tracking of charged particles. Silicon microstrip detectors will be used in the SCT where they must operate in a high radiation environment and in a magnetic field. Chapter 2 introduced the theory behind silicon detectors. Radiation damage to detectors and the implications of operation in a magnetic field were also discussed. The last part of chapter 2 described two designs of silicon microstrip detectors, referred to as p-in-n and n-in-n. Both designs were, in 1997, being considered for use in the SCT. The operational requirements of SCT detectors were also presented.

The aim of the 1997 test beam, described in chapter 3, was to compare the expected performance of n-in-n and p-in-n detectors after the minimum lifetime of ATLAS. Three detectors of each design were irradiated and thermally annealed to emulate 10 years of SCT operation. Modules containing the irradiated detectors were then investigated using a normally incident 180 GeV/c pion beam. The n-in-n modules were found to operate at maximum efficiency when biased at approximately half the CV determined full depletion voltage. The p-in-n modules demonstrated maximally efficient operation at or above the full depletion voltage. This difference in behaviour is due to irradiated n-in-n and p-in-n detectors depleting from strip and non-strip sides respectively. For the same reason, the precision of the p-in-n modules was observed to be degraded below full depletion. The module precision and efficiency of a given module were found to be similar for the read-out of 6 cm and 12 cm long strips.

All n-in-n and two p-in-n modules operated at maximum efficiency when biased at the highest voltage allowed by the SCT detector specifications. The maximum observed efficiency of all modules was below the specification value of 99%. It was, however, demonstrated that the inefficiency was not intrinsic to the detectors but introduced during detector read-out. The FEE and DAQ used in this test beam will not be used in the ATLAS detector. The noise occupancy of both module types was also slightly worse than permitted by the SCT specifications but is also dependent on the choice of read-out electronics.

The charge collected on a detector strip was compared to the predictions of Landau theory. Large differences between the experimental and theoretical distributions were observed. The differences were attributed predominantly to the loss of ionisation electrons from the thin detectors but also to charge sharing between strips, charge trapping and pulse shaping.

In summary, it was demonstrated in the 1997 test beam that p-in-n and n-in-n detectors which satisfy the SCT specifications can be fabricated. The ATLAS Collaboration therefore decided to use cheaper p-in-n detectors in the SCT.

The 1998 test beam, described in chapter 4, studied the performance of p-in-n detectors in a magnetic field and with non-normally incident particles. Two modules were investigated: the first employed an unirradiated detector, the second an identical but irradiated detector. Both modules performed to specification in a 1.56 T magnetic field and for the range of particle angles of incidence that will be observed in the SCT. In contrast to the 1997 test beam, both modules demonstrated a maximum efficiency better than 99%. Charge sharing between detector strips was shown to be well described by a model of charge diffusion in silicon detectors.

A large number of studies have demonstrated the potential of ATLAS to discover and measure the parameters of various SUSY models. Most studies, however, have concentrated on R-parity conserving scenarios. Chapter 5 described a study of the LHC mSUGRA point 5 with a non-zero RPV coupling, $\lambda''_{212} = 0.005$. In this scenario, the LSP ($\tilde{\chi}_1^0$) decays into a charm, a down and a strange quark. The $\tilde{\chi}_1^0$ mass can therefore be measured if the jets from a $\tilde{\chi}_1^0$ decay can be identified. A new version of HERWIG which correctly incorporates RPV vertices was used to generate events. The ATLAS detector response was modelled using ATLFAST, a particle level simulation.

A $\tilde{\chi}_1^0$ mass peak was obtained using cuts on jet kinematics, jet multiplicity and a statistical background subtraction. At mSUGRA point 5, the decay chain $\tilde{\chi}_2^0 \rightarrow \tilde{l}_R^{\pm} l^{\mp} \rightarrow l^{\pm} l^{\mp} \tilde{\chi}_1^0$ is open. It was shown that the right-slepton and $\tilde{\chi}_2^0$ masses could be measured by combining the leptons from the $\tilde{\chi}_2^0$ decay chain with the reconstructed $\tilde{\chi}_1^0$s. In addition, significantly improved $\tilde{\chi}_1^0$ and right-slepton mass peaks with minimal background were obtained by selecting events in the observed $\tilde{\chi}_2^0$ mass peak. The errors on the mass measurements were found to be dominated by the systematic uncertainty of approximately 4% in the jet energy scale correction. SM backgrounds were shown to be small. No flavour tagging of jets was used in the analysis of chapter 5. The algorithm developed is therefore equally applicable to scenarios with different non-zero λ'' couplings.

Bibliography

[1] ATLAS Collaboration. Technical Proposal for a General-Purpose *pp* Experiment at the Large Hadron Collider at CERN. Technical Proposal CERN/LHCC 94-43, CERN, 1994.

[2] The LHC: Conceptual Design Report, 1995. CERN/AC/95-05(LHC).

[3] S. Weinberg. A model of leptons. *Phys. Rev. Lett.*, 19:1264, 1967.

[4] A. Salam. Weak and electromagnetic interations. In Svartholn, Almquist & Wiksells, editor, *Elementary Particle Theory, Proceedings Of The Nobel Symposium, Lerum, Sweden*, pages 367–377, 1968.

[5] S. Glashow et al. Weak interactions with lepton-hadron symmetry. *Phys. Rev. D*, 2:1285, 1970.

[6] J Valle. Physics beyond the SM. *hep-ph/960330*, 1996.

[7] S Martin. A Supersymmetry Primer. In G.L. Kane, editor, *Perspectives on Supersymmetry*. World Scientific, 1999. Extended version available as hep-ph/9709356.

[8] P. Higgs. Broken symmetries and the masses of gauge bosons. *Phys. Rev. Lett.*, 13:508, 1964.

[9] P. Higgs. Spontaneous symmetry breakdown without massless bosons. *Phys. Rev.*, 145:1156, 1966.

[10] The LEP Collaborations ALEPH, DELPHI, L3, OPAL. Report of the LEP Electro-weak Working Group and the Heavy Flavour and Electro-weak Groups. EP 99-15, CERN, 1999.

[11] M Felcini. Searches for Higgs particles at LEP. Talk given at XXXIVth Rencontres de Moriond, Les Arcs, France, March 13-20, 1999.

[12] ALEPH, DELPHI, L3 and OPAL Collaborations. Limits on Higgs boson masses from combining the data of four LEP experiments at $\sqrt{s} \leq 183$ GeV. EP 99-060, CERN, 1999.

[13] The NA48 Collaboration. Proposal for a precision measurement of ϵ'/ϵ in CP violating $K^o \rightarrow 2\pi$ decays. Technical proposal SPSC/90-22, CERN, 1990.

[14] The KTeV Collaboration. Proposal to continue the study of direct CP violation and rare decay processes in KTeV in 1999. Technical proposal, Fermilab, 1997.

[15] R McPherson. Searching for standard SUSY. Talk given at XXXIVth Rencontres de Moriond, Les Arcs, France, March 13-20, 1999.

[16] D0 Collaboration. Search for squarks and gluions in events containing jets and a large inbalance in transverse energy. *hep-ex/990201*, 1999.

[17] D0 Collaboration. Search for squarks and gluinos is single-photon events with jets and large missing transverse energy in $p\bar{p}$ collisions at $\sqrt{s} = 1.8$ TeV. *Phys. Rev. Lett.*, 82:29–34, 1999.

[18] CDF Collaboration. Search for gluino and squark cascade decays at the Fermilab Tevatron Collider. *Phys. Rev. Lett.*, 76:2006, 1996.

[19] Z Kunszt. Higgs production at the LHC: an update on cross sections and branching ratios. *Z. Phys. C*, 74:479–491, 1997.

[20] ATLAS Collaboration. ATLAS Detector and Physics Peformance TDR, Volume II. Technical Report CERN/LHCC 99-15, CERN, 1999.

[21] I Hinchcliffe et al. Precision SUSY Measurements with ATLAS: Introduction and Inclusive Measurements. ATLAS Internal Note PHYS-97-107, CERN, 1997.

[22] E Richter-Was et al. Precision SUSY measurements with ATLAS for SUGRA points 1 and 2. ATLAS Internal Note PHYS-97-108, CERN, 1997.

[23] I Hinchcliffe et al. Precision SUSY Measurements at LHC point 3. ATLAS Internal Note PHYS-97-109, CERN, 1997.

[24] F Gianotti. Precision SUSY measurements with ATLAS: SUGRA point 4. ATLAS Internal Note PHYS-97-110, CERN, 1997.

[25] G Polesello et al. Precision SUSY measurements with ATLAS for SUGRA point 5. ATLAS Internal Note PHYS-97-111, CERN, 1997.

[26] CMS Collaboration. CMS Technical Proposal. Technical Proposal CERN/LHCC 94-38, CERN, 1994.

[27] LHC-B Collaboration. A Large Hadron Collider Beauty Experiment for Precision Measurements of CP Violation and Rare Decays. Technical Proposal CERN/LHCC 98-4, CERN, 1998.

[28] ALICE Collaboration. A Large Ion Collider Experiment at the CERN LHC. Technical Proposal CERN/LHCC 95-71, CERN, 1995.

[29] ATLAS Collaboration. ATLAS Inner Detector TDR, Volume I. Technical Report CERN/LHCC 97-16, CERN, 1997.

[30] ATLAS Collaboration. ATLAS Inner Detector TDR, Volume II. Technical Report CERN/LHCC 97-17, CERN, 1997.

[31] ATLAS Collaboration. ATLAS Calorimeter Performance TDR. Technical Report CERN/LHCC 96-40, CERN, 1996.

[32] ATLAS Collaboration. Liquid Argon Calorimeter TDR. Technical Report CERN/LHCC 96-41, CERN, 1996.

[33] ATLAS Collaboration. Tile Calorimeter TDR. Technical Report CERN/LHCC 96-42, CERN, 1996.

[34] ATLAS Collaboration. Muon Spectrometer TDR. Technical Report CERN/LHCC 97-22, CERN, 1997.

[35] Landolt-Bornstein. *Numerical Data & Functional Relationships in Science & Technology. New Series, Group III*, volume 17a: Physics of Group IV elements & III-V Compounds. Springer, 1985.

[36] J. Hook & H. Hall. *Solid State Physics*, pages 172–177. Wiley, 2nd edition, 1991.

[37] W R Leo. *Techniques for Nuclear and Particle Physics Experiments.* Springer-Verlag, 1994.

[38] L Landau. On the energy loss of fast particles by ionisation. *J. Phys. USSR*, 8(4):201, 1944.

[39] C. Caso et al. 1998 Review of Particle Physics. *The European Physical Journal C3*, 1, 1998.

[40] J Bak et al. Large departures from Landau distributions for high-energy particles traversing thin Si and Ge targets. EP 87-62, CERN, 1987.

[41] W. Shockley. *Electrons and Holes in Semiconductors: with applications to transistor electronics*, pages 207–211. Von Nostrand, 1st edition, 1950.

[42] E Belau et al. Charge collection in silicon strip detectors. *Nuclear Instruments and Methods*, 214:253–260, 1983.

[43] The ROSE Collaboration. RD48 status report. Status report CERN/LHC 97-39, CERN, 1997.

[44] P. Reidler & D Morgan. Analysis of irradiated and annealed ATLAS prototype silicon detectors. ATLAS Internal Note INDET-98-209, CERN, 1998.

[45] E. Barberis et al. Temperature effects on radiation damage to silicon detectors. *Nuclear Instruments and Methods*, A326:373, 1993.

[46] D. Pitzl et al. Type inversion in silicon detectors. *Nuclear Instruments and Methods*, A311:98–104, 1992.

[47] H.-J. Ziock et al. Temperature dependence of the radiation induced change of depletion voltage in silicon PIN detectors. *Nuclear Instruments and Methods*, A342:96–104, 1994.

[48] E. Fretwurst et al. Reverse annealing of the effective impurity concentration and long term operational scenario for silicon detectors in future collider experiments. *Nuclear Instruments and Methods*, A342:119–125, 1994.

[49] K Wyllie. *The design and development of radiation-tolerant silicon microstrip detectors for tracking at the future Large Hadron Collider.* PhD thesis, University of Cambridge, 1997.

[50] L. Andricek et al. Single sided p^+n detectors for the ATLAS silicon tracker. ATLAS Internal Note INDET-97-191, CERN, 1997.

[51] Eurisys Mésures, 1 Chemin de la Roseraie, Lingolsheim, BP 3111-67834 Tanneries Cedex, France.

[52] SINTEF, P.O. Box 124, Blindern, N-0314 Oslo, Norway.

[53] Max Planck Institut für Physik, Postfach 401212, Foehringer Ring 6, D-80805, Munich, Germany.

[54] Hamamatsu Photonics, 1126-1 Ichino-cho, Hamamatsu 435, Japan.

[55] *Novel p-stop structure for n-strip readout detectors*, 1997. Presented at the 3rd International Symposium on Development and Application of Semiconductor Tracking Detectors, Melbourne, 1997. To be published in Nucl. Instr. and Methods A.

[56] P. Allport et al. A comparison of the performance of irradiated p-in-n and n-in-n silicon microstrip detectors read out with fast binary electronics. To be published in NIM, 1998.

[57] D Morgan et al. Annealing of irradiated silicon strip detectors for the ATLAS experiment at CERN. *Nuclear Instruments and Methods*, A426:366–374, 1999.

[58] L Beattie et al. Dependence of depletion voltage and capacitance on temperature and frequency in heavily irradiated silicon diodes. ROSE technical note 97/4, CERN, 1997.

[59] E Spencer et al. A fast shaping low power amplifier-comparitor integrated circuit for silicon strip detectors. *IEEE Trans. Nucl. Scie.*, 42:796, 1995.

[60] J DeWitt. A pipeline and bus interface chip for silicon strip detector read-out. *Proc. IEEE Nucl. Scie. Symp.*, November 1993.

[61] J DeWitt. Header-Adder Chip. Preprint, Santa Cruz Institute of Particle Physics, 1995.

[62] Manufactured by Integrated Detectors and Electronics AS(IDEAS), Oslo, Norway.

[63] F Albiol et al. Beam test of the ATLAS silicon detector modules with binary readout in the CERN H8 beam in 1996. *Nuclear Instruments and Methods*, 409:236–239, 1998.

[64] RD13 Collaboration. Status report of a scalable data taking system at a testbeam for LHC. CERN/LHCC Note 95-47, CERN, 1995.

[65] J. DeWitt et al. Beam test of binary silicon system in H8 in September 1995. ATLAS Internal Note INDET-96-135, CERN, 1996.

[66] RD2 Collaboartion. Final report on the RD2 project. LHCC 96-5, CERN, 1996.

[67] S Gadomski & P Weilhammer. Fast and low noise front-end electronics for Si detectors at the LHC. *NIM*, A351:201, 1994.

[68] G Hall. Ionisation energy losses of highly relativistic charged particles in thin Si layers. *Nucl. Instr. & Methods*, 220:356–362, 1984.

[69] P Shulek et al. Fluctuations of ionisation loss. *Sov. J. of Nucl. Phys*, 4, 1960.

[70] D Robinson et al. Noise studies of n-strip on n-bulk Silicon Microstrip Detectors using Fast Binary Readout Electronics after Irradiation to 3×10^{14}p cm^{-2}. To be published in Nucl. Instr. and Methods.

[71] Private communication with D. Robinson, Cavendish Laboratory, Cambridge.

[72] ATLAS Technical Coordination Team. ATLAS Technical Coordination TDR, Volume I. Technical Report CERN/LHCC 99-01, CERN, 1999.

[73] MSSM Working group. Report of the MSSM working group for the Workshop "GdR-Supersymétrie". PM/98-45, 1998.

[74] L Alvarez-Gaumé et al. Minimal low-energy supergravity. *Nucl. Phys. B*, 221:495–523, 1983.

[75] H Dreiner. An Introduction to Explicit R-parity Violation. In G.L. Kane, editor, *Perspectives on Supersymmetry*. World Scientific, 1997. hep-ph/9707435.

[76] G Bhattacharyya. A brief review of R-parity violating couplings. *hep-ph/9709395*, 1997.

[77] A Mirea & E Nagy. Study of the determination of the SUGRA parameters using the ATLAS detector in the case of L-violating R parity breaking. Internal ATLAS note PHYS-99-007, CERN, 1999.

[78] E Richter-Was et al. ATLFAST 2.0: A Fast Simulation Package for ATLAS. ATLAS Internal Note PHYS-98-131, CERN, 1998.

[79] G Marchesini et al. HERWIG 5.9. *Computer Phys. Commun.*, 67:465, 1992.

[80] K Odagiri. HERWIG 6.1, with supersymmetric processes. Talk given at The Second Workshop: Tools for SUSY '99, Lyon, March 31st - April 2nd, 1999.

[81] H Dreiner & P Richardson. R-Parity Violating Monte Carlo Simulations with HERWIG. Talk given at The Second Workshop: Tools for SUSY '99, Lyon, March 31st - April 2nd, 1999.

[82] H. Baer et al. Simulating Supersymmetry with Isajet 7.0/Isasusy 1.0. *hep-ph/930329*, 1993.

[83] B Allanach et al. Stringy SUSY searches at the LHC. To be published.

[84] ATLAS Collaboration. ATLAS Detector and Physics Peformance TDR, Volume I. Technical Report CERN/LHCC 99-14, CERN, 1999.

[85] E. Buis et al. Parameterisation of the Inner Detector Performance. ATLAS Internal Note INDET-98-197, CERN, 1998.

[86] D Cavalli & S Resconi. Comparison between full simulation and fast simulation of the ATLAS detector. ATLAS Internal Note PHYS-97-100, CERN, 1997.

[87] H Baer et al. Impact of hadronic decays of the lightest neutralino on the reach of the CERN LHC. *Phys rev D*, 55:1466–1470, 1997.

[88] J Söderqvist. Consequences of Baryonic R-parity Violation for Measurements of SUSY Particles using the ATLAS Detector. ATLAS Internal Note PHYS-98-122, CERN, 1998.

[89] M Bosman et al. Jet Finder Library: Version 1.0. ATLAS Internal Note SOFT-98-038, CERN, 1998.

[90] H Baer et al. Cosmic relic density from minimal supergravity with implications for collider physics. *Phys. Rev D.*, 53:597–605, 1996.

[91] Higgs Working Group. Physics at LEP2: Higgs Physics. Yellow Report 96-01, CERN, 1996.

[92] E Richter-Was & D Froidevaux. MSSM Higgs searches in multi-b-jet final states. ATLAS Internal Note PHYS-97-104, CERN, 1997.

[93] P Savard. The $W \rightarrow$jet-jet and top mass reconstruction with the ATLAS Detector. ATLAS Internal Note CAL-97-092, CERN, 1997.

Appendix A

Derivation of the dilepton invariant mass upper edge

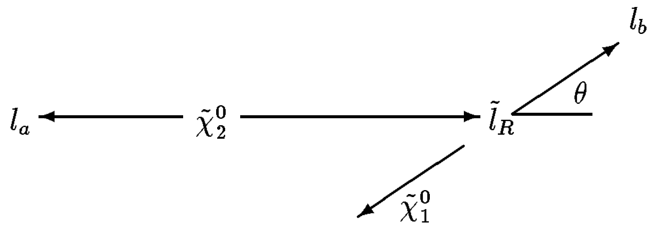

Figure A.1: The decay of the $\tilde{\chi}_2^0$

The invariant mass of the two OSSF leptons (l_a, l_b) from the decay $\tilde{\chi}_2^0 \to \tilde{l}_R^{\pm} l_a^{\mp} \to \tilde{\chi}_1^0 l_a^{\mp} l_b^{\pm}$ (figure A.1) has a sharp upper edge. The position of this edge is given by equation A.1 which is derived in this appendix.

$$m_{ll}^{(\max)} = m_{\tilde{\chi}_2^0} \sqrt{1 - \frac{m_{\tilde{l}_R}^2}{m_{\tilde{\chi}_2^0}^2}} \sqrt{1 - \frac{m_{\tilde{\chi}_1^0}^2}{m_{\tilde{l}_R}^2}} \tag{A.1}$$

The decay comprises two two-body decays. Working in the rest frame of the $\tilde{\chi}_2^0$, the four-momenta of the products of the first decay, $\tilde{\chi}_2^0 \rightarrow \tilde{l}_R^{\pm} l_a^{\mp}$, can be written as:

$$p_a = \begin{pmatrix} a \\ -a \\ 0 \\ 0 \end{pmatrix} \qquad p_{\tilde{l}_R} = \begin{pmatrix} m_{\tilde{\chi}_2^0} - a \\ a \\ 0 \\ 0 \end{pmatrix} \tag{A.2}$$

where p_a is the 4-momentum of the lepton. It is assumed that the mass of the lepton, m_a, is small compared to the SUSY particle masses and momenta ($\sim$1 GeV). Using $m_{\tilde{l}_R}^2 = E_{\tilde{l}_R}^2 - \vec{p}_{\tilde{l}_R}^{\,2}$ one finds that:

$$a = \frac{m_{\tilde{\chi}_2^0}^2 - m_{\tilde{l}_R}^2}{2m_{\tilde{\chi}_2^0}} \tag{A.3}$$

The slepton then decays into a $\tilde{\chi}_1^0$ and a lepton. Conservation of energy and momentum gives the the four-momenta of the $\tilde{\chi}_1^0$ and second lepton (l_b):

$$p_{\tilde{\chi}_1^0} = \begin{pmatrix} m_{\tilde{\chi}_2^0} - a - b \\ a - b\cos\theta \\ -b\sin\theta \\ 0 \end{pmatrix} \qquad p_b = \begin{pmatrix} b \\ b\cos\theta \\ b\sin\theta \\ 0 \end{pmatrix} \tag{A.4}$$

where θ is the angle between l_b and the slepton as shown in figure A.1. Using $m_{\tilde{\chi}_1^0}^2 = E_{\tilde{\chi}_1^0}^2 - \vec{p}_{\tilde{\chi}_1^0}^{\,2}$ and equation A.3 gives:

$$b = \frac{m_{\tilde{\chi}_2^0}(m^2_{\tilde{\chi}_1^0} - m^2_{\tilde{l}_R})}{(m^2_{\tilde{\chi}_2^0} - m^2_{\tilde{l}_R})(1 + \cos\theta) - 2m^2_{\tilde{\chi}_2^0}} \tag{A.5}$$

The invariant mass of the two leptons, m_{ll}, is given by:

$$m_{ll}^2 = (E_a + E_b)^2 - (\vec{p}_a + \vec{p}_b)^2 \tag{A.6}$$

$$= 2ab - 2\vec{a}.\vec{b} = 2ab(1 + \cos\theta) \tag{A.7}$$

Substituting for a and b gives

$$m_{ll}^2 = \frac{(m^2_{\tilde{l}_R} - m^2_{\tilde{\chi}_1^0})(m^2_{\tilde{\chi}_2^0} - m^2_{\tilde{l}_R})(1 + \cos\theta)}{(m^2_{\tilde{l}_R} - m^2_{\tilde{\chi}_2^0})(1 + \cos\theta) + 2m^2_{\tilde{\chi}_2^0}} \tag{A.8}$$

This is maximal at $\theta = 0$ and so

$$(m_{ll}^{(\max)})^2 = m^2_{\tilde{\chi}_2^0}(1 - \frac{m_{\tilde{l}_R}}{m_{\tilde{\chi}_2^0}})(1 - \frac{m_{\tilde{\chi}_1^0}}{m_{\tilde{l}_R}}) \tag{A.9}$$